

SLAC-581  
UC-404  
(SSRL-M)

**ELECTRONIC STRUCTURE OF THE BISMUTH FAMILY  
OF HIGH TEMPERATURE SUPERCONDUCTORS\***

Donglai Feng

*Stanford Synchrotron Radiation Laboratory  
Stanford Linear Accelerator Center  
Stanford University, Stanford, California 94309*

SLAC-Report-581  
August 2001

Prepared for the Department of Energy  
under contract number DE-AC03-76SF00515

Printed in the United States of America. Available from the National Technical  
Information Service, U.S. Department of Commerce,  
5285 Port Royal Road, Springfield, VA 22161

---

\* Ph.D. thesis, Stanford University, Stanford, CA 94309.

# ELECTRONIC STRUCTURE OF THE BISMUTH FAMILY OF HIGH TEMPERATURE SUPERCONDUCTORS

a dissertation  
submitted to the department of physics  
and the committee on graduate studies  
of stanford university  
in partial fulfillment of the requirements  
for the degree of  
doctor of philosophy

Donglai Feng  
August 2001

I certify that I have read this dissertation and that in my opinion it is fully adequate, in scope and quality, as a dissertation for the degree of Doctor of Philosophy.

---

Zhi-Xun Shen (Physics and Applied Physics)  
(Principal Adviser)

I certify that I have read this dissertation and that in my opinion it is fully adequate, in scope and quality, as a dissertation for the degree of Doctor of Philosophy.

---

Theodore H. Geballe (Applied Physics)

I certify that I have read this dissertation and that in my opinion it is fully adequate, in scope and quality, as a dissertation for the degree of Doctor of Philosophy.

---

Shou-Cheng Zhang (Physics)

Approved for the University Committee on Graduate Studies:

*To Qing-xuan and my parents Hai-An and Yin-Ming.*

# Abstract

High temperature superconductivity remains the central intellectual problem in condensed matter physics fifteen years after its discovery. Angle resolved photoemission spectroscopy (ARPES) directly probes the electronic structure, and has played an important role in the field of high temperature superconductors.

With the recent advances in sample growth and the photoemission technique, we are able to study the electronic structure in great detail, and address regimes that were previously inaccessible. This thesis work contains systematic photoemission studies of the electronic structure of the Bi-family of high temperature superconductors, which include the single-layer system (Bi2201), the bi-layer system (Bi2212), and the tri-layer system (Bi2223).

We show that, unlike conventional BCS superconductors, phase coherence information emerges in the single particle excitation spectrum of high temperature superconductors as the superconducting peak in Bi2212. The universality and various properties of this superconducting peak are studied in various systems. We argue that the origin of the superconducting peak may provide the key to understanding the mechanism of High-Tc superconductors.

In addition, we identified a new experimental energy scale in the bilayer material, the anisotropic intra-bilayer coupling energy. For a long time, it was predicted that this energy scale would cause bilayer band splitting. We observe this phenomenon, for the first time, in heavily overdoped Bi2212. This new observation requires the revision of the previous picture of the electronic excitation in the Brillouin zone boundary.

As the first ARPES study of a trilayer system, various detailed electronic properties of Bi2223 are examined. We show that, comparing with Bi2212, both superconducting gap and relative superconducting peak intensity become larger in Bi2223, however, the strength of the interlayer coupling within each unit cell is possibly weaker. These results suggest that the large superconducting phase transition temperature in a high temperature superconductor is associated with parameters that cause both large pairing strength and strong phase coherence in the system. The number of  $\text{CuO}_2$  layers in each unit cell is just one of the factors that affect these parameters.

# Acknowledgements

First, I would like to thank Professor Zhi-Xun Shen for the last fruitful five years that I spent under his guidance. Besides his advice and constant support during my Ph.D research, his enthusiasm, encouragements, care and friendship have always accompanied me; his energy, diligence, strictness, intuitions, leadership, and perspective have made him a great role model for me.

I want to thank Prof. Theodore Geballe and Prof. Shou-Cheng Zhang for taking time in their busy schedule to read this thesis and give me helpful comments.

My experimental training comes from three semi or full members of the “Shen-group”. They are Dr. Changyoung Kim, our “junior boss”, whose creativity earned him the nickname “crazy old Changyoung”, Dr. Donghui Lu who is the master of experiment, and seeks perfection in every aspect of beamline 5-4, and Dr. Hiroshi Eisaki, whose visit at Stanford gave me a chance to work with an original and knowledgeable scientist. I want to thank you for being patient mentors, for always being available to discuss and help, and for your encouragement and friendship.

My experiments cannot be done without the beautiful samples from my collaborators. I want to thank Prof. Shimoyama, Prof. Kishio, Prof. Uchida in Tokyo University, Prof. Yoshizaki at Tsukuba University, Dr. Genda Gu in the University of New South Wales, Prof. Eckstein and his students at University of Illinois at Urbana Champaign, Prof. Zhao and Prof. Wen at Institute of Physics, Academia Sinica, Simon, Dr. Kaneko, Dr. Hiroshi and Prof. Greven here at Stanford. Dr. Si and Prof. Xi at Pennsylvania State University.

I am grateful to many colleagues and professors for countless inspiring discussions. Prof. Dirk Van der Marel, Prof. Shou-cheng Zhang, Prof. Shuheng Pan, Prof.

Laughlin, Dr. Pengcheng Dai, Prof. Maekawa, Jiangping Hu, Prof. Kivelson, Dr. Zengbing Chen.

I thank all my friends here at Stanford, my old friends, and my classmates for filling my life with happiness. I want to thank all the other members of our “Shen-group” for creating a big warm family, in which we shared our good times and bad times together, where we happily learned and worked together. More specifically, I want to thank Dr. Andrea Damascelli for bringing in fresh Italian humor to the group and his willingness to take the night shift for you; Dr. Xinjiang Zhou for always saying “no problem” for every favor I asked for; Dr. Scot Kellar, for all the help in my experiments in ALS and organizing the memorable group retreat in Manmooth Lakes; Zahid Hasan for great discussions, for taking great care of me when we were doing experiments in BNL, and for your great book collection; Peter Armitage for your good jokes, and vivid physics, and many reminders of the “doughnut time”; Filip Ronning, for all the hard work we have done with Beamline 5-3, and being strict in reviewing my papers, and your impressive integrity as a great human being; Pavel Bogdanov, for helps in my Berkeley experiments, and many discussions; Alessandra Lanzora for various discussions, and particularly Zhengyu Wang, for your kindness and care, and all the good time and fun that we had together; Kyle Shen, for your help during various experiments and correcting my paper’s English; Wendy Weisman for proof reading of this thesis. I am also indebted to many former members of the Shen-group. Paul White, and Jeff Harris were my mentors in my early days in the group. Chungwuh Nam, Chul Park, Tony Loeser, Dan Marshall have kindly given me their data. Dr. Ann Matsula, Dr Yunping Wang, Dr. Er-Dong Lu, Dr. Wanli Yang has also helped me in various ways. Special thanks go to our group secretary Marilyn Gordon, and department secretary Marcia Keating and Kathleen Guan. Your work made my life at Stanford much easier. All of you have made my stay in Stanford an invaluable experience in my life.

I thank my family for their constant support. My parents, parents-in-law, my sisters and their family, and my brother-in-law have given me so much help, love, encouragements and good wishes. Especially, I want to thank my father for inspiring me to love science back in my childhood, and my mother for all the sacrifice and



suffering of separation from her son.

I thank my wife Qingxuan, to whom I dedicate this thesis and my life, knowing you is the best thing that have ever happened to me. At last, I want to thank our daughter in advance, who is on her way to this world, for your joyful baby-kicks and indicating a fresh and fruitful future.

Stanford, California

Donglai Feng

June 1, 2001

# Contents

<b>Abstract</b>	<b>v</b>
<b>Acknowledgements</b>	<b>vii</b>
<b>1 Introduction</b>	<b>1</b>
1.1 Strongly correlated systems . . . . .	1
1.1.1 Approaches of the many-body problem . . . . .	3
1.1.2 Theoretical models and basic concepts . . . . .	4
1.2 High temperature superconductors . . . . .	7
1.2.1 General picture . . . . .	7
1.2.2 Issues addressed in this thesis work . . . . .	11
1.3 Photoemission Spectroscopy . . . . .	13
1.3.1 Historical remarks . . . . .	13
1.3.2 General principle . . . . .	14
1.3.3 Angle-resolved photoemission spectroscopy . . . . .	17
1.3.4 Modelling . . . . .	19
<b>2 Superconducting peak in cuprates</b>	<b>29</b>
2.1 Introduction . . . . .	30
2.2 Experimental . . . . .	32
2.3 Results . . . . .	33
2.4 Discussion . . . . .	39
2.5 Universality of the superconducting peak in cuprate . . . . .	43
2.6 Summary . . . . .	44

<b>3</b>	<b>Bilayer Band Splitting in Bi2212</b>	<b>46</b>
3.1	Electronic structure of heavily overdoped Bi2212: bilayer splitting . .	46
3.1.1	Introduction . . . . .	46
3.1.2	Experimental . . . . .	48
3.1.3	Results . . . . .	49
3.1.4	Discussion . . . . .	55
3.2	Nature of electronic excitation in Bi2212 near $(\pi, 0)$ : bilayer splitting effects . . . . .	57
3.2.1	Introduction . . . . .	57
3.2.2	Experimental . . . . .	58
3.2.3	Lineshape of $(\pi, 0)$ spectrum: doping and system dependence .	59
3.2.4	Lineshape of $(\pi, 0)$ spectrum: photon energy dependence . . .	62
3.2.5	Quantitative estimation of the bilayer splitting in optimally doped Bi2212 . . . . .	65
3.2.6	Discussion . . . . .	69
3.3	Summary . . . . .	73
<b>4</b>	<b>Electronic Structure of Bi2223</b>	<b>75</b>
4.1	Introduction . . . . .	75
4.2	Experimental . . . . .	77
4.3	Band dispersion, and Fermi surface . . . . .	77
4.4	Pseudogap and superconducting gap . . . . .	78
4.5	Compare the normal state lineshape with Bi2201 and Bi2212 . . . . .	81
4.6	Compare the superconducting state properties for optimally doped cuprates . . . . .	83
4.7	Discussion . . . . .	86
4.8	Summary . . . . .	88
<b>5</b>	<b>Conclusion</b>	<b>89</b>
	<b>Bibliography</b>	<b>91</b>

<b>A</b>	<b>Intriguing data, possible new physics</b>	<b>101</b>
A.1	Electronic structure of heavily overdoped Bi2201 . . . . .	101
A.2	Photon energy dependence of the superconducting peak . . . . .	107
A.3	Dispersion of the superconducting peak . . . . .	109
A.4	Fermi surface, and spectral weight distribution of Bi2212 . . . . .	112
A.5	Fermi surface, and spectral weight distribution of Bi2201 . . . . .	117
A.6	Random interesting figures . . . . .	121
<b>B</b>	<b>Donglai Feng's Publication</b>	<b>125</b>

# List of Tables

2.1	Summary of the Bi2212 samples used in this chapter . . . . .	33
-----	--	----

# List of Figures

1.1	(a) Cartoon picture of one dimension hydrogen chain. (b) Density of state for half filled one band Hubbard model for $U > W$ . . . . .	5
1.2	Crystal structure of Bismuth family of high temperature superconductors. . . . .	8
1.3	Energy bands and correlations in cuprates. . . . .	9
1.4	Phase diagram of Bi2212 high temperature superconductor. . . . .	10
1.5	Energetics of the photoemission process. . . . .	15
1.6	Experimental setup of ARPES . . . . .	18
1.7	Spectral function of a non-interacting electron system and a Fermi liquid	25
2.1	Single particle excitation spectrum for a conventional BCS superconductor . . . . .	30
2.2	Illustration of the peak-dip-hump structure . . . . .	31
2.3	Temperature dependence of the superconducting state spectra of Bi2212	34
2.4	Extraction of the superconducting peak . . . . .	35
2.5	Doping dependence of the superconducting state spectra of Bi2212 at $(\pi, 0)$ . . . . .	36
2.6	Comparison between the superconducting peak ratio and other superconducting state properties . . . . .	38
2.7	Superconducting peak in other systems . . . . .	43
3.1	Illustration of the bilayer band splitting in cuprates . . . . .	48
3.2	Susceptibility of heavily overdoped sample ( $T_c = 65$ K) . . . . .	48
3.3	Band dispersion in heavily overdoped Bi2212 . . . . .	49

3.4	Split Fermi surfaces in heavily overdoped Bi2212 . . . . .	51
3.5	Splitting of the superconducting peak . . . . .	53
3.6	Energy splitting and the anisotropic intra-bilayer coupling strength .	54
3.7	Bilayer splitting becomes less resolvable in ARPES spectrum with de- creased doping . . . . .	59
3.8	Comparison of lineshapes between single- and bi-layer materials . . .	60
3.9	Numerical calculations of the matrix element effects induced by the bilayer splitting . . . . .	62
3.10	Matrix element effects due to the bilayer splitting observed for Bi2212	63
3.11	MDC analysis along the Fermi surface for Bi2201 and Bi2212 . . . . .	67
3.12	Estimation of the bilayer splitting amplitude for optimally doped Bi2212	68
3.13	A cartoon to illustrate the effective bilayer band splitting is suppressed by correlation effects . . . . .	70
3.14	Optical reflectivity data on optimally doped and heavily overdoped Bi2212 . . . . .	72
4.1	Band dispersion and Fermi surface of Bi2223 . . . . .	78
4.2	$d$ -wave superconducting gap and pseudogap in Bi2223 . . . . .	79
4.3	Temperature dependence of the Bi2223 $(\pi, 0)$ spectrum . . . . .	80
4.4	Comparison of the normal state $(\pi, 0)$ spectra of the Bi-family of cuprates	81
4.5	Photon energy dependence of the normal state $(\pi, 0)$ spectra of the Bi-family of cuprates . . . . .	83
4.6	Comparison of the superconducting state spectra of the Bi-family of cuprates . . . . .	84
4.7	Qualitative phase-diagram for the Bi-based HTSCs. . . . .	87
A.1	Fermi surface of heavily overdoped Bi2201 . . . . .	102
A.2	Spectra along high symmetry lines for heavily overdoped Bi2201 . . .	102
A.3	Normal state $(\pi, 0)$ spectrum for heavily overdoped Bi2201 . . . . .	103
A.4	Observation of a kink in the dispersion of heavily overdoped Bi2201 .	104
A.5	Observation of a kink in the dispersion of heavily overdoped Bi2201 (cont'd) . . . . .	105

A.6	Scattering rate of heavily overdoped Bi2201 along the nodal direction	105
A.7	Scattering rate near $E_F$ obtained through the MDC as a function of temperature for heavily overdoped Bi2201. . . . .	106
A.8	Photon energy dependence of the superconducting peak for Pb-Bi2212	107
A.9	Photon energy dependence of the superconducting peak for pure Bi2212	108
A.10	Dispersion of the superconducting peak . . . . .	109
A.11	A new way to look at the superconducting peak dispersion. . . . .	110
A.12	Energy scales in Bi2212 . . . . .	111
A.13	Fermi surface mapping by ARPES . . . . .	112
A.14	Fermi surface of Bi2212 at various doping . . . . .	113
A.15	Fermi surface measured with different photon energies for Bi2212 (SSRL V-3) . . . . .	114
A.16	Summary of Bi2212 Fermi surfaces measured with different photon energies (SSRL V-3) . . . . .	115
A.17	Bi2212 Fermi surfaces measured with different photon energies (ALS and SSRL V-4) . . . . .	116
A.18	Photo energy dependence of the ARPES spectra of Bi2201 . . . . .	118
A.19	Fermi surface measured with different photon energies for Bi2201 . .	119
A.20	Summary of Bi2212 Fermi surfaces measured with different photon energies . . . . .	120
A.21	Superstructure effects in Bi2201 . . . . .	120
A.22	Comparison between the normal state spectra at $(\pi, 0)$ and the nodal Fermi crossing for Bi2201 samples with different dopings . . . . .	121
A.23	Kink in superconducting state spectrum of heavily overdoped Bi2212 at the nodal Fermi crossing . . . . .	122
A.24	A comparison of ARPES spectra along $(0,0) - (\pi, \pi)$ directions for various cuprates. . . . .	122
A.25	A comparison of ARPES spectra along $(0,0) - (\pi, 0)$ directions for various cuprates. . . . .	123
A.26	ARPES spectral lineshape comparison at nodal and antinodal regions for various cuprates . . . . .	124



# Chapter 1

## Introduction

*More is different.*

- Philip W. Anderson

### 1.1 Strongly correlated systems

The high temperature superconductors belong to a large class of materials, that is, strongly correlated materials, which are characterized by strong interactions or correlations between electrons.

The history of strongly correlated materials begins in the early days of modern solid state physics. In 1930's, Bloch[1] and Wilson[2] developed band theory, which explained why some materials exhibit metallic behavior and others insulating behavior. de Boer and Verweij[3] soon pointed out that the Bloch and Wilson picture broke down for a large number of insulating 3d transition metal compounds, such as NiO and CoO, which were predicted to be metals. Peierls pointed out that the large local d-d Coulomb interaction between electrons overran the energy gained by delocalize the electrons[4]. Mott[5] and Hubbard[6] attributed the insulating behavior to electron-electron correlation. Nowadays, these insulators are generally called Mott-Hubbard insulators, and the Hubbard model is frequently used to study strongly correlated systems. In the mean time, Anderson[7] introduced super-exchange in a model with

a large d-d Coulomb interaction of local 3d electrons in competition with the energy lowered via hopping. This model is virtually identical to the Hubbard model.

Local Coulomb interaction  $U$  plays an important role in another class of phenomena, the Kondo[8] and heavy Fermion[9] phenomena, where the magnetic impurities in a metal or even a lattice of these magnetic “impurities” are considered. Anderson[10] introduced the famous “Anderson Hamiltonian” to address these phenomena, where the Coulomb interaction between the local  $d$  electrons or  $f$  electrons in the magnetic impurity plays an important role and determines whether or not a local magnetic moments exist. In the large  $U$  limit, the Anderson Hamiltonian can be transformed to the Kondo Hamiltonian[11], where only spin degree of freedom of the impurities are retained.

The interaction of two electrons, that is, the basic block of these models is rather simple. However, when many of these blocks are put together, i.e., when a two-body or three-body problem becomes a many body problem, correlation effects become dominant and account for a vast number of complex and often surprising phenomena. The biggest intellectual challenge in condensed matter physics is to obtain a better understanding of the many body problem and its manifestation in large variety of phenomena, which include: metal insulator transition, insulator-superconductor transition, Kondo effects, heavy Fermion system, high temperature superconductors, mixed valence systems, quantum Hall effect, colossal magneto-resistance, charge ordering, and so on. Some of these have been interpreted in the framework of these theoretical models in a loose handwaving way. Only in few cases could an exact solutions be achieved, e.g., one dimensional Lieb and Wu[12] solution of the Hubbard model, and the dilute impurity limit Kondo model. Yet both solutions are so complicated that even their physical consequences are a subject of intense research. As stated by Phil Anderson, the ultimate goal of condensed matter physics is to find out “why is more different,” that is, how the accumulation of quantitative changes in terms of the number of interacting particles leads to such rich qualitative phenomena. The meaning of the answer to this question, in my opinion, is beyond the field of condensed matter physics, because similar questions have been asked in the fields of nonlinear dynamics, turbulence, plasma physics, biology, ecology and even sociology

and economics.

Due to these difficulties, the theoretical paradigm is far from being built in the field of strongly correlated system. Unexpected new discoveries are made quite frequently, bringing joy as well as humility to generations of scientists working in this field.

### 1.1.1 Approaches of the many-body problem

Although far from being solved, the strongly correlated system/many body problem can be described and studied at different levels of understanding.

The most microscopic and radical level is the so called “theory of everything,” that is, to solve a Hamiltonian that includes all the Coulomb interactions between all the particles.

$$H = \sum_i \frac{P_i^2}{2m_e} + \sum_{i,j} \frac{e^2}{|r_i - r_j|} + \sum_m \frac{P_m^2}{2M_m} + \sum_{m,n} \frac{Z_m Z_n e^2}{|R_m - R_n|} + \sum_{i,m} \frac{Z_m e^2}{|R_m - r_i|} \quad (1.1)$$

where all the variables follow the common conventions, in which the upper case represents ions and the lower case represents electrons. This “theory of everything” unfortunately is practically unfeasible considering that the size of the system is in the order of  $10^{23}$ .

An alternative approach is to divide the system into small blocks, represent each block with effective parameters, and simplify the interaction between blocks into the effective ones. By extracting the effective major factors and summing over the blocks, one can build up an effective, relatively simpler model, and hopefully, still accounts for the major collective properties of the system. For example, in the Hubbard model for high temperature superconductors, each site is represented by one electron from the lowest binding energy band, the effective hopping or coupling between neighboring sites, and the effective on-site Coulomb repulsion representing the correlation effects, which will be discussed later. This second approach is widely adapted. As a result, many models, such as Hubbard model, t-J model, and t-t'-t''-J model[13], are built and many useful qualitative results are obtained. Although analytic solutions are not available, they provide the basis for a large amount of

discussion. Particularly, these models are simulated by supercomputers. Although limited by the computational power, only systems with about 20 sites (compare with  $10^{23}$ ), can be computed so far, and surprisingly, the qualitative aspects of many numerical results agree well with experiments and have helped guide the direction of new researches. Analytically, various gauge field theories were proposed[18] to deal with these models. Concepts like “slave boson” are introduced to account for the correlation effects. However, they are generally abstract and mathematical.

Another different approach is based on the existing theories for weakly correlated or uncorrelated systems, namely, band picture and Fermi liquid theory. The extension of these theories, such as LDA[14, 15], LDA+U calculations, various perturbation theories, marginal Fermi liquid (MFL)[16], near antiferromagnetic Fermi liquid (NAFL)[17], have been proposed to describe the strongly correlated system. In general, these theories can account for some aspects of the qualitative physics, but they intrinsically belong to a more phenomenological level, and fail to describe many other aspects of the system.

The last level of approach is the experimentalist’s approach, a conceptual and qualitative approach. The major task of a experimentalist is to discover new phenomena and measure its properties. In an area as complicated as strongly correlated systems, no paradigm is available, no theory is generally agreed upon, and new surprises can appear every moment. Thus, the guide of an experimentalist are those concepts and phenomena that have already been studied. Using these guides, an experimentalist builds simple models and conducts speculative gedanken experiments while designing the real ones. During the experiment, he or she is aware that the model is simply an initiative, and searches for traces of interesting physics in every detail of the data.

### 1.1.2 Theoretical models and basic concepts

The simplest model to describe the electron correlation is the *one-band Hubbard model*. Its Hamiltonian is:

$$H = \sum_{i,j,\sigma} t_{ij} c_{i\sigma}^\dagger c_{j\sigma} + U \sum_i n_{i\uparrow} n_{i\downarrow} \quad (1.2)$$

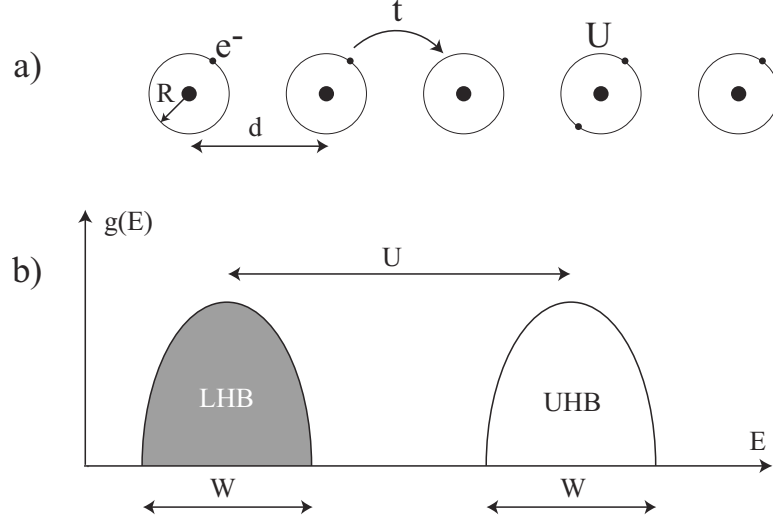


Figure 1.1: (a) Cartoon picture of one dimension hydrogen chain. (b) Density of state for half filled one band Hubbard model for  $U > W$  .

Take the example of one dimensional hydrogen chain Fig. 1.1(a), the first term reflects the kinetic energy, where  $t_{ij} = 0$  unless the  $i$ th and  $j$ th sites are nearest neighbors.  $U$  is the on-site Coulomb repulsion between electrons. This model does not account for long-range Coulomb repulsion, multi-band effects, orbital degeneracy etc., but it does describe how a half-filled band splits into an empty upper Hubbard band (UHB) and a filled lower Hubbard band (LHB). When the band width  $W$  is smaller than  $U$ , the system becomes the so-called *Mott insulator* [Fig. 1.1(b)].

A Mott insulator is a result of the competition between *localization* effects (on-site Coulomb interaction) and *delocalization* effects (hopping to lower the kinetic energy). When the on-site Coulomb interaction dominates, the energy gained by the delocalization of the electron is smaller than what is cost by double occupancy, that is, the bandwidth  $W$  is smaller than  $U$ , the system will be insulating, and vice versa. Localization and delocalization are two very useful concepts in many-body physics. For example, in the case of lanthanide, 4f orbitals are very localized, which correlates with the strong on-site Coulomb interactions in these systems. These account for the heavy Fermion systems and Kondo effects observed in lanthanide systems. For materials containing 3d transition metal elements, the strength of these two effects are

comparable. *Hybridization* between the 3d orbital and the ligand atoms (e.g. O) is just as important. These gives extremely rich phenomena, such as high temperature superconductivity and colossal magneto-resistance in these materials.

From the view of *spatial scales*, when the distance between sites  $\bar{d}$  (determines  $t$ ) is much larger than the orbital radius  $R$  (determines  $U$ ), at sufficiently large  $\bar{d}$ , each site will be an isolated half-filled atom and, therefore, an insulator.

At the infinite  $U$  limit of the  $t$ - $J$  model, one gets another widely used model: the Hubbard model. The large  $U$  forbids the double occupancy and the effects of the on-site Coulomb interaction is renormalized to  $J$  ( $\sim t^2/U$ ), the magnetic exchange coupling between spins at neighboring sites. The  $t$ - $J$  Hamiltonian is

$$H = \sum_{i,j} t_{ij} c_i^\dagger c_j + J \mathbf{S}_i \cdot \mathbf{S}_j \quad (1.3)$$

Similarly, in  $t-t'-t''-J$  model, the hopping to next and next-next nearest neighbors are included.

Another important factor, *dimensionality*, plays an important role in understanding the strongly correlated systems. In the  $t$ - $J$  model, with  $J > 0$ , antiferromagnetic ground state can be achieved in the classic limit. However, in the case of the two-dimensional  $S = 1/2$  system, Anderson argued that the fluctuations could destroy the long range antiferromagnetic order, and a new type of ground state, namely the Resonance Valence Bond (RVB) state will appear [19]. This state has not been observed in experiments, but the basic idea it represents is widely used [20].

We have shown that various energy and length scales are essential in constructing microscopic models and understanding various complicated phenomena of the strongly correlated systems. Similarly, for a specific problem, there are other characteristic scales, such as time scales, temperature scales, momentum scales etc. These scales define the problem at the zeroth order. Experimentally, they determine the right technique for the specific problem. For example, nuclear magnetic resonance (NMR) is a local probe at the atomic length scale, muon spin resonance is sensitive to changes over  $1000\text{\AA}$ . Neutron scattering experiment and ARPES are sensitive to

very fast fluctuations in the system because of the energy scale involved, while optical measurement and transport measurement are much slower probes. Inelastic soft x-ray scattering may not have enough momentum transfer. Neutron scattering may not have good enough momentum resolution. Scanning tunnelling spectroscopy (STS) is spatial resolved, but not momentum resolved, while angle-resolved photoemission spectroscopy (ARPES) is exactly the opposite.

## 1.2 High temperature superconductors

### 1.2.1 General picture

In the last fifteen years, following the discovery of superconductivity in  $\text{La}_{2-x}\text{Ba}_x\text{CuO}_4$  by Bednorz and Müller [21], a large number of related compounds with high superconducting transition temperatures ( $T_c$ 's) have been found. The most common feature of these high-temperature superconductors (HTSC's) is a layered-perovskite crystal structure containing a planar  $\text{CuO}_2$  network. It is now generally believed that the conduction takes place in the  $\text{CuO}_2$  planes which, therefore, are essential to HTSC's. For example, the first three members of the Bismuth family of HTSC (Fig. 1.2), Bi2201, Bi2212, and Bi2223, have one, two, and three  $\text{CuO}_2$  layers respectively. The  $\text{CuO}_2$  planes extend in the  $a - b$  direction, and the electronic couplings in the interplane ( $c$ ) direction are very weak. In the Bismuth family of materials, doping could be achieved by substituting  $\text{Sr}^{2+}$  ions for some impurity ions, such as  $\text{La}^{3+}$ , or by adding interstitial oxygen.

Now let us turn to the electronic structure of an undoped  $\text{CuO}_2$  plane. As shown in Fig. 1.3(a), low energy physics of the  $\text{CuO}_2$  plane mainly involves the hybridization of  $3d_{x^2-y^2}$  orbital of Copper and  $2p$  orbital of Oxygen. Due to the crystal field,  $d$  and  $p$  bands are not degenerate, and they hybridize as illustrated in Fig. 1.3(b). The resulting band structure is metallic, with the antibonding  $\sigma^*$  band being half filled. However, because of the localized nature of  $d$ -orbitals, the undoped system is actually a Mott insulator. The on-site Coulomb interaction splits the antibonding band into an empty upper Hubbard band and a filled lower Hubbard band [Fig. 1.3(c)]. It also

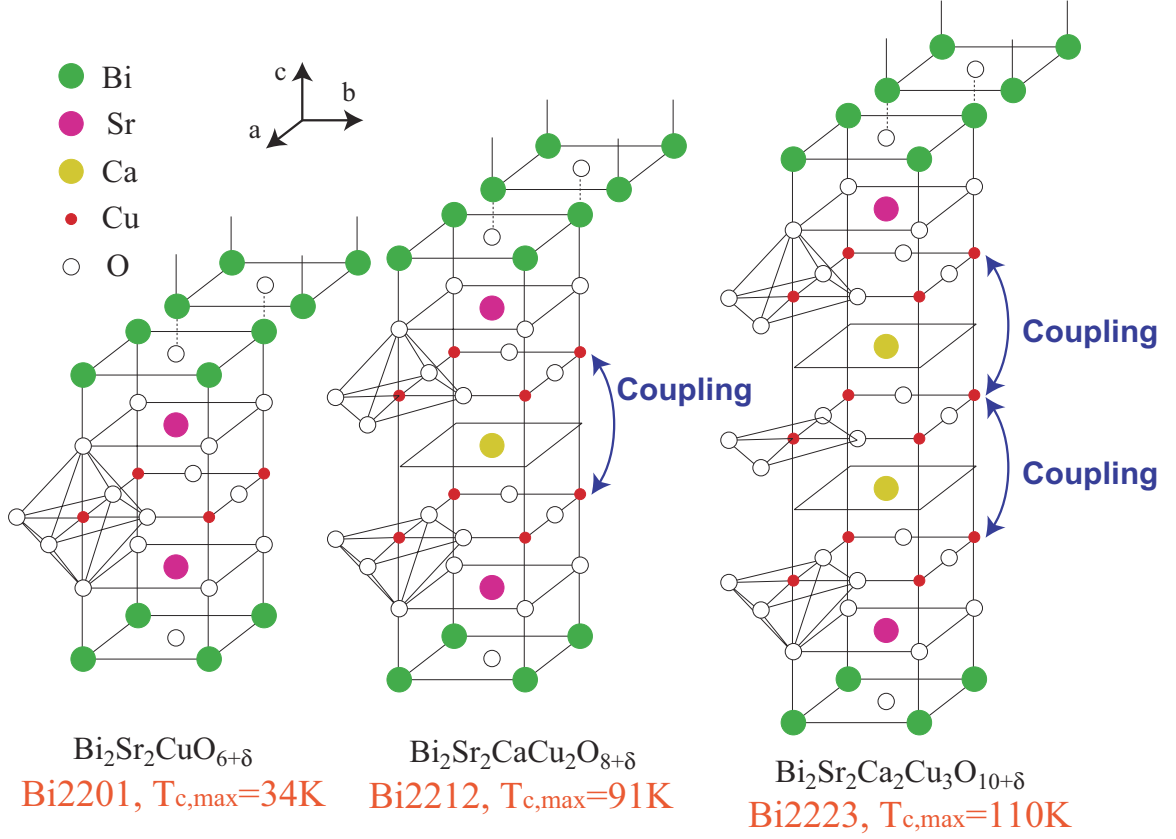


Figure 1.2: Crystal structure of Bismuth family of high temperature superconductors.

has an antiferromagnetic ground state due to the superexchange interaction between the neighboring spins<sup>1</sup>. Because the nonbonding band, which is largely of oxygen nature, located in between the LHB and UHB, the lowest excitation is not of the Hubbard type but the charge transfer type[22]. The excitation is  $\tilde{d}^9 \rightarrow \tilde{d}^8$  for LHB and the charge transfer excitation has additional hopping from the nonbonding band to the LHB to lower the system energy. Thus the overall process is  $\tilde{d}^9 \rightarrow \tilde{d}^9 L^{-1}$ , where  $L^{-1}$  represents a hole in the nonbonding band. These charge transfer insulators are very common in transition metal oxides. If the system is doped with holes, the doped holes are believed to mainly occupy the Oxygen site. In particular, Zhang and Rice[23]

<sup>1</sup>The antiferromagnetic superexchange interaction is originated from the fact that the two neighboring spins on Copper sites could lower the kinetic energy by virtually hopping to the Oxygen sites and/or one of the Copper site together.



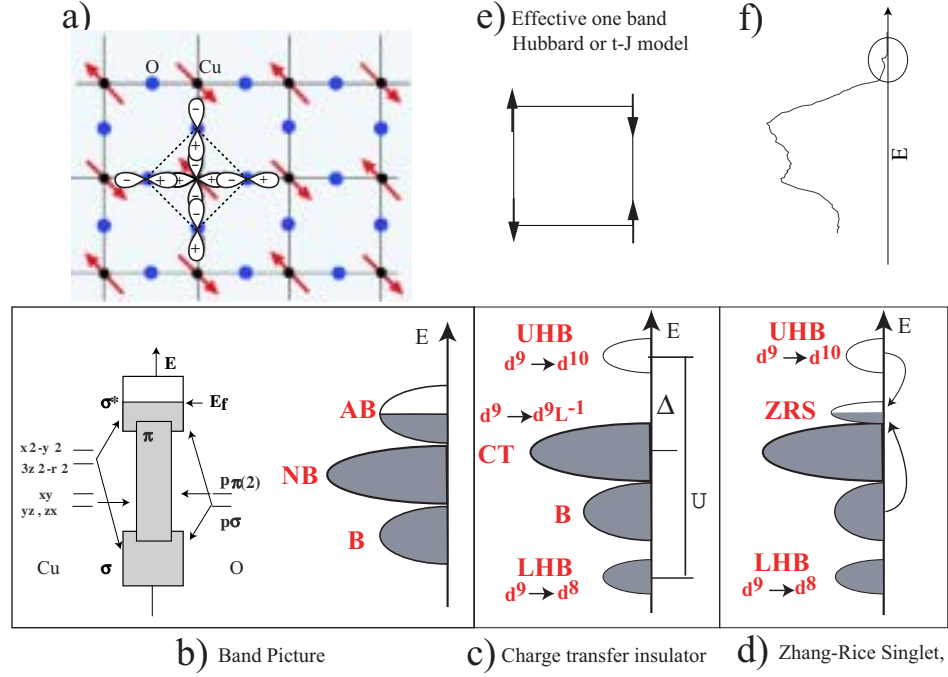


Figure 1.3: (a) Schematic of  $\text{CuO}_2$  plane, the crucial structural subunit for high- $T_c$  superconductivity. Red arrows indicate a possible alignment of spins in the antiferromagnetic ground state. The coupling between oxygen  $p_\sigma$  orbitals and copper  $d_{x^2-y^2}$  leads to superexchange in the insulator and carrier motion in the doped, metallic state. '+' and '-' indicate the phase. (b) band picture of the hybridization of oxygen and copper orbitals. (c) Charge transfer insulator due to the local  $d-d$  Coulomb repulsion. (d) The formation of Zhang-Rice singlet band due to coherence superposition of the four oxygen orbitals surrounding the copper atom as illustrated in (a). The arrows indicate the transfer of spectral weight due to doping. (e) shows the effective one-band model based on the Zhang-Rice singlet band, which is in the circled region of ARPES spectrum in (f).

proposed that Cu-O hybridization strongly binds a hole on each square of O atoms to the central  $\text{Cu}^{2+}$  ion to form a local singlet, which is a coherent superposition of the  $2p_\sigma$  orbitals of the four nearest-neighbour oxygen atoms [Fig. 1.3(a)]. This so-called Zhang-Rice singlet moves through the lattice in a similar way as a hole in the single-band effective Hamiltonian of the strongly interacting Hubbard model. Therefore, it is used as the building block in the construction of effective microscopic Hamiltonians

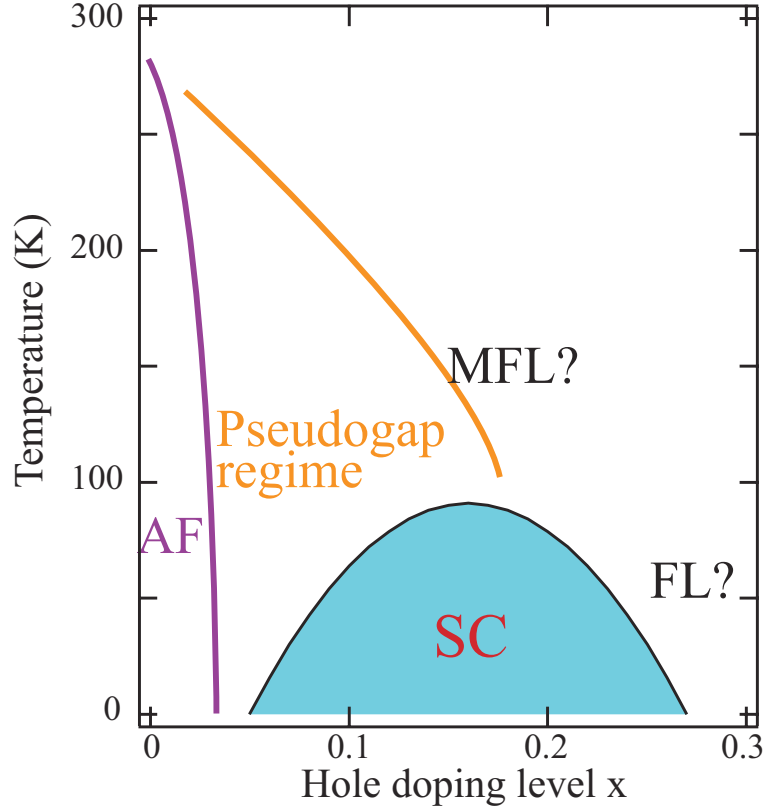


Figure 1.4: Phase diagram of Bi2212 high temperature superconductor.

of the cuprates [Fig. 1.3(e)]. Because, the low energy excitation is mainly the Zhang-Rice-Singlet band [Fig. 1.3(d)], it is also called effective LHB in the literature, which is the circled region of the ARPES spectrum in Fig. 1.3(f), and the main focus of this thesis.

Upon doping, HTSC has very rich phases [Fig. 1.4]. The undoped insulator becomes a superconductor with only 5 ~ 6% holes. The superconducting phase transition temperature  $T_c$  reaches a maximum at the so-called optimal doping level  $x_{opt} \simeq 0.16$ , which separates the superconducting phase into the underdoped regime  $x < x_{opt}$  and the overdoped regime  $x > x_{opt}$  [20].

The optimally doped regime is characterized by linear temperature dependence of the resistivity over a large temperature range. Phenomenologically, this was explained by the Marginal Fermi liquid theory [16], where the scattering rate is a linear function

of temperature and energy. This is recently confirmed by ARPES measurement of the scattering rate[24]. In the superconducting state, a  $d$ -wave superconducting gap opens in HTSC, with the gap node along the  $(0,0) - (\pi, \pi)$  direction, and a gap maximum at  $(\pi, 0)$ [25]. In addition, a pseudogap opens up even in the normal state of underdoped and slightly overdoped samples, which is possibly related to the proximity effect of the antiferromagnetic insulator. The exact origin of the pseudogap has been debated over the years[26]. This type of non-Fermi-liquid behavior is a characteristic of the underdoped regime. On the other hand, the overdoped regime is believed to be more Fermi-liquid-like because of better defined quasi-particles.

In the last five years, experimental advances in material preparation, neutron scattering, STM, ARPES, transport etc. have begun to sketch a converging experimental picture of the HTSC. For example, the stripe instability has been studied by various techniques in YBCO, LSCO systems[27], and has been a very popular and controversial subject in the last several years. The local inhomogeneity has been studied by STM in many systems[28]. The universality of the superconducting peak has been revealed by ARPES and tunnelling measurements[29]. The universality of a kink in the low energy dispersion has been identified in ARPES, and some believe, will have fundamental impact on the study of the mechanism of HTSC. In this context, new theoretical models have also gradually caught up. The recent  $Z(2)$  gauge field theory[30],  $SO(5)$  theory[31], stripe theory[32], etc. have brought fresh ideas into the discussion.

### 1.2.2 Issues addressed in this thesis work

Here we briefly discuss the issues addressed in this thesis. More detailed discussions are embedded in each individual chapters.

As we have discussed in last several sections, due to the lack of proper theory, our approach is to study various concepts and general picture in the HTSC's, rather than to prove or disprove certain theories.

### Superconducting phase transition

For high temperature superconductors, there are many energy scale involved. They are i) the effective on-site Coulomb repulsion  $U \simeq 2 \sim 3\text{eV}$ ; ii) the hybridization or hopping energy scale  $t \sim 0.5\text{eV}$ ; iii) magnetic exchange energy scale  $J \simeq 0.1\text{eV}$ ; iv) the superconducting gap  $\Delta \simeq 4 \sim 40\text{meV}$ ; and v) the superconducting phase transition scale  $T_c \simeq 1 \sim 10\text{meV}$ . It is now understood that the magnetic correlation reduced the band width from  $8t$  to  $4J$ . However, it is still under debate how the  $J$  and  $\Delta$  are related[33]. Unlike the conventional BCS superconductors, the relation between  $\Delta$  and  $T_c$  is also not understood.

These last two energy scales directly associate with the two major ingredients of a superconductor: pairing and phase coherence. The pairing, or the superconducting gap has been extensively studied over the years. However, the phase coherence side of this phenomena is not well studied, particularly if one considers that the high temperature superconductors has very different phase coherence behavior than the conventional superconductors such as the very short coherence length. We pointed out that a particular feature in the ARPES spectrum, the superconducting peak, is directly related to the phase coherence[34] (Chapter 2), and it has very different behavior from the normal state band (Chapter 3). This feature is a very unique and ubiquitous phenomenon of high temperature superconductors (Chapters 2 and 4). We argue that this peak/quasiparticle is created at the superconducting phase transition, and its exact origin may hold the key to solving the problem of the mechanism of HTSC[33].

### Interlayer coupling

One other interesting property of HTSC is the correlation between  $T_c$  and number of  $\text{CuO}_2$  layer ( $n$ ). With increased  $n$ ,  $T_c$  also increases. For example,  $\text{Bi2201}$ ,  $\text{Bi2212}$  and  $\text{Bi2223}$  ( $n = 1, 2$ , and  $3$ , respectively), have maximum  $T_c$ 's of  $34\text{K}$ ,  $90\text{K}$ , and  $110\text{K}$  respectively. Similar relations have also been found for the  $\text{Hg}$  and  $\text{Tl}$  family of HTSC. Therefore, it is important to examine the effect of interlayer coupling on the electronic structure.

For Bi2212 system, intrabilayer splitting causes the bilayer splitting as predicted by various theories, however, its absence has been reported in Bi2212. We have re-examined this issue in detail and show that the bilayer splitting does exist [35](Chapter 3). Moreover, we show that the bilayer splitting energy scale will alter the existing view of electronic excitation in the  $(\pi, 0)$  region dramatically.

### **Trilayer Bi2223 system**

Following the above thinking, we studied the Bi2223 system (Chapter 4), which is the first ARPES study of a trilayer system. Various details of the electronic structure are examined. A systematic view of the interlayer coupling effect is presented.

### **Heavily overdoped systems**

Partly because of the interesting non-Fermi-liquid behavior, most of the previous studies were focused on the underdoped/optimal doped regime. The heavily overdoped regime was not thoroughly studied by ARPES. However, there are many interesting physics that are not addressed in this regime. For example, is this regime really a Fermi liquid? How strong is the correlation effects in this regime? Is there a quantum critical point? etc. We studied the electronic structure of the heavily overdoped Bi2212 (Chapter 3). We found that although the quasiparticle is much better defined in the regime than in the underdoped regime, the correlation effects are still very important.

## **1.3 Photoemission Spectroscopy**

### **1.3.1 Historical remarks**

Photoemission spectroscopy (PES) is used today for a number of experimental techniques that are based on the photoelectric effect. The first observation of the photoelectric effect can be traced back to 1887 when Hertz [36] discovered that a spark between two electrodes occurs more easily with ultraviolet (UV) radiation illuminating the cathode. Subsequent investigations by Thomson [37] and Lenard [38]

identified this effect as the emission of electrons, and established the dependence of the electron current and electron velocity on light intensity and frequency. A satisfying theoretical explanation had not been achieved until Einstein described it as a quantum phenomenon in 1905 [39]. In his quantum theory of the radiation, the photoelectric effect is explained in terms of the simple relationship:

$$E_{kin,max} = h\nu - \phi \quad (1.4)$$

where  $h\nu$  is the photon energy,  $E_{kin}$  is the kinetic energy of the photoelectron, and  $\phi$  is the work function, which denotes the energy necessary to release the electron from the emitter.

The practical aspects of the effect were soon recognized and exploited by means of photocells and, later, photomultipliers [40]. The evolution of PES is intertwined with that of many other experimental techniques, such as the improvement of ultrahigh vacuum (UHV) techniques, the design of electron energy analyzers with high energy and angular resolutions, and the development of synchrotron radiation. Currently, it is a sophisticated technique in the investigation of the electronic properties of atoms, molecules and condensed matter.

### 1.3.2 General principle

The photoemission spectra of a solid are often interpreted in terms of the so called ‘three-step model’ [41, 42, 43, 44]. In this model, the photoemission process is treated as a sequence of:

**step 1:** the optical excitation of an electron,

**step 2:** the transport of the electron through the solid<sup>2</sup>,

**step 3:** the escape from the solid surface into the vacuum.

---

<sup>2</sup>In this step, the electron may be scattered elastically or inelastically. In the latter case, the photoelectron loses energy and excites more electrons, generating what is known as secondary electrons.

For most practical purposes, photoemission spectra are interpreted within the single-particle approximation, and the Einstein equation (1.4) can be extended to describe all electrons, not only those with the highest kinetic energy. Fig. 1.5 illustrates energetics of the photoemission process.

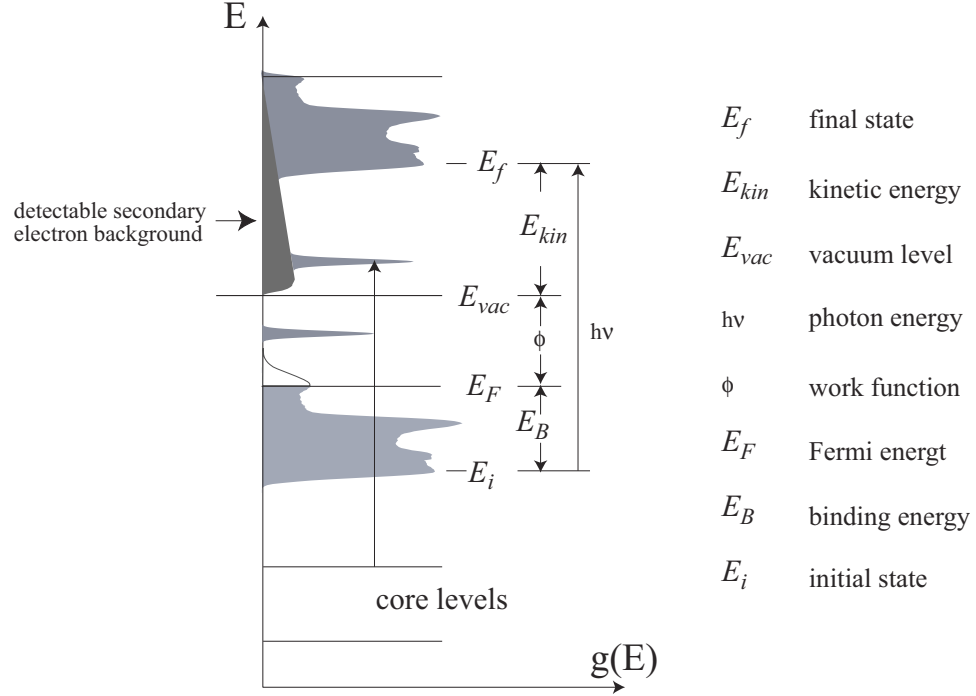


Figure 1.5: Energetics of the photoemission process.

For the optical excitation process (step 1 of the three-step model), the laws of conservation for energy and momentum are given by

$$E_f - E_i - h\nu = 0 \quad (1.5)$$

$$\hbar\mathbf{k}_f - \hbar\mathbf{k}_i - \hbar\mathbf{k}_\gamma = 0 \quad (1.6)$$

where  $E_f$ ,  $E_i$  and  $\mathbf{k}_f$ ,  $\mathbf{k}_i$  are the energy and wave vector of the initial state and final state, respectively.  $\mathbf{k}_\gamma$  denotes the wave vector of the impinging photon. At low photon energies, the momentum of the impinging photon is negligible compared with

the crystal momentum of the electrons in the Brillouin zone (BZ). For example, for the typical photon energy of 20 eV,  $\mathbf{k}_\gamma$  is  $0.01 \text{ \AA}^{-1}$ , which is less than 1% of the typical BZ size of cuprates. Hence, we can use a reduced wave vector  $\mathbf{k}$  for both initial and final states, and the first step of the three-step model can be regarded as a vertical transition from the initial state at  $E_i(\mathbf{k})$  to the final state at  $E_f(\mathbf{k})$ .

For simplicity, we consider only those photoelectrons which propagate towards the sample surface without scattering (step 2 of the three-step model). The escape from the sample surface to the vacuum (step 3 of the three-step model) is then characterized by the work function  $\phi$ . The kinetic energy of the photoelectron detected by the energy analyzer is thereby related to the binding energy inside the solid through the following equation:

$$E_B = h\nu - E_{kin} - \phi \quad (1.7)$$

We note that the wave function of the final state at  $E_f(\mathbf{k})$  is not a single plane wave but a Bloch wave containing components of the form  $\exp[i(\mathbf{k} + \mathbf{G}) \cdot \mathbf{r}]$ , with  $\mathbf{G}$  being any reciprocal wave vector. For each  $\mathbf{k} + \mathbf{G}$  component, there exists the possibility that it can be matched to a travelling wave outside the crystal. Thus, the conservation of the wave vector is given by

$$\mathbf{K}_\parallel = \mathbf{k}_\parallel + \mathbf{G}_\parallel \quad (1.8)$$

where  $\mathbf{K}_\parallel$ ,  $\mathbf{k}_\parallel$  and  $\mathbf{G}_\parallel$  are components parallel to the sample surface of the external photoelectron wave vector  $\mathbf{K}$ , the reduced wave vector  $\mathbf{k}$  and the reciprocal lattice vector  $\mathbf{G}$ , respectively. Unfortunately, the perpendicular component of the wave vector is not conserved, since the crystal is no longer periodic along the perpendicular direction due to the sample surface. As shown in Fig. 1.5, the kinetic energy of the external photoelectron is defined as

$$\begin{aligned} E_{kin} &= \hbar^2(\mathbf{K}_\parallel^2 + K_\perp^2)/2m_e \\ &= E_f(\mathbf{k}) - E_{vac} \end{aligned} \quad (1.9)$$



where  $K_{\perp}$  is the perpendicular component of the photoelectron wave vector and  $E_{vac}$  represents the vacuum level. From Eq. (1.8) and (1.9) we have, for each  $(\mathbf{k}+\mathbf{G})$  component,

$$K_{\perp}^2 = 2m_e[E_f(\mathbf{k}) - E_{vac}]/\hbar^2 - (\mathbf{k}_{\parallel} + \mathbf{G}_{\parallel})^2 \quad (1.10)$$

If  $E_f(\mathbf{k})$  and  $E_{vac}$  are known parameters, both  $\mathbf{K}_{\parallel}$  and  $K_{\perp}$  can easily be calculated out through Eq. (1.8) and (1.10), *i.e.*, energies and directions of the photoelectrons generated by optical transition are completely determined.

### 1.3.3 Angle-resolved photoemission spectroscopy

In angle-resolved photoemission spectroscopy (ARPES), as depicted in Fig.1.6(a), both the kinetic energy and the direction of propagation of the external photoelectrons are directly measurable quantities, *i.e.*, the momentum or wave vector  $\mathbf{K}$  is determined, which is given by

$$\begin{aligned} K_x &= \frac{1}{\hbar} \sqrt{2m_e E_{kin}} \sin \theta \cos \phi \\ K_y &= \frac{1}{\hbar} \sqrt{2m_e E_{kin}} \sin \theta \sin \phi \\ K_z &= \frac{1}{\hbar} \sqrt{2m_e E_{kin}} \cos \theta \end{aligned} \quad (1.11)$$

We would like to trace the external photoelectron back to its initial state inside the crystal and deduce the  $E$  vs.  $\mathbf{k}$  dispersion relations. This ambition, however, encounters some fundamental difficulties. Although  $\mathbf{k}_{\parallel}$  is determined by Eq. (1.8) and (1.11),  $k_{\perp}$  remains indeterminate. Additional assumptions have to be made to determine the value of  $k_{\perp}$ . For example, by assuming a free-electron like behavior of the final state, we have

$$\begin{aligned} E_f(\mathbf{k}) - E_0 &= \hbar^2(\mathbf{k}_{\parallel}^2 + k_{\perp}^2)/2m_e \\ &= E_{kin} + v_0 \end{aligned} \quad (1.12)$$

where  $E_0$  denotes the minimum of the valence band and  $v_0$  is the energy difference

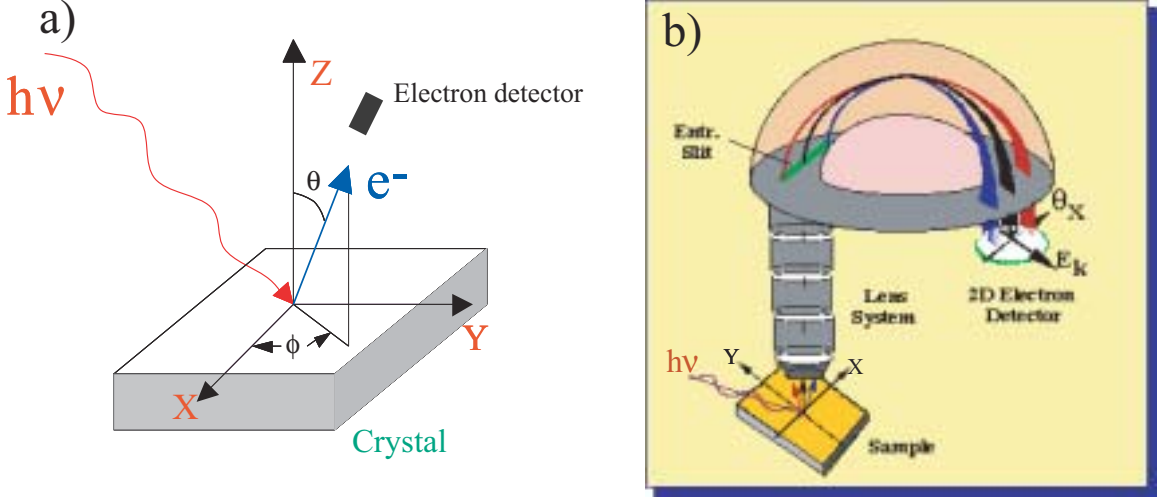


Figure 1.6: (a) The experimental geometry for an angle-resolved photoemission spectroscopy. (b) Modern electron analyzer Scienta SES-200 collects electrons over a large angle and energy simultaneously.

between  $E_0$  and  $E_{vac}$  or the so-called inner potential. From Eq. (1.8), (1.11), and (1.12),  $k_{\perp}$  can be determined. However, such an assumption only holds for the photoelectrons with high kinetic energy ( $\geq 20$  eV).

There are a few special situations in which the band dispersion as a function of  $k_{\perp}$  can be directly determined from experiments. For example, in angle-resolved constant-final-state spectroscopy, the kinetic energy and the direction of the emission are held constant, *i.e.*,  $\mathbf{k}_{\parallel}$  is fixed. By scanning the photon energy, we can sample the band structure as a function of  $k_{\perp}$  along the chosen direction.

For layered compounds like cuprates, the dispersion along the  $k_{\perp}$  direction of the energy bands is usually rather small and can be neglected. In this case, the interpretation of an angle-resolved photoemission experiment is the simplest. The  $E$  vs.  $\mathbf{k}$  relationship and the Fermi surface can be mapped out by following the peak in energy distribution curves (EDC's) at the band energy position.

The recent advance of the electron energy analyzer makes it possible to detect electrons with different emission angles and kinetic energy simultaneously with high resolution [Fig. 1.6(b)]. This not only makes the data taking process much more efficient, but also enable a new way of retrieving information from ARPES, namely, the

momentum distribution curve (MDC) in addition to the previous energy distribution curve (EDC).

### 1.3.4 Modelling

In a rigorous way, the photoemission process is a one-step quantum mechanical event in which an electron, under the effect of the electromagnetic field, is removed from an occupied state and emitted into the detector. Theoretically, it is described by the so-called *one-step model* [45, 46, 47]. In this model, a Green's function method is adopted to take into account the multiple scattering process, correlation effects etc. A formal diagrammatic expansion for photoemission has been put forward by Carolic *et al.* [45], using the Keldysh perturbation theory for nonequilibrium many-body problems. The advantage of the one-step model is that it includes coherence effects and that it can be expanded systematically. However, in practice, due to the complexity in crystal structure, correlation effects, multiple scattering etc., a comprehensive and accurate calculation of the photoemission matrix element based on the one-step model is not feasible. Instead, photoemission data are usually discussed within the *three-step model*, as we have discussed in the last two sections. The advantage of the three-step model is its simplicity and effectiveness. This intuitive and phenomenological model has played an important role in the development of photoemission spectroscopy. With reasonable assumptions, qualitative results obtained based on this model are still widely used today to provide guidance for various experiments.

#### Three-Step Model

In three-step model, the intensities in the photoemission spectra can be calculated in a straightforward approach [48, 49]. According to the three-step model, the EDC of photoemitted electrons  $I(E_f, h)$  is a sum of a primary distribution of electrons  $I_p(E_f, h)$  that have not suffered an inelastic collision, and a background of secondary electrons  $I_s(E_f, h)$ , which have suffered an energy loss in one or more collisions.

$$I_{total}(E_f, h) = I_p(E_f, h) + I_s(E_f, h) \quad (1.13)$$

The  $\mathcal{I}_p(E_f, \hbar)$  in Eq. (1.13) can be factorized into a distribution of photoelectrons  $\mathcal{I}(E_f, \hbar)$ , a transmission function  $T(E_f, \hbar)$ , and an escape function  $D(E_{kin})$  [49]. For each pair of initial and final states,

$$\mathcal{I}_p(\mathbf{k}, \mathbf{G}) = \mathcal{I}(\mathbf{k}, \hbar) T(E_f, \hbar) D(E_f) \quad (1.14)$$

Usually, the transmission factor  $T(E_f, \hbar)$  is calculated in terms of the electron mean free path  $\ell_e(E_f)$  and the photon penetration depth  $\lambda_{ph}(\hbar)$  [44],

$$T(E_f, \hbar) = \frac{\ell_e(E_f) / \lambda_{ph}(\hbar)}{1 + \ell_e(E_f) / \lambda_{ph}(\hbar)} \quad (1.15)$$

The typical values of  $\ell_e(E_f)$  and  $\lambda_{ph}(\hbar)$  are  $\sim 5 - 20 \text{ \AA}$  and  $\sim 100 - 200 \text{ \AA}$ , respectively [49]. Therefore,  $T(E_f, \hbar)$  can be replaced by  $\ell_e(E_f) / \lambda_{ph}(\hbar)$ . Under the assumption that the inelastic scattering frequency  $1/\tau$  is isotropic and only depends on  $E_f$ , the electron mean free path can be described as

$$\ell_e(E_f) = |\nabla_{\mathbf{k}} E_f(\mathbf{k})| / \hbar \quad (1.16)$$

A classical expression for the escape factor  $D(E_f)$  is

$$D(E_f) = \begin{cases} 0 & : E_f(\mathbf{k}) - E_{vac} < \hbar^2(\mathbf{k}_{\parallel} + \mathbf{G}_{\parallel})^2 / 2m \\ 1 & : E_f(\mathbf{k}) - E_{vac} \geq \hbar^2(\mathbf{k}_{\parallel} + \mathbf{G}_{\parallel})^2 / 2m \end{cases} \quad (1.17)$$

which simply describes the fact that the beam will be completely reflected if the momentum component normal to the surface is insufficient to surmount the surface barrier.

Assembling all these ingredients of the model and taking into account the conservation of wave vector in Eq. (1.8), the final expression for  $\mathcal{I}_p(E_f, \hbar)$  is given by:

$$\begin{aligned} \mathcal{I}_p(E_f, \hbar) \propto \int d^3\mathbf{k} \mathcal{I}(\mathbf{k}_{\parallel}, \mathbf{G}_{\parallel}) \times (\mathbf{k}_{\parallel} + \mathbf{G}_{\parallel} - \mathbf{K}_{\parallel}) \\ \cdot [\mathbf{E}_f(\mathbf{k}) - \mathbf{E}_i(\mathbf{k}) - \hbar] \times [\mathbf{E}_f - \mathbf{E}_f(\mathbf{k})] \end{aligned} \quad (1.18)$$

For the first step of the three step model, a  $N$ -electron ground state  $\Psi_i^N$  to a final state  $\Psi_f^N$  including a photoelectron. Applying the Fermi's Golden Rule [50] to the optical transition probability, we have:

$$I \propto \sum_{f,i} w_{fi} = \sum_{f,i} \frac{2}{\hbar} |\langle \Psi_f^N | H_{int} | \Psi_i^N \rangle|^2 (E_f^N - E_i^N - \hbar) \quad (1.19)$$

where  $E_i^N = E_i^{N-1} - E_B^{\mathbf{k}}$  and  $E_f^N = E_f^{N-1} + E_{kin}$  are the initial and final-state energies of the  $N$ -particle system ( $E_B^{\mathbf{k}}$  is the binding energy of the photoelectron with kinetic energy  $E_{kin}$  and momentum  $\mathbf{k}$ ).  $\Psi_i$  and  $\Psi_f$  denote wave-functions of the initial state and the final state, respectively.  $H_{int}$  describes the electron-photon interaction:

$$H_{int} = \frac{e}{2m c} (\mathbf{A} \cdot \mathbf{p} + \mathbf{p} \cdot \mathbf{A}) = \frac{e}{m c} \mathbf{A} \cdot \mathbf{p} \quad (1.20)$$

where  $\mathbf{A}$  is the vector potential, which represents the photon field,  $\mathbf{p}$  is the electronic momentum operator, and we made use of the commutator  $[\mathbf{p}, \mathbf{A}] = i\hbar \nabla \cdot \mathbf{A}$ . With the dipole approximation (i.e.,  $\mathbf{A}$  being a constant over atomic dimensions, which is true in the ultraviolet regime),

$$w_{fi} \propto |\langle \Psi_f^N | \mathbf{r} | \Psi_i^N \rangle|^2 (E_f^N - E_i^N - \hbar) \quad (1.21)$$

In the independent particle picture,  $\Psi_i^N$  is a product of one-particle wave functions following the Hartree-Fock formalism. For  $\Psi_f^N$ , under *sudden approximation*, that is, the photoelectron is assumed not to have any interaction with the system left behind (which implies two independent wave functions), and the effective potential changes discontinuously in time from that of the initial  $N$ -electron system to that of the final system of  $(N - 1)$ -electron plus a photohole. Note that this is not necessarily true for low kinetic energy photoelectrons, which may need a longer time than the system response to leave the system. In the latter case, or the so-called *adiabatic limit*, the detailed screening of photoelectron and photohole have to be taken into account[51]. The sudden approximation is justified for the cuprates even at photon energies as low as 20 eV[52], see section 1.3.4). Within these approximations, we can write  $\Psi_i^N$  and

$\Psi_f^N$  as:

$$\Psi_i^N = \mathcal{A} \begin{smallmatrix} \mathbf{k} \\ i \end{smallmatrix} \Psi_i^{N-1} \quad \Psi_f^N = \mathcal{A} \begin{smallmatrix} \mathbf{k} \\ f \end{smallmatrix} \Psi_f^{N-1} \quad (1.22)$$

where  $\begin{smallmatrix} \mathbf{k} \\ i \end{smallmatrix}$  and  $\begin{smallmatrix} \mathbf{k} \\ f \end{smallmatrix}$  are the wave functions of the (photo)-electron with momentum  $\mathbf{k}$  before and after the optical transition,  $\Psi_i^{N-1}$  and  $\Psi_f^{N-1}$  describe the remaining  $(N-1)$ -electron system, and  $\mathcal{A}$  is an antisymmetric operator for fermion wave functions. One then has

$$\langle \Psi_f^N | \mathbf{r} | \Psi_i^N \rangle = \langle \begin{smallmatrix} \mathbf{k} \\ f \end{smallmatrix} | \mathbf{r} | \begin{smallmatrix} \mathbf{k} \\ i \end{smallmatrix} \rangle \langle \Psi_f^{N-1} | \Psi_i^{N-1} \rangle \quad (1.23)$$

where  $M_{f,i}^{\mathbf{k}} \equiv \langle \begin{smallmatrix} \mathbf{k} \\ f \end{smallmatrix} | H_{int} | \begin{smallmatrix} \mathbf{k} \\ i \end{smallmatrix} \rangle$  is the one-electron dipole matrix element and the second term is the  $(N-1)$ -electron overlap integral.

Because the remaining electrons will feel the potential of the photohole, and  $\Psi_f^{N-1}$  will not be one of the eigenstates of the  $(N-1)$ -electron Hamiltonian. It will relax to one of the eigenstates of the  $(N-1)$ -particle,  $\Psi_{s,i}^{N-1}$ , with eigen energy  $E_s^{N-1}$ . Also  $\Psi_i^{N-1}$ , which is *not* an eigenfunction of the  $(N-1)$ -particle Hamiltonian. The total photoemission intensity measured at a fixed momentum  $\mathbf{k}$  as a function of  $E_{kin}$

$$I(\mathbf{k}, E_{kin}) \propto \sum_{f,i} w_{f,i} \propto \sum_{f,i} |M_{f,i}^{\mathbf{k}}|^2 \sum_s |c_{s,i}|^2 (E_{kin} + E_{s,i}^{N-1} - E_i^N - h) \quad (1.24)$$

where  $|c_{s,i}|^2 = |\langle \Psi_{s,f}^{N-1} | \Psi_i^{N-1} \rangle|^2$  is the probability that the removal of an electron from orbital  $\mathbf{k}$  will leave the  $(N-1)$ -particle system in the excited state  $s$ . In the strongly correlated systems many of the  $|c_{s,i}|^2$  will be different from zero because a large number of eigenstate  $\Psi_{s,i}^{N-1}$  is participating in the final state and, as a consequence of the (sudden) change of potential,  $\Psi_i^{N-1}$  will *not* be orthogonal to many of the  $\Psi_{s,i}^{N-1}$ . Therefore, the ARPES spectra will not consist of single delta functions but will show a main line and several satellites according to the number of excited states  $s$  created in the process. For a weakly interacting system, under *frozen orbital approximation*,  $\Psi_f^{N-1} = \Psi_i^{N-1}$ , one only observes the main line.

### One-particle spectral function

If we rewrite the eq. 1.24 as

$$\mathcal{I}(\mathbf{k}, E_{kin}) \propto \sum_{f,i} |\mathcal{M}_{f,i}^{\mathbf{k}}|^2 \mathcal{A}(\mathbf{k}, ) \quad (1.25)$$

is the final state electron energy.  $\mathcal{A}(\mathbf{k}, ) \equiv \sum_s |\mathcal{C}_{s,i}|^2 (E_{kin} + E_{s,i}^{N-1} - E_i^N - \hbar )$  is the so called one particle spectral function, which is directly related to the Green's function.

The propagation of a single electron in a many-body system can be described by the time-ordered one-electron Green's function  $G(\tau, \tau')$  that can be interpreted as the probability amplitude that an electron added to the system in a Bloch state with momentum  $\mathbf{k}$  at a time zero will still be in the same state after a time  $|\tau - \tau'|$ . By taking a Fourier transform,  $G(\tau, \tau')$  can be expressed in energy-momentum representation obtaining  $G(\mathbf{k}, ) = G^+(\mathbf{k}, ) + G^-(\mathbf{k}, )$ , where  $G^+(\mathbf{k}, )$  and  $G^-(\mathbf{k}, )$  indicate the one-electron addition and removal Green's function, respectively:

$$G^\pm(\mathbf{k}, ) = \sum_s \frac{|\langle \Psi_s^{N\pm 1} | \mathcal{C}_{\mathbf{k}}^\pm | \Psi_i^N \rangle|^2}{\mp E_s^{N\pm 1} \pm E_i^N \pm i} \quad (1.26)$$

where  $\epsilon$  is the excitation energy from the Fermi level (from here on  $\hbar = 1$ ), the operator  $\mathcal{C}_{\mathbf{k}}^+ = \mathcal{C}_{\mathbf{k}\sigma}^\dagger$  ( $\mathcal{C}_{\mathbf{k}}^- = \mathcal{C}_{\mathbf{k}\sigma}$ ) creates (annihilates) an electron with momentum  $\mathbf{k}$  and spin  $\sigma$  in the  $N$ -particle initial state  $\Psi_i^N$ , the summation runs over all possible  $(N \pm 1)$ -particle eigenstates  $\Psi_s^{N\pm 1}$  with eigenvalues  $E_s^{N\pm 1}$ , and  $i$  is a small positive number needed to perform the calculations in the complex plane.

In the limit  $\epsilon \rightarrow 0$ ,  $(x \pm i)^{-1} = \mathcal{P}(1/x) \mp i\pi \delta(x)$ , where  $\mathcal{P}$  denotes the principle value. The *one-particle spectral function*  $\mathcal{A}(\mathbf{k}, ) = \mathcal{A}^+(\mathbf{k}, ) + \mathcal{A}^-(\mathbf{k}, ) = -(1/\epsilon) \text{Im } G(\mathbf{k}, )$ , with:

$$\mathcal{A}^\pm(\mathbf{k}, ) = \sum_s |\langle \Psi_s^{N\pm 1} | \mathcal{C}_{\mathbf{k}}^\pm | \Psi_i^N \rangle|^2 \delta(\mp E_s^{N\pm 1} \pm E_i^N) \quad (1.27)$$

Note that  $\mathcal{A}^-(\mathbf{k}, )$  and  $\mathcal{A}^+(\mathbf{k}, )$  define precisely the one-electron removal and addition spectra one probes with direct and inverse photoemission, respectively. Invoking

once again the sudden approximation, the intensity measured in an ARPES experiment on a 2D single-band system can now be written as:

$$\mathcal{I}(\mathbf{k}, \epsilon) \propto \sum_{f,i} |\mathbf{M}_{f,i}^{\mathbf{k}}|^2 \mathcal{F}(\epsilon) \mathcal{A}(\mathbf{k}, \epsilon) \quad (1.28)$$

where  $\mathbf{k} = \mathbf{k}_{\parallel}$  is the in-plane electron momentum,  $\epsilon$  is the electron energy with respect to the Fermi level. The Fermi function  $\mathcal{F}(\epsilon) = (\epsilon^{\omega/k_B T} + 1)^{-1}$

With the Green's function formalism, one can utilize the *quasiparticle* concept to study many body effects in solids. This allows the definition of the electron *proper self-energy*  $\Sigma(\mathbf{k}, \epsilon) = \Sigma'(\mathbf{k}, \epsilon) + i\Sigma''(\mathbf{k}, \epsilon)$ , which contains all the information on the energy renormalization ( $\Sigma'$ ) and lifetime ( $\Sigma''$ ) of an electron (with band energy  $\epsilon_k$  and a momentum  $\mathbf{k}$ ) propagating in a many-body system. The spectral function  $\mathcal{A}(\mathbf{k}, \epsilon)$  is a continuous function that contains full information of a single electron or hole excitation in a many-body system, and we can write:

$$\mathcal{G}(\mathbf{k}, \epsilon) = \frac{1}{\epsilon - \epsilon_{\mathbf{k}} - \Sigma(\mathbf{k}, \epsilon)} \quad (1.29)$$

$$\mathcal{A}(\mathbf{k}, \epsilon) = \frac{1}{\pi} \frac{\Sigma''(\mathbf{k}, \epsilon)}{[\epsilon - \epsilon_{\mathbf{k}} - \Sigma'(\mathbf{k}, \epsilon)]^2 + [\Sigma''(\mathbf{k}, \epsilon)]^2} \quad (1.30)$$

Because  $\mathcal{G}(\tau, \tau')$  is a linear response function to an external perturbation, the real and imaginary part of its Fourier transform  $\mathcal{G}(\mathbf{k}, \epsilon)$  have to satisfy causality and, therefore, are related by Kramers-Kronig relations. This implies that, if the full  $\mathcal{A}(\mathbf{k}, \epsilon) = -(1/\pi) \text{Im} \mathcal{G}(\mathbf{k}, \epsilon)$  is available from photoemission and inverse photoemission, one can calculate  $\text{Re} \mathcal{G}(\mathbf{k}, \epsilon)$  and then obtain both the real and imaginary part of the self-energy directly from Eq. 1.29. However, due to the lack of inverse photoemission data, this analysis is usually performed only on the basis of ARPES spectra under certain assumptions[53].

### Spectral function of a Fermi liquid

In general, the exact calculation of  $\Sigma(\mathbf{k}, \epsilon)$  and, in turn, of  $\mathcal{A}(\mathbf{k}, \epsilon)$  is an extremely hard task. In reality, usually weak interactions or certain analytical properties of the



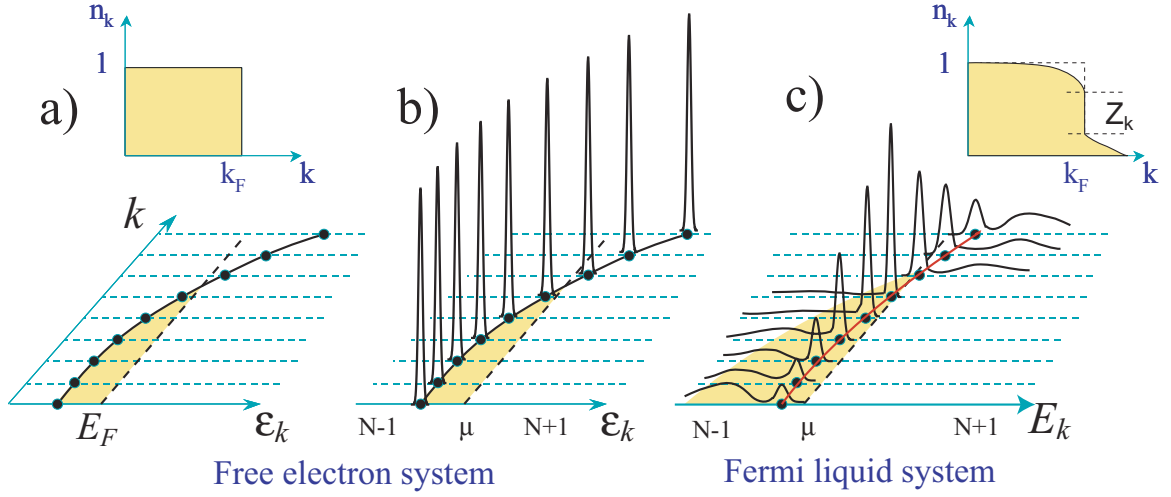


Figure 1.7: Cartoon picture of (a) a free electron band, (b) free electron spectral function, and (c) quasi particle spectral function of a Fermi liquid. The top of (a) and (c) are the density of state for free electron and the Fermi liquid quasiparticle respectively.

Green's function are assumed. Fermi liquid theory is a successful example of this, which could be a good starting point to discuss the data even in the presence of strong correlation.[54].

In a non-interacting case,  $\Sigma(\mathbf{k}, \omega) = 0$ , the independent electron dispersion is sketched in Fig.1.7(a). One can easily find that  $G^\pm(\mathbf{k}, \omega) = 1/(\omega - \epsilon_k \pm i0)$  has only one pole for each  $\mathbf{k}$ , and  $A(\mathbf{k}, \omega) = \delta(\omega - \epsilon_k)$  consists of single lines as shown in Fig.1.7(b). In this case,  $\mathbf{k}$  is a good quantum number and, for a metallic system at  $T = 0$ , the occupation number  $\hat{n}_{\mathbf{k}} = \frac{1}{2} \sum_{\sigma} c_{\mathbf{k}\sigma}^\dagger c_{\mathbf{k}\sigma}$  is characterized by a sudden drop from 1 to 0 at  $\mathbf{k} = \mathbf{k}_F$  [Fig. 1.7(a), top], which defines a sharp Fermi surface.

When the electron-electron correlation is turned on adiabatically, (so that the system remains at equilibrium), any particle added into a Bloch state has a certain probability of being scattered out of it, leaving the system in an excited state in which additional electron-hole pairs have been created. The electron occupation number  $\hat{n}_{\mathbf{k}}$  will now show a discontinuity smaller than 1 at  $\mathbf{k}_F$  and a finite occupation probability for  $\mathbf{k} > \mathbf{k}_F$  even at  $T = 0$  [Fig.1.7(c), top]. As long as  $\hat{n}_{\mathbf{k}}$  shows a finite discontinuity  $Z_{\mathbf{k}} > 0$  at  $\mathbf{k}_F$  (i.e., weak enough correlations), we can describe the correlated Fermi

sea in terms of independent *quasiparticles*, i.e. electrons *dressed* with a manifold of excited states, which are characterized by a pole structure very close to the one of the non-interacting system but with renormalized energy  $E_{\mathbf{k}}$  and mass  $m^*$ , and a finite lifetime  $\tau_{\mathbf{k}} = 1/\Gamma_{\mathbf{k}}$  (with these renormalized parameters the properties of the free electron gas can be readily extended to the FL of quasiparticles). As the bare-electron character of the quasiparticle or pole strength (also called coherence factor) is  $Z_{\mathbf{k}} < 1$ , and the total strength must be conserved (see below Eq. 1.33), we can separate  $G(\mathbf{k}, \omega)$  and  $A(\mathbf{k}, \omega)$  into a coherent pole part and an incoherent smooth part without poles:

$$G(\mathbf{k}, \omega) = \frac{Z_{\mathbf{k}}}{\omega - E_{\mathbf{k}} - i\Gamma_{\mathbf{k}}} + G_{inc} \quad (1.31)$$

$$A(\mathbf{k}, \omega) = Z_{\mathbf{k}} \frac{\Gamma_{\mathbf{k}}}{(\omega - E_{\mathbf{k}})^2 + \Gamma_{\mathbf{k}}^2} + A_{inc} \quad (1.32)$$

where, more in detail  $Z_{\mathbf{k}} = (1 - \frac{\partial \Sigma'}{\partial \omega})^{-1}$ ,  $E_{\mathbf{k}} = \epsilon_{\mathbf{k}} + \Sigma'$ ,  $\Gamma_{\mathbf{k}} = Z_{\mathbf{k}} \Sigma''$ , and the limit of validity of the FL description is  $E_{\mathbf{k}} - \mu \gg \Sigma''$ , for small  $\epsilon_{\mathbf{k}} - \mu$  and  $\mathbf{k} - \mathbf{k}_F$ . In particular, for three dimensional FL systems  $\Gamma_{\mathbf{k}} \propto [(\epsilon_{\mathbf{k}} - \mu)^2 + E_{\mathbf{k}}^2]$ . By comparing the electron removal and addition spectra for a FL of quasiparticles [Fig. 1.7(c)] with those of a free electron gas [Fig. 1.7(b)], the effect of the self energy correction becomes evident. The quasiparticle peak has now a finite lifetime (due to  $\Sigma''$ ). It sharpens up rapidly, thus emerging from the broad incoherent component, upon approaching the Fermi level where the lifetime is infinite corresponding to a well defined quasiparticle [note that coherent and incoherent part of  $A(\mathbf{k}, \omega)$  are reminiscent of the main line and satellite structure discussed in the previous section]. Furthermore, the peak position is shifted with respect to the bare band energy  $\epsilon_{\mathbf{k}}$  (due to  $\Sigma'$ ): as the quasiparticle mass is larger than the free-electron one because of the dressing ( $m^* > m$ ), the total dispersion (or bandwidth) will be smaller ( $|E_{\mathbf{k}}| < |\epsilon_{\mathbf{k}}|$ ). Among the general properties of the spectral function there are also several sum rules. A fundamental one, which was implicitly used to state that  $\int d\omega A_{qp} = Z_{\mathbf{k}}$  and  $\int d\omega A_{inc} = 1 - Z_{\mathbf{k}}$  in discussing the FL, reads:

$$\int_{-\infty}^{+\infty} d\omega A(\mathbf{k}, \omega) = 1 \quad (1.33)$$

which reminds us that  $A(\mathbf{k}, \omega)$  describes the probability of removing/adding an electron with momentum  $\mathbf{k}$  and energy  $\omega$  to a many-body system. However, as it requires also the knowledge of the electron addition part of the spectral function, it is not so useful in the analysis of ARPES data. A sum rule more relevant to this task is:

$$\int_{-\infty}^{+\infty} d\omega f(\omega) A(\mathbf{k}, \omega) = n(\mathbf{k}) \quad (1.34)$$

which relates solely the one-electron removal spectrum to the momentum distribution function  $n(\mathbf{k})$ , equivalent to the occupation number  $\hat{n}_{\mathbf{k}}$ . When electronic correlations become important and the electronic momentum  $\mathbf{k}$  is no longer a good quantum number, the discontinuity at  $\mathbf{k}_F$  is reduced (as just discussed for the FL case) but a drop in  $n(\mathbf{k})$  is usually still observable (even for strong correlations[55, 56]. Note, however, that great care is necessary in making use of Eq. 1.34 because the integral of Eq. 1.28 does not give simply  $n(\mathbf{k})$  but rather  $\mathcal{I}_0(\mathbf{k}, \omega, \mathbf{A})n(\mathbf{k})$ . Nevertheless, by tracking in momentum space the *loci* of steepest descent of the experimentally determined  $n(\mathbf{k})$  (i.e., the maxima in  $|\nabla_{\mathbf{k}} n(\mathbf{k})|$ ). For a more extended discussion on the different methods used to experimentally determine the Fermi surface [57, 58].

### Linewidth

The energy broadening and the lineshape of the quasiparticle in ARPES is determined by two factors: the contribution of the initial state (the hole state) and the contribution of the final state (the photoelectron state)[59]. If we assume that the variation of  $\text{Im}\Sigma$  is small, and the spectral function for the photohole/photoelectron are given by

$$A_h(\mathbf{k}_\perp, \omega) \propto \frac{\Gamma_h}{[\omega - \epsilon_h(\mathbf{k}_\perp)]^2 + \Gamma_h^2}; \quad A_e(\mathbf{k}_\perp, \omega) \propto \frac{\Gamma_e}{[\omega - \epsilon_e(\mathbf{k}_\perp)]^2 + \Gamma_e^2} \quad (1.35)$$

where  $\mathbf{k}_\perp$  is conserved. Summing over initial state wave vectors, the photocurrent is then given by

$$\mathcal{I}(\omega) \propto \int d\mathbf{k}_\perp \frac{\Gamma_h}{[\omega - \epsilon_h(\mathbf{k}_\perp)]^2 + \Gamma_h^2} \cdot \frac{\Gamma_e}{[\omega - \epsilon_e(\mathbf{k}_\perp)]^2 + \Gamma_e^2} \quad (1.36)$$

Evaluating this integral we obtain a Lorentzian shape for  $\mathcal{I}(\ )$  with a width of

$$\Gamma_m = \frac{\Gamma_h + \Gamma_e \left| \frac{v_h^\perp}{v_e^\perp} \right|}{\left| 1 - \frac{v_h^\perp}{v_e^\perp} \right|} \quad (1.37)$$

with  $v_h^\perp$  and  $v_e^\perp$  being the group velocities for the hole and the photoelectron, respectively, which are defined as  $v_h^\perp = E_h / k_\perp$ ,  $v_e^\perp = E_e / k_\perp$ . In the limit when  $|v_h^\perp|$  is much smaller than  $|v_e^\perp|$ , *i.e.*, when the energy dispersion of the initial-state band perpendicular to the sample surface is very small, Eq. (1.37) is reduced as

$$\Gamma_m = \Gamma_h + \Gamma_e \left| \frac{v_h^\perp}{v_e^\perp} \right| \quad (1.38)$$

In the case of Bismuth family of cuprates, the system is fairly two dimensional, and the band dispersion perpendicular to the  $\text{CuO}_2$  plane (or the cleaved surface) or  $v_h^\perp$  is very small, we may identify  $\Gamma_m$  with  $\Gamma_h$ .

## Chapter 2

# Superconducting peak in cuprates

In this chapter<sup>1</sup>, we show that the doping and temperature dependence of photoemission spectra near the Brillouin zone boundary of  $\text{Bi}_2\text{Sr}_2\text{CaCu}_2\text{O}_{8+\delta}$  exhibit unexpected sensitivity to the superfluid density (or more strictly condensate fraction). In the superconducting state, the photoemission peak intensity as a function of doping scales with the superfluid density and the condensation energy. As a function of temperature, the peak intensity shows an abrupt behavior near the superconducting phase transition temperature where phase coherence sets in, rather than near the temperature where the gap opens. This anomalous manifestation of collective effects in single-particle spectroscopy raises important questions concerning the mechanism of high-temperature superconductivity. Moreover, we show that this peak is ubiquitous in single particle excitation spectrum measured by ARPES and or tunnelling experiment for various cuprate systems, which suggest that it could be a crucial ingredient of the high temperature superconductivity.

---

<sup>1</sup>The major content of this chapter has been published in D. L. Feng *et al.*, *Science*, Vol. 289, 277 (Jul. 2000) .

## 2.1 Introduction

The collective nature of superconductivity manifests itself contrastingly in different techniques. Microwave and muon spin relaxation measurements are inherently sensitive to the collective motion of the condensate, whereas single-electron tunnelling spectroscopy and photoemission mainly probe single-particle excitations of the condensate. Hence, these two types of spectroscopies can be used to measure two essential but distinct ingredients of superconductivity: the superfluid density, which characterizes the phase coherence of the Cooper pairs, and the superconducting energy gap, which reflects the strength of the pairing.

For a simple metal in its normal state, as we have discussed in Chapter 1, the position of the sharp feature measured by ARPES reflects the band dispersion [Fig. 2.1(a)]. In the superconducting state (at the same wave vector), the position of the feature is pushed to higher binding energy, because of the opening of a superconducting gap, and the intensity of the feature is reduced because of the particle hole mixing effects or the Cooper pair formation. An exaggerated version of this change in the spectral function is illustrated in [Fig. 2.1(b)]. In this conventional Bardeen-Cooper-Schrieffer (BCS) picture, there is no direct information about the phase coherence in the single particle excitation spectrum as measured by ARPES.

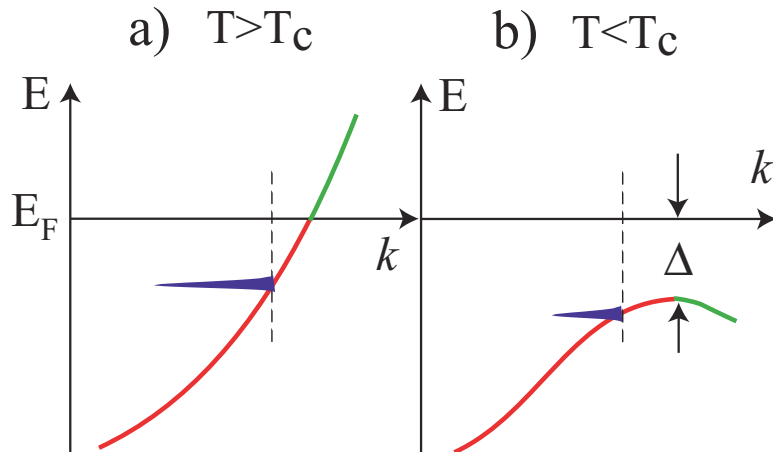


Figure 2.1: Single electron excitation spectrum for a conventional BCS superconductor in the (a) normal and (b) superconducting states.

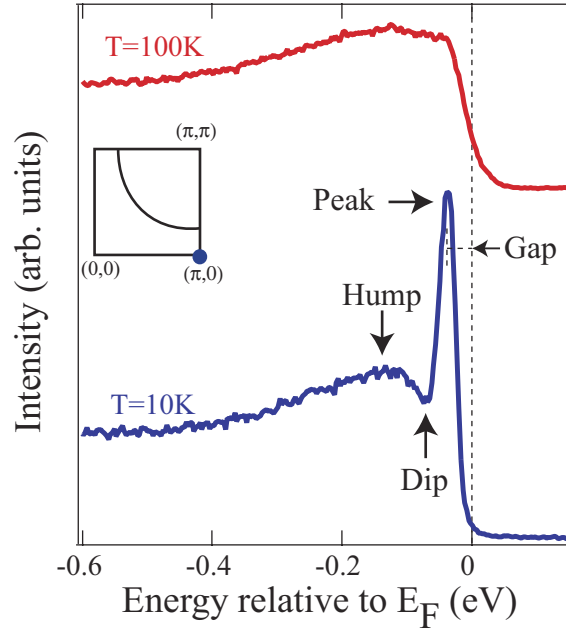


Figure 2.2: ARPES spectrum of optimally doped Bi2212 ( $T_c = 90\text{K}$ ) in normal and superconducting states at  $(0,0)$ . Inset shows the Fermi surface sketch.

The situation is different for the high temperature superconductors such as Bi2212. As shown in Fig.2.2, instead of a shift of the the normal state feature position, a sharp peak seems to be created upon the superconducting phase transition near the Brillouin zone boundary  $(\pi/a, 0)$ ,<sup>2</sup> forming the famous peak-dip-hump structure [61, 62, 63, 64, 65, 66]. This feature has so far been discussed primarily in the context of quasi-particle excitations coupled to many-body collective excitations[63, 67, 68]. In this chapter, we show that it indicates a pronounced departure from the above conventional picture. Namely, the peak intensity contains information about the phase coherence, in addition to its position corresponding to the pairing strength (or superconducting gap).

we show that the doping dependence of the peak intensity exhibits a clear resemblance to the behavior exhibited by the superfluid density  $n_s$  and the condensation energy, both of which scale approximately with dopant  $x$  in the underdoped regime and saturate or scale with  $A - x$  in the overdoped regime (where  $A$  is a constant). The

<sup>2</sup> $a$  is the lattice constant, which is set to unity for convenience in the literature

temperature dependence of this peak intensity also shows a resemblance to that of the superfluid density. More important, this peak intensity shows an abrupt behavior near  $T_c$ , where phase coherence sets in, rather than at  $T^*$ , the temperature where the pseudogap opens in the underdoped regime[69]. It is remarkable that the signature of these collective properties appears in a single-particle excitation spectrum at  $(\pi, 0)$  (the antinode region of a d-wave state with maximum gap). This anomalous manifestation of the superfluidity as well as  $x$  dependence of many physical quantities contrasts strongly with the conventional BCS type of picture based on the Fermi liquid. In that picture, the quasi-particle spectral weight  $Z$  depends on interactions and the energy gap near the normal state Fermi surface whose volume scales with  $1 - x$  (counting electrons), rather than on the superfluid density. Instead, these observations agree well with theories that are based on the doped Mott insulator.

## 2.2 Experimental

We measured ARPES spectra on Bi2212 samples with various doping levels. Bi2212 samples are labelled by their  $T_c$  with the prefix UD for underdoped, OP for optimally doped, or OD for overdoped (e.g., an underdoped  $T_c = 83$  K sample is denoted UD83). Samples used here include traveling-solvent floating zone-grown single crystals and molecular beam epitaxy (MBE)-grown films. The typical transition width is less than 1 K, except for UD73, which has a transition width of 7 K. Samples with different  $T_c$  's are of similar high quality, as assessed by the measured residual resistivity ratio (RRR), the ratio between the extrapolated resistivity at  $T = 0$  K and resistivity at  $T = 300$  K. The hole doping level  $x$  was determined by the empirical relation  $T_c = T_{c,max}[1 - 82.6(x - 0.16)^2]$ [70].  $T_{c,max} = 91$  K was used for all the samples because the chemical dopants used in this study (Dy or O) are doped out of the CuO<sub>2</sub> plane[71], which changes the doping level but results in much weaker scattering effects than impurities doped in the CuO<sub>2</sub> plane (e.g., Zn). The samples measured in the experiments as well as those cited from Ref.[66] (named in lowercase) are summarized in Table 2.1.

The data were collected at Stanford Synchrotron Radiation Laboratory (SSRL)



Table 2.1: Summary of the Bi2212 samples used in this chapter

Sample	Chemical formula	texture	$T_c$ (K)	$\Delta T_c$ (K)	doping
UD30	$Bi_{1.2}Sr_{1.2}Ca_{0.7}Dy_{0.3}Cu_2O_{8+\delta}$	film	30	1	0.07
UD46	$Bi_{1.2}Sr_{1.2}Ca_{0.9}Dy_{0.1}Cu_2O_{8+\delta}$	film	46	1	0.084
ud55	$Bi_{1.2}Sr_{1.2}CaCu_2O_{8+\delta}$	film	55	not available	0.09
UD73	$Bi_{1.2}Sr_{1.2}CaCu_2O_{8+\delta}$	crystal	73	7	0.112
ud75	$Bi_{1.2}Sr_{1.2}CaCu_2O_{8+\delta}$	crystal	75	not available	0.115
ud83	$Bi_{1.2}Sr_{1.2}CaCu_2O_{8+\delta}$	crystal	83	not available	0.127
UD83	$Bi_{1.2}Sr_{1.2}CaCu_2O_{8+\delta}$	crystal	83	1	0.127
ud89	$Bi_{1.2}Sr_{1.2}CaCu_2O_{8+\delta}$	crystal	89	not available	0.145
OP91	$Bi_{1.2}Sr_{1.2}CaCu_2O_{8+\delta}$	crystal	91	1	0.16
OD88	$Bi_{1.2}Sr_{1.2}CaCu_2O_{8+\delta}$	crystal	88	1	0.18
OD79	$Bi_{1.2}Sr_{1.2}CaCu_2O_{8+\delta}$	crystal	79	1	0.2
OD75	$Bi_{1.2}Sr_{1.2}CaCu_2O_{8+\delta}$	crystal	75	1	0.205
ud72	$Bi_{1.2}Sr_{1.2}CaCu_2O_{8+\delta}$	crystal	72	not available	0.21

using 22.4eV synchrotron light. The data shown in Fig. 2.3 and Fig. 2.4, (a) to (e), were collected at beamline V-4 with an overall energy resolution of 15 meV. The data shown in Fig. 2.5 were collected at beamline V-3 with overall energy resolutions of 30 to 50 meV and an angular resolution of  $\pm 0.045^\circ$ . The chamber pressure was better than  $4 \times 10^{-11}$  torr during the measurements.

## 2.3 Results

For both the UD83 ( Fig. 2.3(a)) and the OD84 ( Fig. 2.3(b)) Bi2212 samples, the spectra near the  $(\pi, 0)$  show the peak-dip-hump structure. These features are clearly distinct below  $T_c$  and persist slightly above  $T_c$ , as shown in insets 2 and 3 of Fig. 2.3. Moreover, a normal-state pseudogap is present in the underdoped sample but not in the overdoped sample (at least for the 110 K spectra)[72]. The intensity of the peak in the overdoped sample is much higher than that in the underdoped sample.

To quantify the peak intensity, we focus on the relative peak intensity normalized by the intensity of the entire spectrum. This quantity, which we call the superconducting peak ratio (SPR), makes it possible to compare data taken on different samples

with different dopings and under different experimental conditions. We extracted the peak (as illustrated in Fig. 2.4(a) using the spectrum of OD84 at  $T = 10$  K) by fitting the broad hump of the spectra with a five-parameter phenomenological formula,

$$y = a_1 \frac{1}{e^{(x-a_2)/a_3} + 1} (1 + a_4(x - a_5)^2)$$

where the  $a_i$ 's ( $i = 1, 2, 3, 4, 5$ ) are the fitting parameters. This formula is simply the

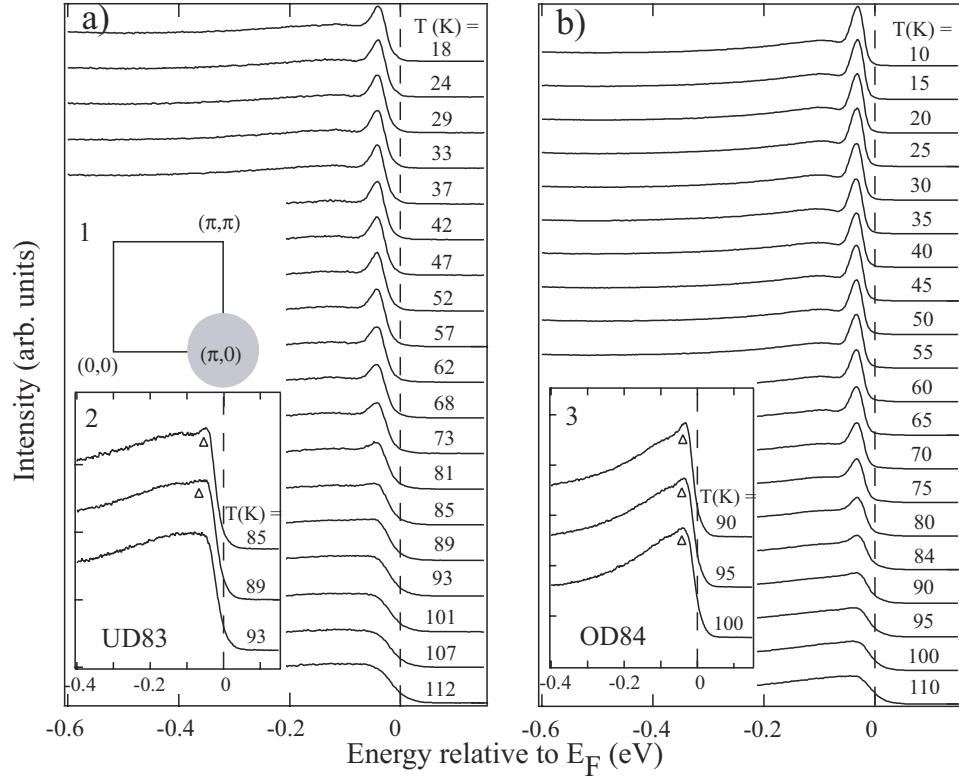


Figure 2.3: Temperature dependence of the superconducting state spectra of Bi2212 for (a) an underdoped  $T_c = 83$  K sample and (b) an overdoped  $T_c = 84$  K sample ( $E_F$ , Fermi energy). The data are collected near  $(\pi, 0)$  over the shaded circular momentum region in inset 1 to measure the overall relative change of the superconducting peak near the  $(\pi, 0)$  region and to achieve the best signal-to-noise ratio for detailed comparison. Insets 2 and 3 are enlargements of spectra taken above  $T_c$ ; the open triangle markers show that the superconducting peak exists at temperatures slightly above  $T_c$ .

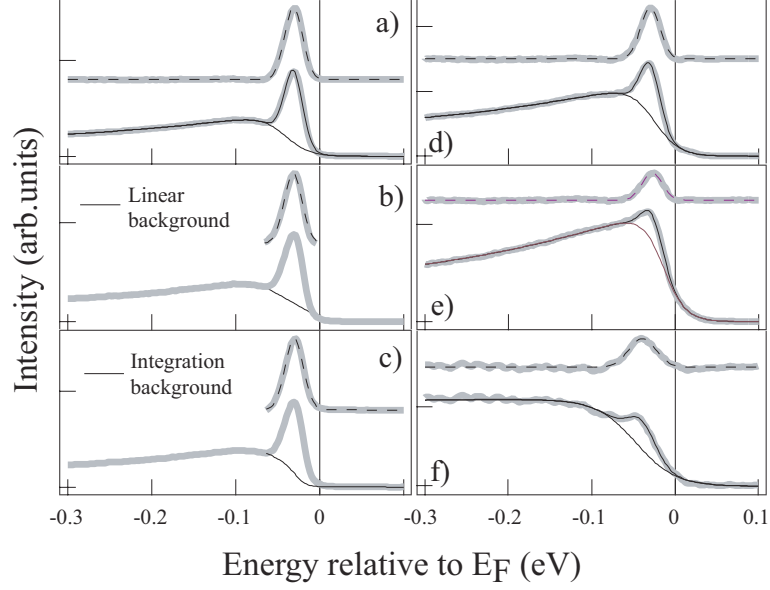


Figure 2.4: Various ways of extracting the superconducting peak: (a) fitting the hump feature with Eq. 1, (b) subtracting a linear background, and (c) subtracting an integration background for the spectrum of OD84 at  $T = 10$  K. The same procedure shown in (a) is also applied for (d) the spectrum of OD84 at  $T = 80$  K, (e) the spectrum of OD84 at  $T = 90$  K, and (f) the spectrum of UD55 at  $T = 15$  K [taken from Ref.[66]]. In each panel, the lower shaded curves are the raw spectra; the upper shaded curves are the extracted superconducting peaks, which are fitted by a Gaussian function (dashed lines). In (a), (d), (e), and (f), both the fits for the hump feature and the full fits are shown as solid curves.

product of the Fermi function ( $a_3$  is not the temperature) and a parabolic function, and the fit is very robust. The remaining peak then can be fitted by a Gaussian or a Voigt function. The SPR is defined as the ratio between the extracted peak intensity and the total spectrum intensity integrated over  $[-0.5 \text{ eV}, 0.1 \text{ eV}]$ , and this integration window covers the energy scale of the dispersion. We have also used other integration windows, which did not change the qualitative behaviors discussed here. Because there are certain subjective factors in the fitting procedure, we have also extracted the peak by subtracting a linear background (Fig. 2.4(b)) and an integration (Shirley) background (Fig. 2.4(c)), which gave similar results. The SPR values obtained in Fig. 2.4, (a) to (c), are 0.139, 0.127, and 0.142, respectively. Therefore, errors due to possible subjective factors in the fitting procedure can be estimated to be smaller

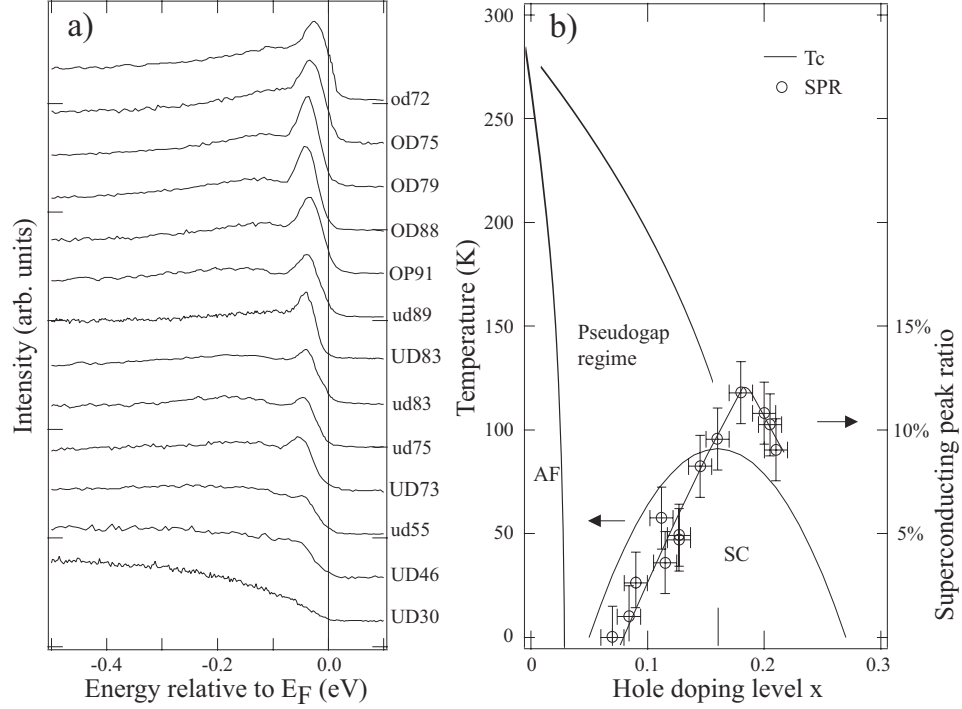


Figure 2.5: (a) Doping dependence of the superconducting state spectra of Bi2212 at  $(\pi, 0)$  taken at  $T \ll T_c$ . Data from samples marked in lowercase are taken from [66]. (b) The doping dependence of SPR is plotted over a typical Bi2212 phase diagram for the spectra in (a). The solid line is a guide to the eye. Horizontal error bars denote uncertainty in determining the doping level ( $\pm 0.01$ ); vertical error bars denote uncertainty in determining the SPR ( $\pm 1.5\%$ ). AF, antiferromagnetic regime; SC, superconducting regime.

than 0.01 to 0.02. We chose the phenomenological formula (Eq. 1) for our analysis, because it can smoothly fit the entire hump feature, and we have estimated the errors to be  $\pm 1.5\%$  to reflect the subjective uncertainty. This fitting procedure also works well in cases where the peak is small and the dip is weak (Fig. 2.4, (d) to (f)). We stress that the qualitative trends are independent of any given choice of fitting procedure or energy integration window.

Low-temperature spectra (Fig. 2.5(a)) were collected at  $(\pi, 0)$  and at  $T = 10$  to  $20$  K  $\ll T_c$  for different doping levels. The peak is not observed in very underdoped samples, but starts to appear as a small bump in spectrum ud55. Upon further increase of doping, the peak intensity increases until slightly above optimal doping

and then decreases in the strongly overdoped regime where the dip disappears. This systematic increase of the peak intensity in the underdoped regime is consistent with earlier data [63, 72, 73]. The SPR is plotted against the hole doping level  $x$  in Fig. 2.5(b); the SPR increases with doping and reaches a maximum slightly above optimal doping as defined by  $T_c$ , then decreases in the strongly overdoped regime. We stress here that the ratio of the two parts of the spectra—not just the absolute peak intensity—is changing with doping. Our  $k$ -dependent data from a few doping levels indicate that the behavior shown in Fig. 2.5(b) holds for various points in  $k$  space near  $(\pi, 0)$ .

Although scanning tunnelling microscopy experiments[71] have found that both the superconducting gap size and the peak intensity are smaller near the scattering centers (impurities or defects), we believe the systematics seen in our “spatially averaged” data are mainly derived from doping for several reasons. First, we do not see a clear correlation between the SPR and residual resistivity, which is a measure of impurity levels. For example, the RRRs of OP91, OD79, and UD30 are ordered as  $\text{RRR}(\text{OP91}) < \text{RRR}(\text{OD79}) \gg \text{RRR}(\text{UD30})$ , whereas the SPRs of these samples are ordered as  $\text{SPR}(\text{UD30}) \ll \text{SPR}(\text{OP91}) < \text{SPR}(\text{OD79})$  (Fig. 2.5(b)). Second, the same behavior of the SPR is observed in samples doped by either Dy or oxygen, which are located at different crystal sites. Third, given the narrow transition widths of most of the samples, it is unlikely that the impurity effects are dominant. Finally, the systematic doping behaviors of the superconducting gap and pseudogap in these samples are consistent with many other measurements.

In comparing the doping and temperature dependence of the SPR with several ground-state quantities related to the superfluidity (Fig. 2.6), we assume a universality of the properties of the cuprates, because not all the quantities are measured in the Bi2212 system. Our data lend further support to the universality of the doping-dependent behavior of many quantities observed in Bi2212,  $\text{YBa}_2\text{Cu}_3\text{O}_{7-y}$  (YBCO), and  $\text{La}_{2-x}\text{Sr}_x\text{CuO}_{4+\delta}$  (LSCO); because of various experimental difficulties, few systematic studies have been performed on Bi2212 by other techniques. As a function of doping, we find a remarkable resemblance of the SPR (Fig. 2.6(a)) to the low-temperature superfluid density as measured by muon spin relaxation

( $\mu$ SR) (Fig. 2.6(b))[74, 75], to the condensation energy from the specific heat ( $C_p$ ) measurements[74], and to the specific heat coefficient jump [ $\Delta_c \equiv C_p(T_c) - C_p(120K)$ ],

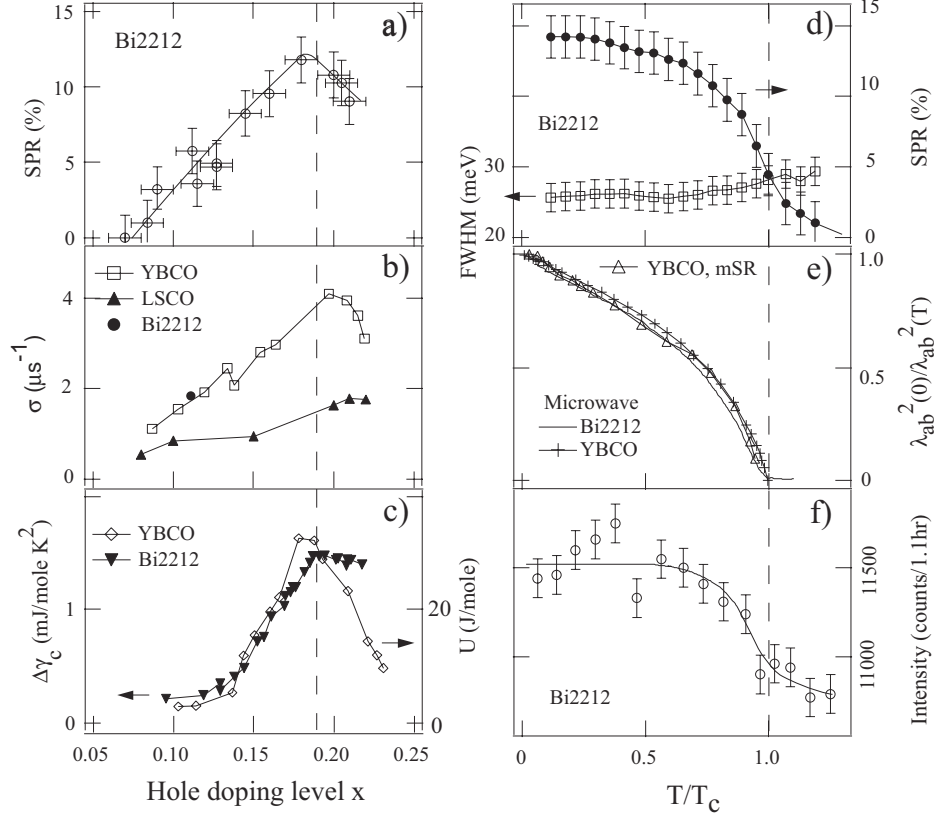


Figure 2.6: (a to c) Low-temperature doping dependence for (a) the SPR of Bi2212 reproduced from Fig. 2.5(b); (b) the  $\mu$ SR relaxation rate  $s$  (proportional to superfluid density) for YBCO [from Ref.[74]], LSCO, and Bi2212 [from Ref. [75]]; and (c) the specific heat coefficient jump  $\Delta_c$  of Bi2212 [from Ref. [76]] and the condensation energy  $U$  of YBCO [from Ref. [74]]. The dashed line through (a), (b), and (c) is  $x = 0.18$ , serving as a guide to the eye. (d to f) Temperature dependence of (d) the SPR and the peak full width at half-maximum (FWHM) for OD84 data shown in Fig. 2.3(b); (e)  $\lambda_{ab}^2(0)/\lambda_{ab}^2(T)$  (proportional to superfluid density), where  $\lambda_{ab}$  is the penetration depth, measured by microwave spectroscopy for OP91 Bi2212 [from Ref. [96]] and OP93.2 YBCO [from Ref. [97]] and by  $\mu$ SR for OP93.2 YBCO [from Ref. [98]]; and (f) the neutron (p,p) resonance mode intensity [from Ref. [94]] for an OD83 Bi2212.

where  $\rho \equiv C_p/T$ ] (Fig. 2.6(c))[76]. In each of these cases, the physical quantity increases with doping, reaching the maximum slightly above the optimal doping, and then decreases or saturates in the strongly overdoped regime. The decrease of the SPR in the overdoped regime has not been explicitly stated in the published literature.

Upon increasing the temperature, the SPR decreases slowly until about  $0.7 T_c$ , then decreases rapidly to zero at a temperature slightly above  $T_c$  (Fig. 2.6(d)). This temperature dependence suggests that the peak is related to phase coherence and not to the energy gap, because in the underdoped samples, the pseudogap opens well above  $T_c$  but the sharp peak shows up only slightly above  $T_c$ . This temperature dependence of the SPR qualitatively resembles that of  $n_s$  as measured by microwave and  $\mu$ SR experiments (Fig. 2.6(e)). The microwave and  $\mu$ SR results from the YBCO system are very similar to those from the Bi2212 system, partially justifying our assumption of system universality in the above discussion.

## 2.4 Discussion

The SPR clearly tracks the superconducting properties measured by microwave and  $\mu$ SR experiments, but there are several discrepancies. First, the  $n_s$  measured in these experiments goes to zero at  $T_c$ , instead of persisting slightly above  $T_c$ . This discrepancy may be related to the difference in the time scales of the measurements, as photoemission is a much faster probe than microwave measurements or  $\mu$ SR. It has been shown that terahertz optical experiments, a much faster probe than the usual microwave measurements, are sensitive to short-range phase coherence above  $T_c$  [77]. Second, in the low-temperature regime, the microwave and  $\mu$ SR data exhibit linear temperature dependence, whereas the SPR shows signs of saturation. This may be attributed to the fact that the SPR is obtained from spectra near the  $(\pi, 0)$  region, where the superconducting gap energy is much larger than the thermal energy. Hence, further lowering the temperature at already low temperatures will not affect the SPR. On the other hand, microwave and  $\mu$ SR experiments measure the overall superfluid density, which is always affected by nodal quasi-particle excitations, and thus lowering the temperature will increase the measured superfluid density by reducing the number

of thermally excited quasi-particles. This also suggests that although the SPR is closely related to the superfluid density, it is still different from superfluid density. The question is: why is the intensity of the single-particle excitation near the antinode of a d-wave superconductor related to the superfluidity?

Strictly speaking, single-particle spectroscopy should not be directly related to a collective behavior like the superfluid density, however in the case of a superconductor, it could be sensitive to a sibling concept of the superfluid density, that is, the condensate fraction. Condensate fraction ( $|\Psi|^2$ ) is defined, in a two fluid picture, as the number of electrons that participate the pairing to form Cooper pairs. Superfluid density is a transport quantity, while the condensate fraction is the order parameter of a superconductor[78], and can be measured by one/two-particle probes. In conventional superconductors,  $n_s$  and  $|\Psi|^2$  have similar temperature dependence behaviors. In high temperature superconductors, this relation is believed to hold at least qualitatively<sup>3</sup>. Recently, it was shown that the neutron ( , ) resonance is actually measures the condensate fraction. This can explain the resemblance between the ARPES superconducting peak and neutron in Fig. 2.6f), especially they both show a saturation behavior at low temperature.

Having discussed why ARPES could be sensitive to the superfluid density through the condensate fraction, we still need to understand the following intriguing questions: why antinode region of a d-wave superconductor is so special, and why does the SPR scale with  $x$  in the underdoped regime? These questions cannot be reconciled within the theoretical framework of superconductivity involving BCS pairing (with either s-wave or d-wave symmetry) and excitations around a large Fermi surface. The  $x$  dependence of the SPR and other quantities requires a fundamental departure from a band-like Fermi surface-based approach in the underdoped regime. Moreover, in a BCS type of picture based on the Fermi liquid concept, the superconducting quasi-particle peak intensity  $Z$  should depend on the coherence factor that is related to the energy gap instead of the superfluid density. This theoretical picture contrasts

---

<sup>3</sup>In some exotic cases,  $|\Psi|^2$  and  $n_s$  could be very different. For example, in 2D xy model, when  $T > 0$  but below the Kosterlitz-Thouless transition temperature, the condensate fraction is zero, i.e. no condensate. However, superfluid density is finite, as phase of the system could still resist to external twist such as magnetic field through vortex/antivortex bounding.



strongly with the fact that the sharp peak in the underdoped regime rises abruptly near  $T_c$  rather than  $T^*$ , where the pseudogap opens. A related problem is that the gap is larger in the underdoped regime while the effect of superconductivity on the photoemission spectra is weaker. The Fermi liquid approach has been extended by attributing the disappearance of the sharp peak above  $T_c$  to broadening caused by phase fluctuations [79]. However, it is inconsistent with the fact that the integrated peak intensity changes continuously with temperature below  $T_c$ , whereas the peak width does not change other than by simple thermal broadening over the entire 90 K temperature range, even above  $T_c$  (Fig. 2.6(d)).

The experimental data discussed here are in agreement with the theoretical models based on the doped Mott insulator picture. There have been two classes of theoretical models—resonant valence bond (RVB) gauge theory and the stripe model—that predict the existence of the coherent spectral weight in the single-particle excitation spectrum that is proportional to  $x$ . The stripe theory envisions a microscopic phase separation that breaks the global two-dimensional (2D) system into local 1D systems of charge stripes and intervening “insulator domains” [32, 80]. Electronic structures calculated on the basis of this model reproduce the “flat band” that dominates the spectral weight near the  $(\pi, 0)$  region [81, 82, 83], which is also consistent with photoemission data from the statically charge-ordered compound [84]. The stripe theory attributes the emergence of the sharp peak below  $T_c$  to the phase coherence among the stripes via a 1D to 2D crossover [85]. In this picture, the spectral weight of the coherent part of the single-particle excitation spectrum is a monotonic function of the superfluid density rather than of the energy gap [85]. This can explain the doping and temperature dependencies of the data, as the number of stripes scales with doping  $x$  in the underdoped regime. The RVB gauge theory envisions the superconductivity to be a derived property of the doped Mott insulator, where the pairing force stems from the magnetic interaction already strongly present in the insulator, and doping destroys the residual long-range order and allows RVB pairs to move [19, 86, 87, 88, 89, 90, 91]. In this picture, an excitation is regarded as a composite of two particles. One of these particles is directly related to the phase of the superconducting order parameter. Following this assumption, this theory naturally gives rise to a coherent quasi-particle

whose strength scales with doping  $x$  (or phase stiffness) and vanishes above  $T_c$ . It has also been suggested that the coherent part is most pronounced near  $(\pi, 0)$  because of the decoupling of the two components of the composite particle in that region [91]. In addition to these two classes of theories, there is another model based on the assumption that a quantum critical point (QCP) exists near  $x = 0.19$  [74, 92, 93]. It suggests that the competing orders on both sides of this QCP cause the nonmonotonic doping behavior of many physical quantities of high-temperature superconductors, such as  $n_s$ ,  $\Delta_c$ , and  $U$  [Fig. 2.6, (b-c)].

Recent STM studies of Bi2212 shed new light on the  $x$ -dependence of the superconducting peak [101]. It is found that the intensity of the superconducting peak has a spatial distribution. It seems to be more intense in some regions of the sample surface. The density of local peak intensity maximum correlates with the hole density (not to confuse the hole dopant density with the impurities of a system). On the other hand STM studies on Bi2201 [100] shows the spatial distribution of the superconducting peak maximum region is much sparser than Bi2212. These phenomena indicate that the superconducting peak or coherence peak might be some sort of bound state between the condensate and the hole dopant. New theory is needed, but in this stage it is clear that the theory should be still based on the doped Mott insulator picture.

Several related issues and obvious questions remain to be explored. The relation between this  $(\pi, 0)$  collective and the superconducting peak near  $(\pi, 0)$  is currently under discussion [63, 67, 66, 68]. Because these are Fermi liquid-based phenomenological theories focused on the issue of the spectral lineshape [63, 66, 67, 68], they do not address the key paradox in the data, namely the anomalous correlation between the ARPES peak intensity and the condensate in the underdoped regime. Another unresolved issue is the overdoped regime, where the SPR and other physical properties either saturate or decrease. It is still an open question whether this is because the system switches to a “normal” Fermi liquid-like behavior in the overdoped regime, or is due to phase separation [95] or the existence of a QCP at  $x$  near 0.19.

## 2.5 Universality of the superconducting peak in cuprate

If the superconducting peak were really caused by the high temperature superconductivity, as suggested by various theories, it should ubiquitously exist in the spectral function of all of the high temperature superconductors. However, just one year ago, it was only observed in Bi2212. Naturally, one would ask whether it is just a specific phenomenon associated with Bi2212 or the bilayer structure.

Recently, with improved resolution and crystal quality, Lu *et al* showed that there are two peaks in the  $(\pi, 0)$  ARPES spectrum of YBCO [Fig. 2.7(a)][99]. The peak near the Fermi energy is found to be a surface state, which diminishes when the surface is disordered at high temperatures. The peak at higher binding energy, on the other hand, turns on a  $T_c$  and has very similar temperature dependent behavior as the superconducting peak of Bi2212. In fact, when the surface state peak is deducted, the resulting spectrum also has a peak-dip-hump structure, which is almost the same

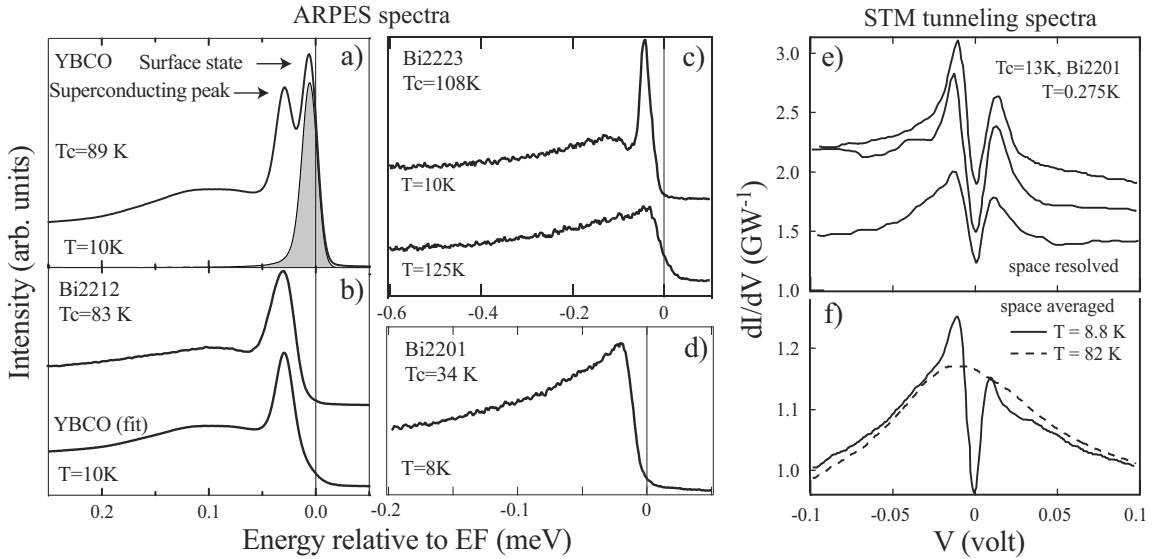


Figure 2.7: (a to d)  $(\pi, 0)$  ARPES spectra for (a) YBCO, (b) YBCO (surface state peak deducted) and Bi2212, (c) Bi2223, and (d) Bi2201. (e and f) Space resolved (e) and space averaged (f) density of state measured by STM tunnelling experiments.

as that of Bi2212 [Fig. 2.7(b)].

We recently also found the superconducting peak in the trilayer system Bi2223<sup>4</sup>. As shown in [Fig. 2.7(c)], one can see almost the same phenomenology in Bi2223 as that shown in Fig. 2.2 for Bi2212.

So far in ARPES experiments, the superconducting peak has been observed in both bilayer material (YBCO, Bi2212), and trilayer systems (Bi2223). However, it is not observed in single layer systems such as LSCO, Bi2201. [Fig. 2.7(d)] presents our recent effort with the state-of-art apparatus and excellent quality crystal. Experiments were conducted at  $T = 8$  K on an optimally doped Bi2201 with a  $T_c$  of 34 K. The overall energy resolution is about 6 meV (10-90%), yet the superconducting peak cannot be observed. This is probably due to the low superfluid density in Bi2201 and the fact that the measuring temperature (10 to 20 K) is a large fraction of  $T_c$  in these systems. Consistently, no superconducting peak has been resolved for Bi2212 samples with  $T_c < 40$  K in the low doping regime.

This receives further support from the recent STM data of Bi2201. Fig. 2.7(e) shows the local density of state measured by STM tunnelling experiments at several different locations on a  $T_c = 13$  K Bi2201 sample in the superconducting state. Similar to the data obtained in Bi2212, STM tunnelling spectra show strong spatial dependence. However, the superconducting peak is observable at some locations. When the spectrum is averaged over the space [Fig. 2.7(f)], the superconducting peak is emersed in the background, although a gap is still observable compared with the high temperature data. The space averaged data are very similar to that measured by ARPES, which suggest that the superconducting peak does exist in Bi2201 but is too weak to be resolved by the current ARPES technique.

## 2.6 Summary

In summary, the doping dependence of the SPR at  $(\pi, 0)$  is found to scale like the collective properties related to the superfluid, particularly the  $x$  dependence of the SPR in the underdoped regime. This unexpected manifestation of collective effects

---

<sup>4</sup>Details are discussed in Chapter 4 of this thesis

in the single-particle excitation spectra cannot be reconciled by models based on Fermi liquid, but rather may be more naturally explained by models based on the doped Mott insulator. Various experiments have shown that the superconducting peak ubiquitously exists in cuprates. Therefore a thorough understanding of its origin may be critical to understand the mechanism of high temperature superconductivity.

# Chapter 3

## Bilayer Band Splitting in Bi2212

In this chapter, we experimentally identify a new energy scale that plays an important role in the physics of Bi2212. This energy scale, the intra-bilayer coupling energy, was predicted long ago, but only discovered recently. In the first part of this chapter, we will discuss its discovery in the heavily overdoped Bi2212; in the second part of this chapter, we will show that this new energy scale dramatically changes our view of the  $(\pi, 0)$  single particle excitation spectrum, which provides vital information for various theories, as we have shown in last chapter.<sup>1</sup>

### 3.1 Electronic structure of heavily overdoped Bi2212: bilayer splitting

#### 3.1.1 Introduction

High temperature superconductors (HTSC's), as doped Mott insulators, show strong doping dependent behavior. The underdoped regime of the HTSC's is characterized by its unconventional properties, such as the pseudogap and non-Fermi liquid transport behavior. On the other hand, the overdoped regime is considered to be more "normal", partly because of the absence of a pseudogap and more Fermi liquid-like

---

<sup>1</sup>This part of results has been published in D.L.Feng, *et al.*, Phys. Rev. Lett., 86, 5550 (2001); and D.L.Feng, *et al.* *ibid.* submitted (2001).

behavior. It is very challenging and important for HTSC theories to be able to explain the phenomenology in both regimes. Angle resolved photoemission spectroscopy (ARPES), one of the most direct probes of the electronic structure, has contributed greatly to the understanding of the electronic structure of the HTSC's[102]. However, most systems studied by ARPES have either low  $T_c$ 's (below 40K for  $\text{La}_{2-x}\text{Sr}_x\text{CuO}_{4+\delta}$  (LSCO), and  $\text{Bi}_2\text{Sr}_2\text{CuO}_{6+\delta}$  (Bi2201)), or doping limitations (only up to slightly overdoping for  $\text{Bi}_2\text{Sr}_2\text{CaCu}_2\text{O}_{8+\delta}$  (Bi2212) and  $\text{YBa}_2\text{Cu}_3\text{O}_{7-y}$  (YBCO)). For a complete understanding, it is very important to study the heavily overdoped systems, especially Bi2212, which is the most studied system by ARPES.

Recent advances in high pressure annealing techniques have made it possible to synthesize heavily overdoped Bi2212. Here, we discuss ARPES measurements of the electronic structure of heavily overdoped Bi2212. We show that the long-sought bilayer band splitting exists for both normal and superconducting states of this material over a large fraction of the Brillouin zone. Bilayer band splitting is caused by the coupling between the two neighboring  $\text{CuO}_2$  planes within one unit cell of a bilayer cuprate such as Bi2212. It has been predicted by various calculations[103, 104, 105, 106, 107], but not observed in earlier ARPES data[108]. It was shown that the two originally degenerate bands (one for each  $\text{CuO}_2$  plane) split into one bonding and one antibonding band as illustrated in Fig.3.1(a). Similarly, the Fermi surface also has two pieces [Fig.3.1(b)] as calculated by the bilayer Hubbard model[107]. The detection of bilayer band splitting enables us to address several important issues. First, it provides a very detailed test for the theoretical calculations, with our experimental results favoring the bilayer Hubbard model[107] over LDA calculations[103, 105]. Second, it shows the novel result that the bilayer splitting energy in the superconducting state is only about 23% of the normal state splitting. Third, it provides an explanation for the detection of a “peak-dip-hump” structure in the normal state of heavily overdoped samples[109, 110].

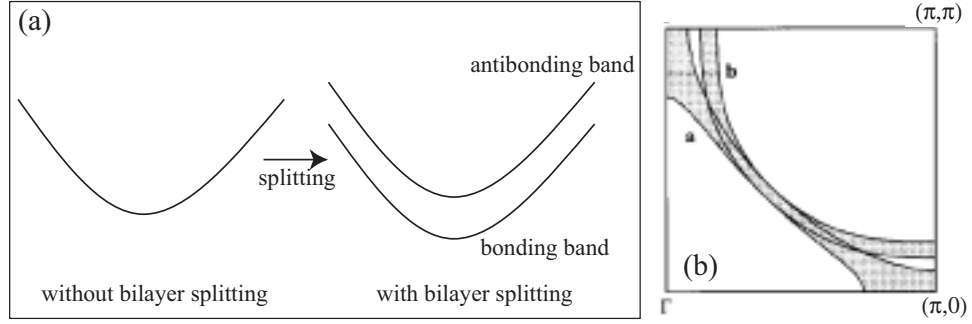


Figure 3.1: (a) Illustration of bilayer splitting of the bands (b) calculated bilayer split Fermi surfaces taken from Ref.[107] for an overdoped sample. a and b indicate antibonding and bonding Fermi surfaces respectively. The broadening is caused by the finite dispersion along the c-axis.

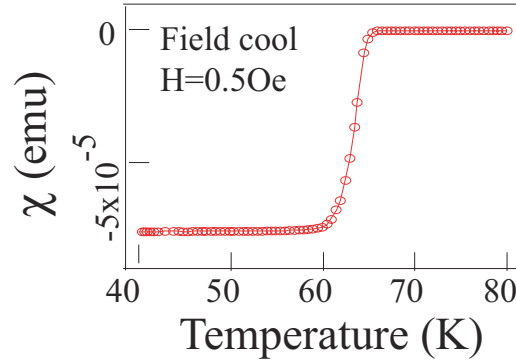


Figure 3.2: Susceptibility of heavily overdoped sample ( $T_c = 65$  K) .

### 3.1.2 Experimental

Heavily overdoped Bi2212 samples ( $T_C(\text{onset}) = 65$  K,  $\Delta T_C(10\% \sim 90\%) = 3$  K, denoted as OD65) were synthesized by annealing floating-zone-grown single crystals under oxygen pressure  $P_{O_2} = 300$  atm at  $300^\circ\text{C}$  for two weeks, and characterized by various techniques. Magnetic susceptibility measurements [Fig. 3.2] do not show the presence of a second phase. Laue diffraction and low energy electron diffraction (LEED) patterns show that its superstructure and surface resemble those of optimally doped samples, and the flatness of the cleaved sample surface is confirmed by the small laser reflection from the sample. Angle resolved photoemission experiments were performed at beamline V-4 of Stanford Synchrotron Radiation Laboratory (SSRL)



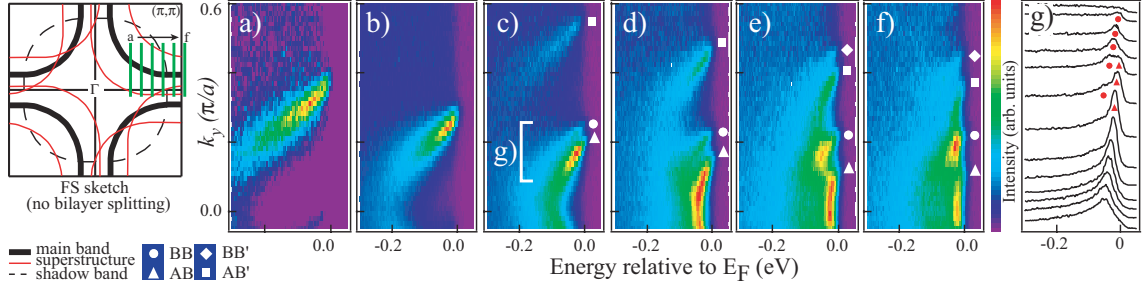


Figure 3.3: (color) (a-f) false color plot of the OD65 normal state ( $T=75K$ ) ARPES spectra taken with 22.7 eV synchrotron light. Features AB, BB, and their superstructure images AB' and BB' are indicated by triangles, circles, squares, diamonds respectively. The EDC's near the Fermi crossing in (c) (indicated by "[") are plotted in (g). The angular resolution is  $0.3^\circ$ . The panel on the left shows the Fermi surface sketch without considering the bilayer band splitting effects.

with a Scienta SES200 electron analyzer, which can take spectra in a narrow cut of  $0.5^\circ \times 14^\circ$  simultaneously in its angular mode with an angular resolution as good as  $0.12^\circ$  along the cut direction. The data were collected with polarized synchrotron light from a normal incidence monochromator, where the intensity of the second order light is extremely weak, as well as nonmonochromatic and unpolarized He-I light. The intensity of other lines are fairly weak, which contributes a smooth background to the spectra in the interested range and does not affect the conclusions drawn below. The overall energy resolution is about 10 meV. Samples were aligned by Laue diffraction, and cleaved in-situ at a pressure better than  $5 \times 10^{-11}$  torr ( $1.3 \times 10^{-10}$  torr with He lamp turned on). Sample aging effects are negligible during the measurement.

### 3.1.3 Results

A typical Fermi surface (FS) sketch of the Bi2212 system without considering the bilayer band splitting is shown in Fig. 3.3[108]. One can see the main FS, its superstructure images due to structure modulations in the BiO layer, which are typically about  $(0.21, 0.21)$  away from the main FS<sup>2</sup>, and the shadow band FS, which is a

<sup>2</sup>The effect of the superstructure on the electronic structure can be viewed, in a simple sense, as the photoelectron diffraction effect. The photoelectron from the  $CuO$  plane is diffracted by the structure modulations in the BiO plane, which act as an grating. The relation between the

( $\pi, 0$ ) foldback of the main FS [111], and is very weak at 22 eV photon energy due to matrix element effects[108]. Photoemission intensity taken in the normal state of OD65 along the momentum cuts indicated by the green lines in the FS sketch are shown in Fig. 3.3(a-f) as a function of momentum and binding energy. In this way, one can clearly see the centroids of the dispersing features. For example, Fig. 3.3(a) shows that one band disperses and crosses the Fermi energy along a momentum cut that goes through the d-wave node region. Away from the nodal region, this seemingly single feature splits evidently into two features, Features AB and BB, starting from Fig. 3.3(c). The photoemission intensities in the bracketed region are replotted in the form of energy distribution curves (EDC's) in Fig. 3.3(g), where one can see two peaks cross the Fermi level about  $0.9^\circ$  apart. This splitting increases when approaching the ( $\pi, 0$ ) region. In Fig. 3.3(f), the Features AB and BB are well-separated, and two more weaker features (AB' and BB') are clearly visible as well; these are the superstructure images of Features AB and BB. The absence of splitting in the nodal region is checked with the best achievable angular resolution ( $\sim 0.12^\circ$ ).

The observed Fermi crossings in Fig. 3.3(c-f) deviate from what is expected from the FS sketch shown in Fig. 3.3, but can be naturally interpreted by the presence of bilayer band splitting. Because the Bi2212 ARPES features are considered to be mainly contributed by the anti-bonding  $x^2 - y^2$  state in the  $\text{CuO}_2$  plane, and Bi2212 has two  $\text{CuO}_2$  planes per unit cell, the intrabilayer coupling would cause a splitting. As we will see later, the observed splitting agrees with what is expected from a bilayer system[107]. This interpretation is also supported by recent studies of heavily overdoped single-layer Bi2201, where only one band was observed[112]. Since Feature AB is always at lower binding energy than Feature BB at a given momentum, we assign the anti-bonding band (AB) to Feature AB, and bonding band (BB) to Feature BB.

The Fermi surfaces can be determined by determining Fermi crossings of the bands (dispersion method), or determining the local maxima of the low energy ARPES

---

superstructure and the superconductivity is not clear. For example, the superstructure usually is stronger in Bi2201 than in Bi2212, but the enhancement is not observed after doping the system with Pb in the BiO layer to remove the superstructure.

spectral weight distribution (spectral weight method) [Fig. 3.4]<sup>3</sup>. One can see two main FS's, one for the antibonding band (AB) and the other for the bonding band (BB), and their corresponding superstructure images (AB' and BB'). The observed hole-like Fermi surface topology is consistent with early findings in less overdoped Bi2212 systems at similar photon energies. These FS's overlap in the nodal region and gradually depart from each other when approaching the  $(\pi, 0)$  region, which is almost the same as what is predicted by the bilayer Hubbard model as shown in Fig. 3.1(b). Fig. 3.4(b) shows EDC's along one cut that crosses all of the four Fermi

<sup>3</sup>We note that at 20 eV photon energy, the FS's determined by the dispersion method do not agree with those determined by the spectral weight method. The latter is affected by the photoemission matrix elements: when two features are very close and have similar intensities, the positions of the local spectral weight maxima shift due to the overlapping. However, combination of both methods can give a qualitative and objective measurement of the FS.

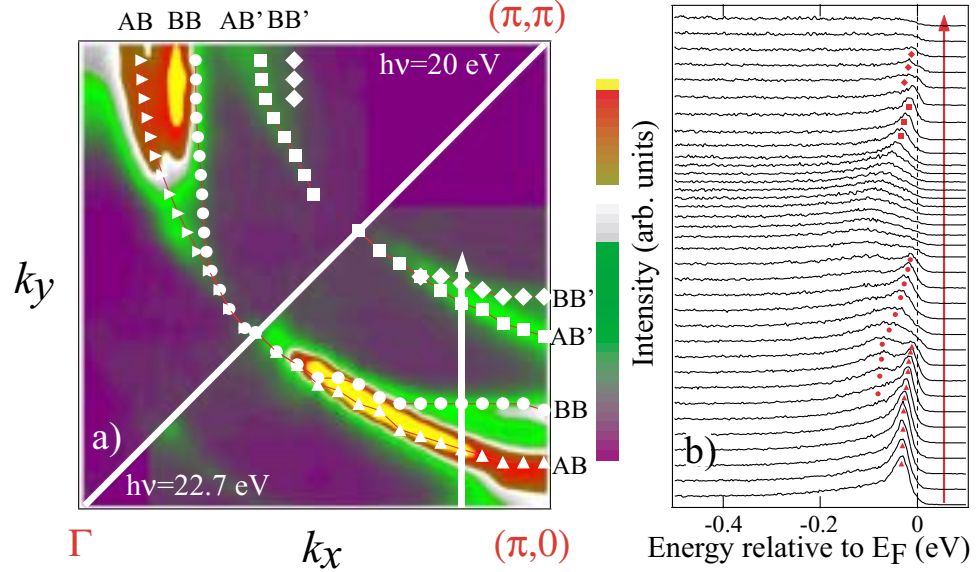


Figure 3.4: (color) (a) False color plot of the spectral weight mapping near  $E_F$  ([-20 meV, 10 meV]) of OD65 taken at 22.7 eV (lower right half,  $T=75K$ ) and 20 eV (upper left half,  $T=80K$ ) (note they are from different experiments). The Fermi surface determined by dispersion is also plotted for antibonding states (AB, triangles), bonding states (BB, circles), superstructure images of antibonding states (AB', squares), and bonding states (BB', diamonds). (b) ARPES spectra along the cut indicated by the arrow in (a).

surfaces. At 22.7 eV photon energy [lower right half of Fig. 3.4(a)], the AB has more weight near  $E_F$  than the BB, and this situation is reversed at 20 eV [upper left half of Fig. 3.4(a)]. This strong photon energy dependence of the relative intensities of the AB and BB is consistent with the bilayer band splitting, because the AB and BB have odd and even symmetries respectively along the c-axis. By tuning the incident photon energy, the wavevector of the final electron state along the c-axis is changed, which changes the photoemission cross-sections between the final state and the initial BB and AB differently due to their opposite symmetries. The fact that we see bilayer band splitting all over the FS and in the superstructure images (AB' and BB') away from the  $(0, 0)$  region rules out the possibility that the split FS's are artifacts caused by the superstructure. Moreover, because the intensity of BB is weaker than that of AB in the 22.7 eV photon energy data, AB cannot be a superstructure of BB, and vice versa for the data taken at 20 eV photon energy.

To understand the effect of the bilayer band splitting on the superconducting state, spectra were taken in both the normal and superconducting states near the  $(0, 0)$  region (Fig. 3.5), where the splitting is greatest. It was found that in this region, the ARPES lineshape of Bi2212 evolves dramatically across  $T_c$  from a broad spectrum in the normal state into a well-known peak-dip-hump (PDH) structure in the superconducting state[61].

In the normal state [Fig. 3.5(a)], the antibonding state crosses  $E_F$  near  $n4$  and  $n-4$ , while the bonding state disperses through the Fermi energy around spectra  $n8$  and  $n-8$ . The presence of two features in the normal state was reported earlier [109, 110], and suggested to be an anomalous normal state counterpart to the conventional superconducting PDH[109]. Here, we show that this feature is actually due to the bilayer splitting. In spectra  $n-3$  through  $n3$ , the BB is at high binding energy and thus broad, while the AB is at low binding energy and thus sharp, which conspire to give a PDH-like structure. We stress that this is different from the PDH structure that turns on at  $T_c$ .

In the superconducting state [Fig. 3.5(b)], the low energy part of the spectra evolves into two sharp superconducting peaks. It appears that both the normal state BB and AB develop their own superconducting PDH structure. BB hump

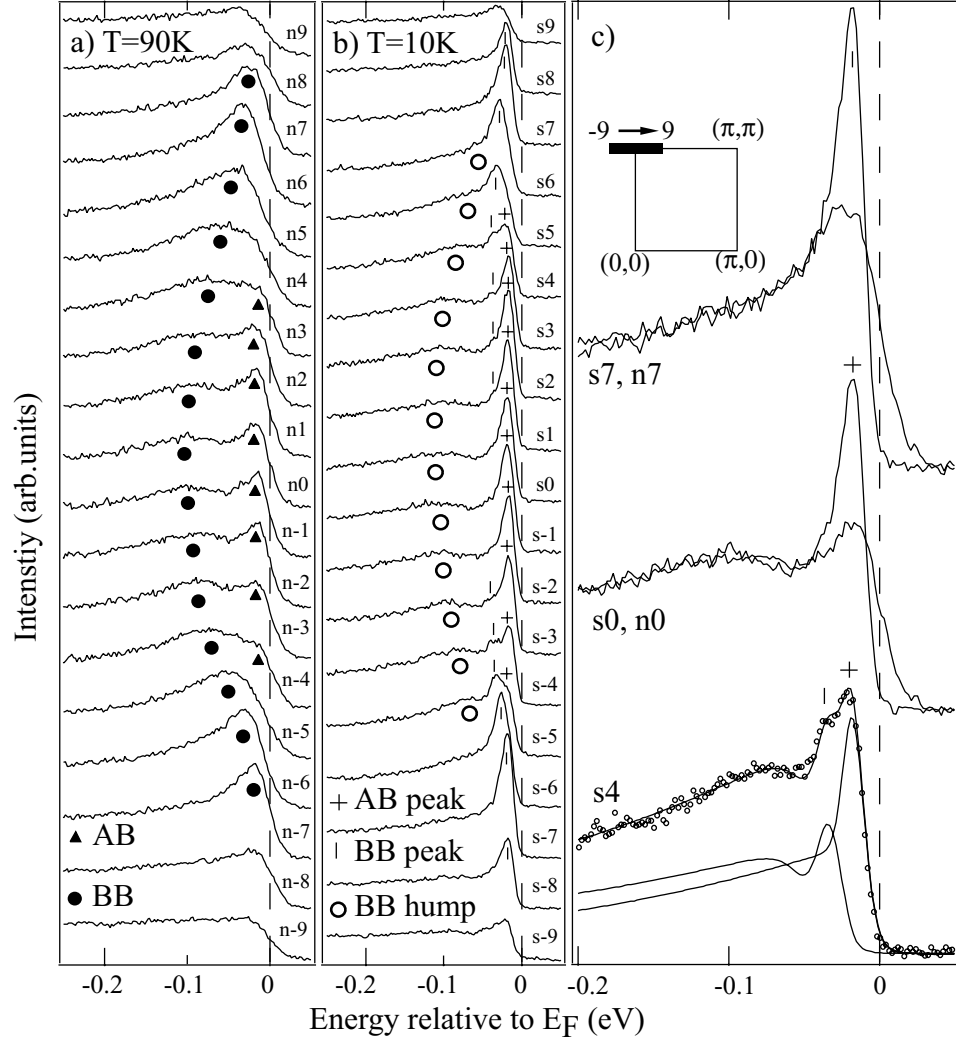


Figure 3.5: ARPES spectra taken on OD65 with He-I light for (a) normal state, and (b) superconducting state. The angular resolution is  $0.56^\circ$ . (c) shows selected spectra from (a) and (b). Note that the fit of s4 is not unique. The spectra are taken along  $(-0.24, 0) - (0.24, 0)$ , and labeled from -9 to 9 as shown in the inset of (c).

is observed near the normal state BB binding energy, whereas AB hump is buried under the superconducting peaks, which presumably locates also near the normal state AB binding energy. Similar to the superconducting peak reported before in less overdoped samples, both BB and AB superconducting peaks lose their intensity upon crossing the corresponding normal state BB/AB FS's. More specifically, spectra s7

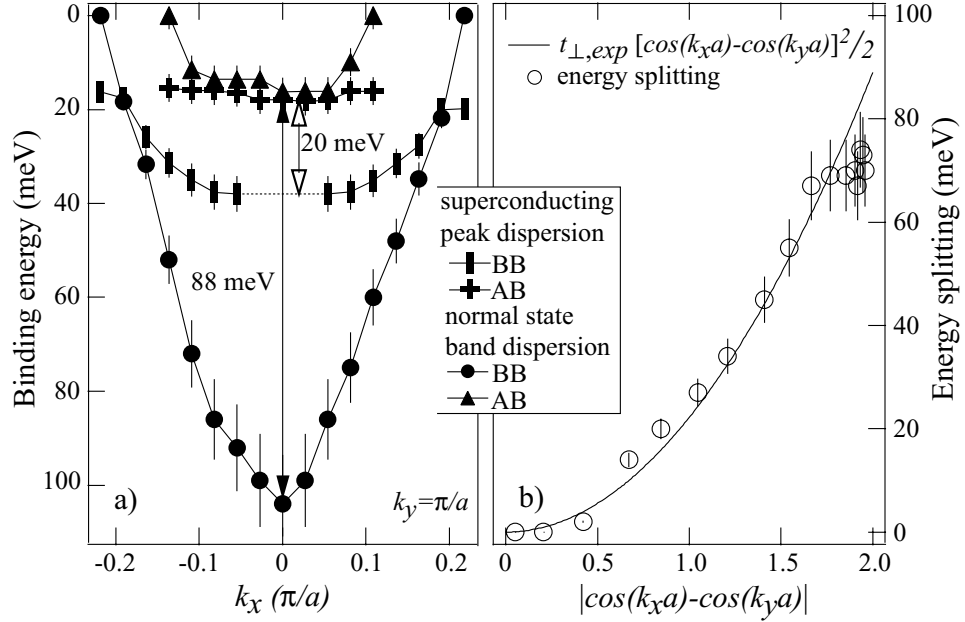


Figure 3.6: (a) Dispersion extracted from Fig. 3.5. (b) Energy splitting along the AB Fermi surface, which are obtained from data shown in Fig. 3.3. It is simply the binding energy of the BB, since the binding energy of AB is zero at its Fermi surface. The curve is  $t_{\perp,exp} [\cos(k_x a) - \cos(k_y a)]^2 / 2$ , where  $t_{\perp,exp} = 44 \pm 5$  meV. Error bars are due to the uncertainties in determining the energy position.

and n7 [replotted in Fig. 3.5(c)], which consist mainly of the BB, strongly resemble the normal and superconducting state spectra from overdoped samples with less carrier doping[34, 113]. When the BB superconducting peak disperses to higher binding energies, it becomes weaker and presumably contributes very little to the sharp peak seen at s0. Therefore, the observed sharp peak at s0 can be regarded as mainly due to the antibonding state. For spectra containing two peaks, they can be fitted by two PDH's, as shown in Fig. 3.5(c) for s4.

The dispersions extracted from Fig. 3.5 are summarized in Fig. 3.6(a). Because the superconducting peak intensity of the BB is very weak near  $(\pi, 0)$ , its position is extrapolated and shown as the dotted line. Although the BB and AB superconducting peaks have different dispersions, their minimum binding energies near their respective FS's are almost the same ( $\sim 16$  meV), which shows that the BB and AB

have the same  $d$ -wave superconducting gap amplitude. The maximum energy splittings can be extracted from the binding energies at  $(\pi, 0)$ . They are found to be about 88 meV for the normal state bands, and interestingly, only about 20 meV for the superconducting peaks. The striking difference in the splitting energies cannot be explained conventional theories, where quasiparticles below  $T_c$  have an energy of  $E_{\mathbf{k}} = \sqrt{\Delta_{\mathbf{k}}^2 + \epsilon_{\mathbf{k}}^2}$ , with  $\epsilon_{\mathbf{k}}$  and  $\Delta_{\mathbf{k}}$  being the normal state quasiparticle energy and superconducting gap, respectively. The small splitting energy of the superconducting peak also counters the naive expectation that global phase coherence below  $T_c$  will enhance the  $c$ -axis coupling and thus cause larger splitting. Instead, the data suggest that the superconducting peak is a new quasiparticle generated upon the superconducting phase transition. This is in agreement with the earlier observation that the weight of the superconducting peak is closely related to the carrier doping level and the condensation fraction of the system[34, 113]. We hope the new data can stimulate more theoretical works on this issue.

### 3.1.4 Discussion

The nature of the normal state bilayer band splitting as a function of momentum and energy puts strong constraints on theoretical models. A maximum momentum splitting near  $(\pi, 0)$  contradicts early LDA calculations, where the calculated BiO Fermi surface near  $(\pi, 0)$  causes very a small splitting of the  $\text{CuO}_2$  bands near  $(\pi, 0)$ [103]. However, it does agree qualitatively with bilayer LDA calculations that only consider bands from the two  $\text{CuO}_2$  planes[105], and the bilayer Hubbard model, which is based on the bilayer LDA band calculations plus additional on-site Coulomb repulsion[107]. The bilayer Hubbard model predicts two AB/BB Fermi surfaces similar to the data for similar carrier doping levels[107].

The bilayer LDA calculations [105] predicted that the normal state bilayer energy splitting to be  $2t_{\perp}(\mathbf{k}) = t_{\perp}(\cos(k_x a) - \cos(k_y a))^2/2$ , where  $t_{\perp}(\mathbf{k})$  is the anisotropic intrabilayer hopping. It indicates that the maximum energy splitting is  $2t_{\perp}$  at  $(\pi, 0)$ . This agrees with the data, and one obtains the experimental intrabilayer

hopping  $t_{\perp,exp} = 44 \pm 5$  meV. To test this over a large momentum range, the normal state energy splitting along the AB Fermi surface [Fig. 3.6(b)] were extracted from the data in Fig.'s 3.3 and 3.4. Indeed, the data can be fitted very well by  $t_{\perp,exp}(\cos(k_x a) - \cos(k_y a))^2/2$ , but quantitatively, the experimental maximum energy splitting of 88 meV ( $2t_{\perp,exp}$ ), is much smaller than the 300 meV ( $2t_{\perp,LDA}$ ) splitting predicted by the bilayer LDA calculations[105]. On the other hand, the data agree better with the bilayer Hubbard model[107], which predicted a similar anisotropic energy splitting with 40 meV maximum energy splitting at  $(\pi, 0)$  for the similar doping level. This is because unlike the bilayer LDA calculations, the bilayer Hubbard model considers strong correlations, and strong on-site Coulomb repulsion (or correlations) will substantially reduce the hopping to an occupied site thus reducing the effective intrabilayer hopping[106]. Based on this, its small splitting energy scale (40 meV) may suggest that weaker on-site Coulomb repulsion should be adopted in the bilayer Hubbard model (at least for the heavily overdoped case). We note that  $t_{\perp,exp}$  is of similar magnitude of the gap, and is a significant fraction of the in-plane exchange coupling  $J$ , and the bandwidth. Therefore, the intrabilayer coupling should be considered in models describing Bi2212.

A natural question is why the bilayer band splitting is particularly prominent in heavily overdoped materials, and not observed in previous studies on samples with less doping. This is mainly because the more Fermi liquid-like behavior in the heavily overdoped regime results in much better defined quasiparticles, i.e., much sharper features. The absence of two well-defined features in the spectra of less overdoped samples does not necessarily imply the absence of the bilayer band splitting. In fact, with improved resolution, preliminary studies have found signatures of bilayer band splitting in the normal state of slightly overdoped Bi2212 samples[119, 120]. As for the optimally doped and underdoped systems, situation is more complicated, which is the main subject of the following section.



## 3.2 Nature of electronic excitation in Bi2212 near $(\pi, 0)$ : bilayer splitting effects

### 3.2.1 Introduction

ARPES data from the  $(\pi, 0)$  region of  $\text{Bi}_2\text{Sr}_2\text{CaCu}_2\text{O}_{8+\delta}$  (Bi2212) have been one of the most important sources of information about the electronic structure of the high temperature superconductors [102]. The normal state spectra are very broad, with widths much larger than those from the nodal region (near  $(\pi/2, \pi/2)$ ), indicating a large anisotropy in the scattering rate along the Fermi surface[67, 114]. This anisotropy has been considered in various theories that describe the anomalous transport and optical properties in the cuprates[115]. In addition, the information gathered from these spectra have helped to put additional important parameters into microscopic models[116]. On the other hand, the superconducting state spectra contain the well known peak-dip-hump structure[61]. The position of the dip was suggested to be related to the neutron  $(\pi, \pi)$  resonance mode[66], resulting in modelling of the tunnelling and ARPES data [117]. The peak intensity in the peak-dip-hump structure has been interpreted as being related to the condensate fraction (chap. 2) [34, 113], as discussed by various theories[85, 90, 91]. These studies constitute a significant part of the HTSC literature.

Bi2212 has two coupled  $\text{CuO}_2$  planes in the unit cell and therefore bilayer splitting is naturally expected. However, it has been largely ignored in the studies mentioned above, partly because of earlier reports of its absence in the ARPES spectra of optimally doped and underdoped samples[108, 118]. However, as we have discussed in the last section, the bilayer splitting does exist in overdoped Bi2212, and the bilayer splitting energy scale is comparable to the size of the superconducting gap and the normal state band dispersion. As a result, the bilayer splitting causes a peak-dip-hump structure even in the normal state of heavily overdoped Bi2212[35, 109, 121], demonstrating that the intra-bilayer coupling plays an important role in the electronic structure of the overdoped regime and should be seriously considered in relevant theories. These results naturally raise the question of whether bilayer splitting exists in

the optimal and under-doped regimes where most experiments and analyses were conducted, and if it does, how it affects our understanding of the nature of the electronic excitations near  $(\pi, 0)$ .

In the following, we will show ARPES spectra from Bi2212 and Bi2201 for various dopings and photon energies ( $\hbar\omega$ ). The lineshapes of Bi2201 and Bi2212 are similar in the nodal region, but very different near  $(\pi, 0)$ . In addition, Bi2212 spectra from the  $(\pi, 0)$  region are strongly modified by  $\hbar\omega$ , in contrast to the weak photon energy dependence of the Bi2201 spectra. We show that these results can be well explained by the underlying bilayer splitting effects in under and optimally doped Bi2212 and that the broad linewidth near  $(\pi, 0)$  is, in large part, due to the bilayer splitting. These results are very different from the current, commonly-accepted picture of the electronic excitations near  $(\pi, 0)$ , and therefore requires the reexamination of many existing theories, and puts strong constraints on future theoretical models and data analysis.

### 3.2.2 Experimental

High quality Bi2212 and Bi2201 single crystals were grown by the floating zone technique. Bi2212 samples are labeled by the superconducting phase transition temperature  $T_c$  of the sample with the prefix UD for underdoped, OP for optimally doped, and OD for overdoped. Bi2201 samples are labeled in the same way but in lowercase. For example, UD83 represents a  $T_c=83$  K underdoped Bi2212 sample, while od17 represents a  $T_c=17$  K overdoped Bi2201 sample. Samples with Pb doping are labeled with the prefix “Pb”, except od33, which is doped with both Pb and La. The superconducting transition widths,  $\Delta T_c$ , were less than 3K for all the samples used. Angle resolved photoemission experiments were performed at a normal incidence monochromator (NIM) beamline of the Stanford Synchrotron Radiation Laboratory, where the intensity of the second order light is extremely weak. Data were taken with a Scienta SES200 electron analyzer with the angular resolution of  $0.3 \times 0.5$  degrees unless specified otherwise. The overall energy resolution varied from 10 meV to 18 meV at different  $\hbar\omega$ 's. This variation of the energy resolution does not affect any of our

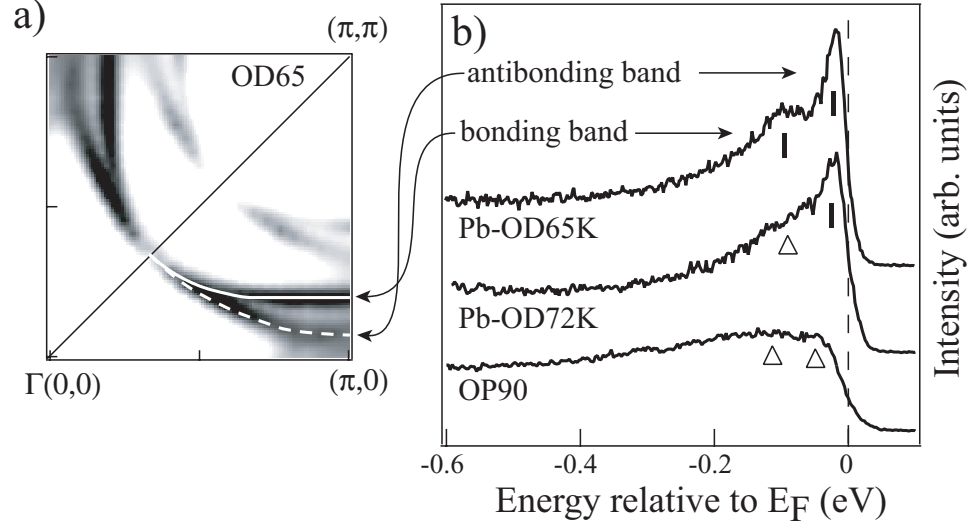


Figure 3.7: (a) Bilayer-split Fermi surfaces of heavily overdoped OD65; the two weaker features are their superstructure counter parts. Solid and dashed lines represent the bonding and antibonding Fermi surfaces, respectively. (b) Normal state photoemission spectra of Bi2212 taken at  $(\pi, 0)$  for three different doping levels. Data were taken with  $h\nu = 22.7\text{eV}$  photon. Bars indicate identified feature positions, and triangles indicate possible feature positions.

conclusions since the energy scales of the discussed features are much larger. The chamber pressure was better than  $5 \times 10^{-11}\text{torr}$ , and sample aging effects were negligible during the measurements. Unless otherwise specified, normal state data were taken 10~20K above  $T_c$ .

### 3.2.3 Lineshape of $(\pi, 0)$ spectrum: doping and system dependence

The most obvious signature of the bilayer splitting is double features in the Fermi surface and energy distribution curves (EDC), as shown in Fig. 3.7 for heavily overdoped Bi2212 [35]. Due to the anisotropic nature of the intrabilayer coupling, the amplitude of the bilayer splitting is also anisotropic with zero splitting in the nodal region and maximum splitting at  $(\pi, 0)$  [Fig. 3.7(a)]. The normal state  $(\pi, 0)$  EDC

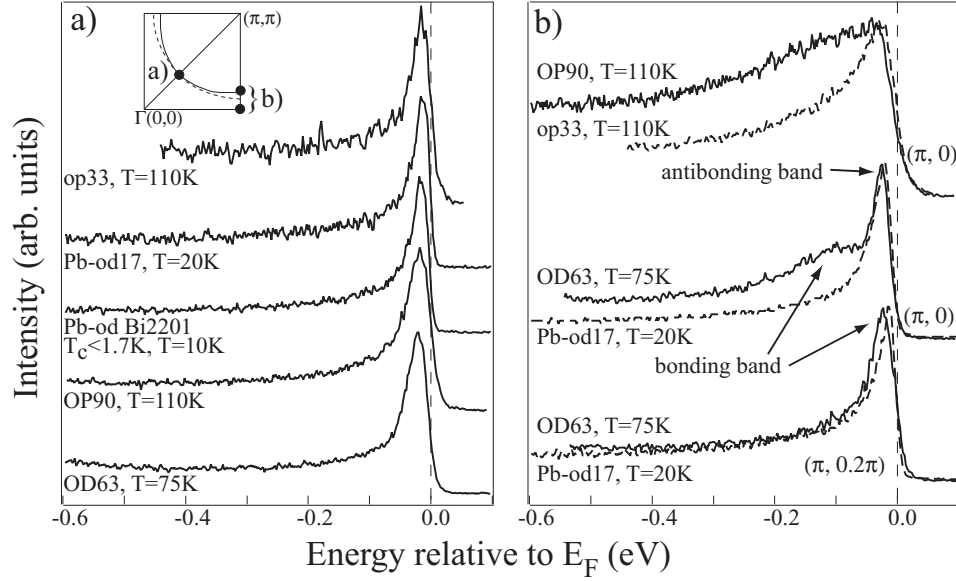


Figure 3.8: Normal state spectra taken at (a) the d-wave node region, and (b) the  $(\pi, 0)$  region for both Bi2212 and Bi2201 at various dopings. The solid and dashed lines in the inset of panel (a) indicate the bonding and antibonding Fermi surfaces of OD63 respectively, and the black dots indicate the momentum locations of the spectra. Data were taken with  $\hbar\omega = 22.7\text{eV}$ . Angular resolution was  $0.3^\circ$  for OP90 and  $0.12^\circ$  for others in panel a).

of heavily overdoped Pb-OD65 [Fig. 3.7(b)] clearly shows two features that exhibit a normal state peak-dip-hump structure, and are assigned to the two bilayer split bands[35, 119, 120]. This was not observed in previous measurements on overdoped samples, mainly due to extrinsic factors such as energy and angular resolution. With a slight decrease of the doping (Pb-OD72), the two components of the  $(\pi, 0)$  spectrum are barely distinguishable. Compared with Pb-OD65, the two features become broader and their intensities smaller. For OP90, the spectrum is intrinsically too broad to distinguish the two split features, which makes the identification of the bilayer splitting very difficult in this manner.

To clarify this further, we looked for other signs of bilayer splitting by comparing the spectra of Bi2212 with those of single layer Bi2201 at similar doping levels. We

chose two pairs of samples: OP90 and op33, and OD63 and od17. Based on the empirical  $T_c$  vs. doping formula[122], they have doping levels of 0.16, 0.16, 0.22, and 0.24, respectively. For the spectra taken in the nodal region shown in Fig. 3.8(a), Bi2201 and Bi2212 have similar lineshapes, and the linewidth varies only slightly for different systems and experimental conditions. This holds true even for the heavily overdoped Bi2201 sample with a  $T_c < 1.7\text{K}$  (doping level  $\sim 0.28$ ). The situation is very different for the spectra taken in the  $(\pi, 0)$  region [Fig. 3.8(b)]. For OD63, the spectrum consists of both the bonding and antibonding bands, while the spectrum at  $(\pi, 0.2)$  mostly consists of the bonding band, because the antibonding band is above  $E_F$  [35]. We find that the Bi2212 and Bi2201 spectra match at  $(\pi, 0.2)$  almost perfectly, while those at  $(\pi, 0)$  do not because of the presence of the bonding band at higher energies. As far as the near- $E_F$  features are concerned, the spectra from both od17 and OD63 have very similar linewidths at similar binding energies and momenta. This similarity between the OD63/od17 low energy spectra can be attributed to their similar doping levels in each  $\text{CuO}_2$  plane. The OP90/op33  $(\pi, 0)$  spectra show a large mismatch similar to the OD63/od17 case, which can be naturally attributed to the additional spectral weight from the bonding band of OP90. On the other hand, without bilayer splitting (or intra-bilayer coupling) in OP90, properties of the  $\text{CuO}_2$  planes of OP90 and op33 should be similar. It is then difficult to explain why the linewidths of OP90 and op33 are so dramatically different in the  $(\pi, 0)$  region, considering that Bi2201 and Bi2212 are very similar in many other aspects such as the phase diagram, Fermi surface shapes, dispersion energy scales[123, 124], and particularly, residual resistivity, which indicates the scattering caused by defects and impurities. The larger linewidth of op33, compared to od17, may be attributed to enhanced correlation effects with decreased doping, presumably  $(\pi, \pi)$  scattering due to increased antiferromagnetic fluctuations[67, 115]. We note that these normal state spectra were taken at different temperatures. However, the thermal broadening is negligible compared to the peak widths, within the experimental temperature range.

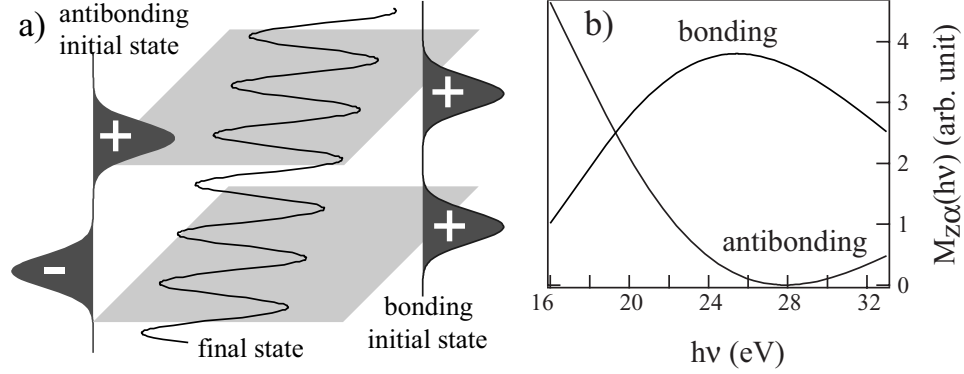


Figure 3.9: (a) Cartoon of the initial and final state symmetries along the c-axis for the photoemission process with the presence of the bilayer splitting. (b) The calculated c-axis contributions to the photoemission matrix elements for both bonding and antibonding state as functions of  $h\nu$ , as described in the text.

### 3.2.4 Lineshape of $(\pi, 0)$ spectrum: photon energy dependence

The above comparison between spectra from Bi2201 and Bi2212 suggests the possible presence of bilayer splitting in optimally doped samples. This is further supported by photon energy dependence studies. As depicted in Fig. 3.9(a), the antibonding and bonding states have opposite symmetry along the c-axis with respect to the midpoint between the two CuO<sub>2</sub> planes. As a consequence, their photoemission matrix elements respond differently to various experimental parameters, including the photon energy. Upon tuning  $h\nu$ , the spectral weight from the bonding and antibonding states will vary differently, thus changing the overall spectral lineshapes. This can be further illustrated by an analysis of the photoemission matrix elements. Although comprehensive calculations of the photoemission matrix element are still not feasible because of the complexity in the crystal structure and the photoemission process, as well as the electron-electron correlations, with reasonable assumptions and simplifications one can still study its behavior on a qualitative level, which turns out to be very helpful for the interpretation of the data on various occasions[125].

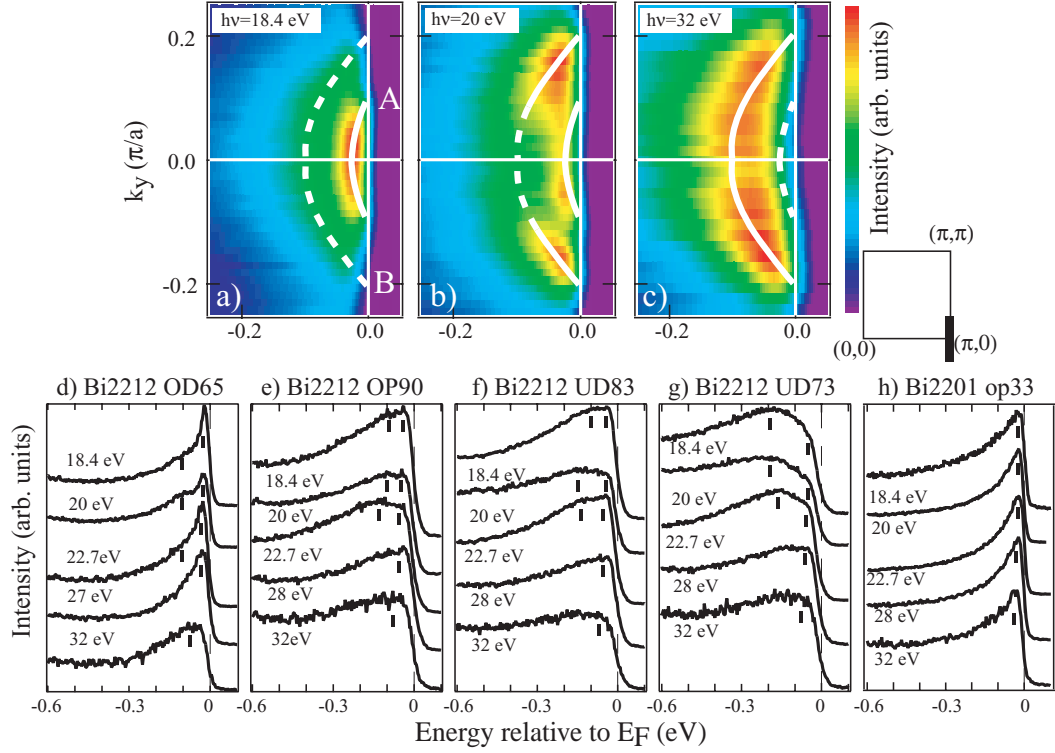


Figure 3.10: (a-c) Normal state photoemission intensity as a function of momentum and binding energy in color scale maps near the  $(0,0)$  region ( $k_x = 0$ ) of OD65 taken with  $h\nu = 18.4$  eV, 20 eV and 32 eV respectively. The thick white lines indicate the dispersion of the bonding (B) and antibonding (A) bands, and lines are shown in dashed form when the feature is weak. (d-h) Normal state EDC's taken at  $(0,0)$  for samples (d) OD65, (e) OP90, (f) UD83, (g) UD73, and (h) op33. at various  $h\nu$ 's. Bars serve as guides for the centroids of spectral features. Note that the features indicated by bars near  $E_F$  may be Fermi cutoffs instead of real features. The separation between bars is not necessarily the splitting energy.

We consider two 2D systems coupled via a certain bilayer interaction. The photoemission intensity for such a system with non-interacting electrons is  $I \propto \sum_{\alpha=a,b} M_{\alpha}^2 A_{\alpha}(k, \epsilon)$  where  $k$ ,  $\epsilon$  and  $A_{\alpha}$  are the momentum, energy for the final state, and the spectral function respectively, while  $a$  and  $b$  represent antibonding and bonding bands. In the one-electron matrix element  $M_{\alpha} = \langle f | \mathbf{A} \cdot \mathbf{p} | i_{\alpha} \rangle$ ,  $f$  and  $i_{\alpha}$  are

the final state and initial state single electron wave functions,  $\mathbf{A}$  is the vector potential of the photon field, and  $\mathbf{p} \equiv -i\hbar\nabla$ . Assuming  $\psi_{i\alpha}(\mathbf{x}, \mathbf{y}, z) = \psi_i(\mathbf{x}, \mathbf{y}) \phi_{\alpha}(z)$  and a free electron final state  $\psi_f(\mathbf{x}, \mathbf{y}, z) = e^{ik_x x + ik_y y + ik_z z}$ , the matrix element can be separated into the in-plane contribution  $M_{\parallel}$  and the out-of-plane contribution  $M_{z\alpha}$ . Under the dipole approximation,

$$\begin{aligned} M_{\alpha} &\propto M_{\parallel} + M_{z\alpha} \\ &\equiv A_{\parallel}/A_z \langle e^{ik_x x + ik_y y} | r_{\parallel} | \psi_i(\mathbf{x}, \mathbf{y}) \rangle + \langle e^{ik_z z} | z | \phi_{\alpha}(z) \rangle \end{aligned}$$

where  $k_x$  and  $k_y$  are fixed to be  $(\pi, 0)$  for both the initial and final states. The first term contributes equally to both bonding and antibonding states, and the ratio of polarization,  $A_{\parallel}/A_z$ , is approximately constant in the experiment. Therefore, we can focus on  $M_{z\alpha}$  as a function of  $\hbar\omega$ . To further simplify, we assume

$$\phi_{\alpha}(z) = e^{-\frac{(x-l_0/2)^2}{(\beta l_0)^2}} \pm e^{-\frac{(x+l_0/2)^2}{(\beta l_0)^2}},$$

where “-” and “+” signs are for  $\alpha = a$  and  $b$  respectively.  $l_0$  is the intrabilayer distance, and  $\beta$  is an adjustable parameter reflecting how the electron wavefunction is localized within a  $\text{CuO}_2$  layer and is assumed to be  $\beta = 1/6$  in the calculation. For the final state, the free electron approximation gives  $k_z = [2m^*\hbar^{-2}(\hbar\omega - \Phi + v_0) - (k_x^2 + k_y^2)]^{-\frac{1}{2}}$ , where we choose the photoelectron effective mass  $m^*$  to be the free electron mass, the work function  $\Phi = 4.3 \text{ eV}$ , and inner potential  $v_0 = 7 \text{ eV}$  in the calculation<sup>4</sup>.  $M_{z\alpha}$  calculated with these parameters and simplifications is shown for both antibonding and bonding states in Fig. 3.9(b). The  $M_{z\alpha}$ ’s for the bonding and antibonding state have almost opposite behaviors with  $\hbar\omega$ , and changes quite dramatically in the studied  $\hbar\omega$  range. This causes the overall lineshape of the Bi2212  $(\pi, 0)$  spectrum to alter significantly with  $\hbar\omega$  as the relative weight of bonding/antibonding states oscillates. In the case of optimally doped and underdoped systems, the centroid of the broad feature will shift.

This is indeed observed in OD65, where the bilayer splitting has been clearly

---

<sup>4</sup>We note that the qualitative results discussed here are independent of the chosen parameters, and only the qualitative results shall be compared with the data.



identified[35]. Fig. 3.10(a-c) show ARPES intensity taken in the  $(\pi, 0)$  region at different  $\hbar\omega$ 's as a function of momentum and binding energy. Because the NIM gives extremely weak second-order light, it is possible to directly compare spectra taken at different  $\hbar\omega$ 's. One can see that the relative intensities of the antibonding band (A) and bonding band (B) change with  $\hbar\omega$ . At some photon energies, only one feature is prominent, while in others, both features are clearly visible. EDC's of OD65 at  $(\pi, 0)$  are plotted in Fig. 3.10(d)<sup>5</sup>. While some  $k_z$  dispersion may exist, the data show strong bilayer matrix element effects. One clearly sees that the relative intensities of the bonding and antibonding features vary drastically with  $\hbar\omega$ . For optimally doped [Fig. 3.10(e)] and underdoped Bi2212 [Fig. 3.10(f-g)], one does not see two clearly separated features. However, one can see the strong variation of the lineshape, and changes in the centroid of the feature. Although there are some detailed variations from sample to sample, the spectra of underdoped and optimally doped Bi2212 change with a similar trend as the OD65. On the other hand, for the optimally doped single layer system Bi2201 [Fig. 3.10(h)], the peak position and the overall lineshape show virtually no photon energy dependence. The high binding energy background of op33 is a smooth function of binding energy and photon energy. These indicate that the strong photon energy dependence of the Bi2212 spectra is due to the bilayer splitting.

### 3.2.5 Quantitative estimation of the bilayer splitting in optimally doped Bi2212

We have shown that from both photon energy dependence and the EDC line shape comparison between Bi2212 and Bi2201, bilayer splitting exists in optimally doped and underdoped Bi2212, and it can naturally explain the large normal state linewidth of Bi2212 at  $(\pi, 0)$ . From a theoretical point of view, the presence of bilayer splitting is a model-independent universal behavior that is independent of doping. A more important question is how the bilayer splitting amplitude evolves with doping. As we will illustrate later, this contains direct information about the correlation effects

---

<sup>5</sup>Data in Fig. 3.10 (d-h) were taken in the momentum window of  $0.01 \sim 0.02\pi \times (0.02 \sim 0.03\pi)$  centered around  $(\pi, 0)$ . Due to the weak dispersion of the electronic states near  $(\pi, 0)$  in Bi2212 and Bi2201, small variations in the momentum window do not affect the spectral lineshape.

[106].

Since it is not feasible to separate a broad EDC into bonding and antibonding components reliably, it is difficult to quantitatively determine the bilayer band binding energy splitting directly from the spectra for the optimal doped and underdoped systems. Thus we turn the momentum distribution curve (MDC) approach. The MDC analysis has several advantages over EDC analysis. First, MDC analysis is almost independent of the background; second, MDC has a simple Lorentzian form if the self-energy is a weak function of the momentum; third, the MDC width gives the direct measurement of the scattering rate when multiplied by the bare band Fermi velocity [114, 130].

We measured the normal state MDC width along the Fermi surface similar to the work by Valla *et al.*[114] for both OP90 and op33. Two examples are shown in Fig. 3.11. ARPES spectra taken along momentum cuts #1 and #2 shown in Fig. 3.11(a). After the spectra were normalized by the detector angular profile obtained with polycrystalline gold, MDC's at the Fermi energy of each cut were obtained and fitted to single or multiple Lorentzians:

$$A(k, E_F) = a_0 + \frac{a_1}{(k_{\parallel} - a_2)^2 + a_3}$$

,  $k_{\parallel}$  is the momentum along each cut.  $a_i$ 's ( $i = 0, 1, 2, 3$ ) are the fitting parameters.  $2\sqrt{a_3}$  is the full-width-half-maximum (FWHM) of the Lorentzian, which is defined as the MDC width. Fig. 3.11(b) shows MDC's at  $E_F$  along the  $(0,0) - (\pi, 0)$  cut for OP90 and op33. One can see that the op33 MDC is slightly narrower than the OP90 MDC. Fig. 3.11(c-d) show MDC's at  $E_F$  along the cut #2 for OP90 and op33 respectively. Because cut #2 goes through regions that cross many superstructure Fermi surfaces, the MDC's are more complicated than that of cut #1, especially in the  $k_y < 0$  side. Because op33 has stronger superstructure modulations than OP90, its MDC fit requires four Lorentzians, which correspond to two main bands and two superstructure bands as illustrated in Fig. 3.11(a). OP90 fit, on the other hand only requires three Lorentzians, indicating intensity of one of the superstructure band is negligible. Fortunately, we can just focus on the  $k_y > 0$  side of the spectra, which

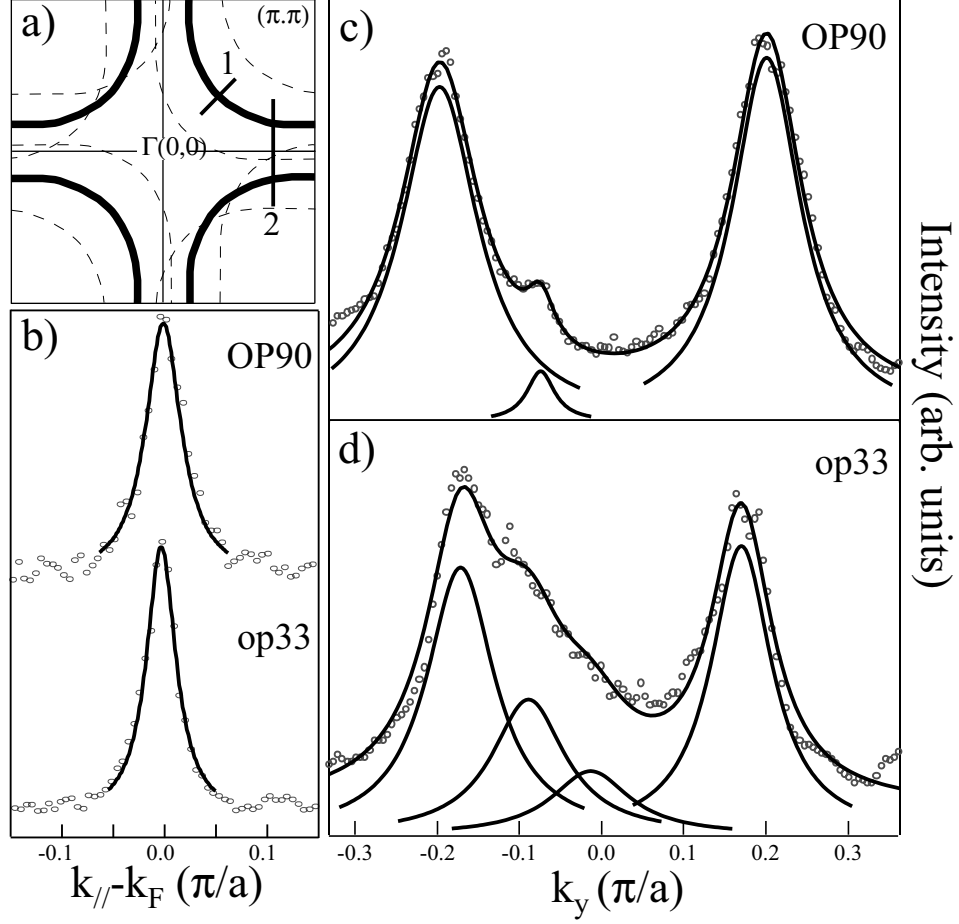


Figure 3.11: (a) Cartoon of the Fermi surface of Bi2201. The thick black curves represent the main Fermi surface and dashed curves represent the Fermi surfaces due to superstructure. Cut #1 and #2 are indicated by straight lines. (b) MDC's at  $E_F$  taken along (b) cut 1 for OP90 and op33, (c) cut 2 for OP90, and (d) cut 2 for op33. The solid lines are Lorentzian fits of the data. Data are taken at 110K for both OP90 and op33. The angular resolution is 0.12 degrees.

is less affected by the superstructure. One can see that the difference between MDC width of OP90 and that of op33 is enlarged in comparison with the nodal cut.

In Fig. 3.12(a), MDC widths extracted from data taken along those cuts shown in the inset are plotted. One can see that the MDC width is at its minimum along the

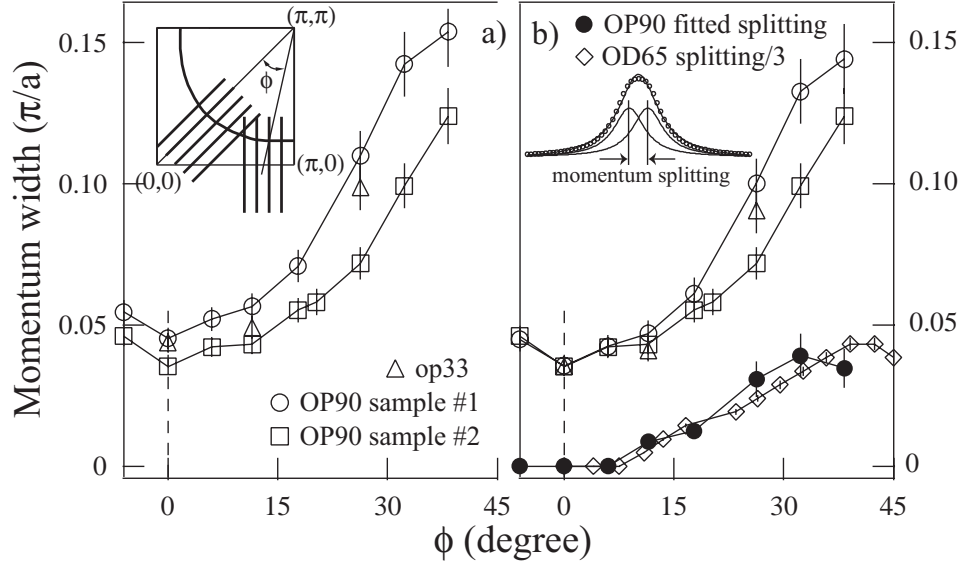


Figure 3.12: (a) MDC width for OP90 and op33 as a function of Fermi surface angle  $\phi$ , which is defined in the inset, e. g.  $k_{\text{node}} = 0$ , and  $(\pi, k_y) = 0$ . Data were taken at the same temperature  $T = 110\text{K}$  for both Bi2212 and Bi2201 and at  $\hbar\omega = 22.7\text{eV}$ . (b) MDC width for OP90 and op33 with the OP90 shifted down so that its minimum matches that of the op33, and the splitting of bonding and antibonding Fermi surfaces for OP90 and OD65. The OD65 momentum splitting is directly measured from EDC's after ref.12. Its amplitude is scaled by a factor of 1/3, and its Fermi surface angle is based on the bonding band crossing. The OP90 momentum splitting is fitted as described in the text. The inset of panel b illustrate fitting process for the estimation of the splitting amplitude.

nodal cut, which assures correct sample alignment. This minimum momentum width changes slightly from sample to sample, and has been attributed to scattering from defects and impurities[114]. Because the bilayer splitting is absent at the d-wave node, and the nodal EDC width is very similar for different samples [Fig. 3.8(a)], we shift the OP90 curve down [Fig. 3.11(b)] so that its minimum matches that of the op33, and take this as the momentum reference point in order to further the quantitative analysis. In fact, the MDC widths at the nearby Fermi surface angles also match. Away from the nodal region toward the  $(\pi, 0)$  region, one sees the MDC width of OP90 becomes increasingly larger than that of op33.

This is consistent with the bilayer splitting scenario. Although experimentally, one only observes a single Lorentzian for Bi2212, this Lorentzian consists of two sub-Lorentzians corresponding to the split bonding and antibonding bands that are separated by certain bilayer momentum splitting, the overall MDC width should be larger than that of op33, which corresponds to a split-free case. If we further assume that both of these two sub-Lorentzians have the same amplitude and width as that of op33 [as illustrated by the inset of Fig. 3.12(b)], one can fit the momentum splitting between these two Lorentzians to reproduce the OP90 MDC. The fitted splitting between the bonding and antibonding Fermi surfaces, are shown in the Fig. 3.12(b). Meanwhile, we can measure the bilayer splitting of OD65 in the momentum space directly from EDC's based on data in ref.[35]. The fitted bilayer splitting of OP90 has similar momentum dependence as that of the OD65, but with only 1/3 of the splitting amplitude. Assuming OP90 and OD65 have similar Fermi velocity, the maximum energy splitting of OP90 would also be 1/3 of that of the OD65, which is about 88 meV[35]. Therefore, we estimate that the bilayer splitting energy in OP90 is about 27 meV. We note that this is just a rough estimation, as our assumption is quite simplified version of the real situation. In the case of OD65, the bonding band actually has sharper MDC width and larger Fermi velocity than that of the antibonding band due to strong bilayer splitting effects. Nevertheless, the symmetric shape of the OP90 MDC's, and the relatively small splitting amplitude that we obtained are consistent with those assumptions. Although the splitting amplitude is smaller in the optimally doped sample, the two split bands are largely broadened, and therefore the overall spectral lineshape could still change in a large energy range with different photon energies.

### 3.2.6 Discussion

Because of the previous lack of evidence for bilayer splitting in optimally doped and underdoped Bi2212 [108, 118], many analyses and calculations assumed its absence. For example, the momentum distribution curves in this region were usually fitted by one Lorentzian[114, 126], when in fact it consisted of two Lorentzians separated by the

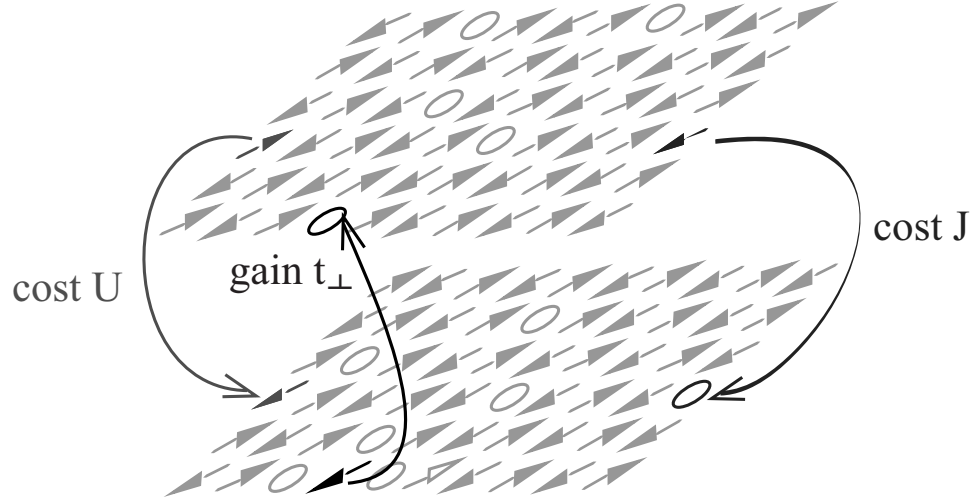


Figure 3.13: A cartoon to illustrate the effective bilayer band splitting is suppressed by correlation effects, whose strength increases with underdoping. Note that the distance between sites are not in real scale.

bilayer splitting in momentum space. Bi2212  $(\pi, 0)$  spectra were discussed [67, 66], and particularly, fitted with a one-component formula[127]. We show that even with a two-component model, there are various uncertainties involved in fitting the spectra, because the bonding and antibonding features are weighted by unknown factors at certain  $\hbar\omega$ 's, and generally too broad to be reliably separated. For overdoped Bi2212, the dip position will be shifted by the overlapping of the two humps and the superconducting peaks.

Intra-bilayer coupling was assumed in some theories to explain the different temperature dependence behavior of c-axis and in-plane transport and optical properties of bilayer systems [128]. Our results reinforce the assumptions of these theories. On the other hand, we find that the quasiparticle in the  $(\pi, 0)$  region of optimally doped Bi2212 should be similar to that of Bi2201, and thus much better defined than previously believed from earlier Bi2212 data. The quasiparticle lifetime is more than 100% longer than obtained from previous EDC analyses, *i.e.*, the scattering rate in this  $(\pi, 0)$  “hot spot” is not as large as previously believed, although an anisotropy of the scattering rate still exists in the optimally doped and underdoped regime, as

is observed in Bi2201[67, 115].

Our results show that bilayer splitting becomes weaker with underdoping, suggesting that the correlation effects strongly reduce the effective intrabilayer coupling. This is illustrated in Fig. 3.13, where correlation effects, such as on-site Coulomb repulsion, and short range anti-ferromagnetic exchange interaction, can hinder the intrabilayer coupling. For example, when one electron hops into an occupied site in the neighboring layer, the hopping process costs the on-site Coulomb repulsion energy; when it hops into a empty site whose neighboring spins have the same orientation as the hopping one, the hopping process costs the in-plane exchange energy  $J > J_{\perp}$ ; only when the neighboring spins have the opposite orientation, the hopping process could gain the energy of  $t_{\perp}$ . With decreasing density of holes, these effects become stronger. Exact diagonalization calculations on double layer t-J model have also shown that the effective intrabilayer coupling strength is proportional to the in-plane quasiparticle renormalization factor  $Z$ , and  $Z$  decrease with increased correlation[106]. Moreover, studies on the bilayer splitting in heavily overdoped Bi2212 found that the experimental intrabilayer coupling amplitude[35] (44meV) is much weaker than that predicted by bare LDA (150 meV) calculations[103], where correlation effects are neglected.

The excitations between two bilayer split bands are dipole-allowed and should have contributions to the c-axis optical absorption spectra in the infrared (IR) region. However, the energy split between the bonding and antibonding bands is not a constant but a continuous distribution from zero to about 90 meV for the heavily overdoped sample. Therefore, it manifest itself in the IR absorption spectrum as a broad hump not a sharp peak like the phonon contributions, considering additional broadening from the correlation effects. In the inset of Fig. 3.14, we plotted the IR spectra taken from Ref.[131] by Motohashi *et al.*. One can see that compare with the optimally doped sample, the IR reflectivity spectrum of the heavily overdoped sample posses a hump in the range of  $400 \sim 600 \text{ cm}^{-1}$ , *i.e.*,  $50 \sim 75 \text{ meV}$ . This could be attributed to the bilayer splitting effects. The split energy range in the optimally doped samples are  $0 \sim 30 \text{ meV}$ , which is not resolvable due to many strong phonon excitations in that energy range. In general, IR spectra have many structures and contains information about large amount of processes that can give optical excitations. It is

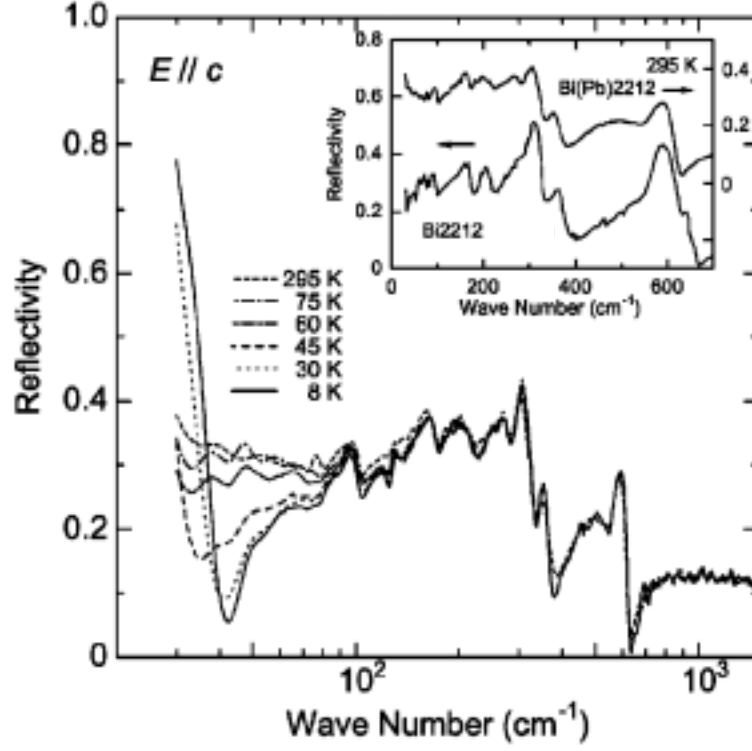


Figure 3.14: (Taken from Ref.[131]). c-axis reflectivity spectra of Bi<sub>1.6</sub>Pb<sub>0.6</sub>Sr<sub>1.8</sub>CaCu<sub>2</sub>O<sub>y</sub> single crystal ( $T_c = 65$  K) at various temperatures. The inset represents the room-temperature spectra of Bi<sub>1.6</sub>Pb<sub>0.6</sub>Sr<sub>1.8</sub>CaCu<sub>2</sub>O<sub>y</sub> and pure Bi2212 ( $T_c = 90$  K).

hard to separate the contributions from the bilayer splitting.

Finally, we discuss the bilayer splitting effects on the superconducting peak analysis discussed in the last chapter. To quantify the peak intensity, the “hump” of the superconducting PDH was fitted out for Bi2212 samples with various dopings up to the  $T_c = 72$  K overdoped sample. In these samples, the normal state spectra are broad, and two split bands, or the normal state PDH structure as found in the heavily overdoped samples, are not resolved; the two superconducting peak are also not resolved. The formula used for the hump-fitting was empirical, and it was used to simply remove the “background” and keep the superconducting peak, which is



defined as the spectral feature that grows upon entering the superconducting state. Therefore this fitting is feasible even the normal state spectrum and superconducting peak contains two unresolvable components. On the other hand, as we have shown in this chapter and in Appendix A, the normal state spectra, the hump, and the superconducting peak all have photon energy dependence due to bilayer splitting and other matrix elements effects. Therefore, the value of SPR depends on the incident photon energy, and one can only compare SPR's based on data taken at the same photon energy, and this has been adapted in our analysis and discussions of the superconducting peak in last chapter. In this regard, the qualitative statements made in last chapter is not affected by the bilayer splitting effect.

### 3.3 Summary

The electronic structure of heavily overdoped  $\text{Bi}_2\text{Sr}_2\text{CaCu}_2\text{O}_{8+\delta}$  is investigated by angle-resolved photoemission spectroscopy. The long-sought bilayer band splitting in this two-plane system is observed in both normal and superconducting states, which qualitatively agrees with the bilayer Hubbard model calculations. The maximum bilayer energy splitting is about 88 meV for the normal state feature, while it is only about 20 meV for the superconducting peak. The different energy splitting scales reported here provide new information for the behavior of the superconducting peak.

Based on ARPES spectra measured on different systems at different dopings, momenta and photon energies, we showed that the anomalously large spectral linewidth in the  $(\pi, 0)$  region of optimal doped and underdoped  $\text{Bi}_2\text{Sr}_2\text{CaCu}_2\text{O}_{8+\delta}$  has significant contributions from the bilayer splitting, and that the scattering rate in this region is considerably smaller than previously estimated. This new picture of the electronic excitation near  $(\pi, 0)$  puts additional experimental constraints on various microscopic theories and data analysis.

We have also tried to estimate the intrabilayer coupling under various assumptions. The intrabilayer coupling is reduced by a factor of three when doping is lowered from OD65 to OP90. This is in a good agreement with resistivity and optical measurements, which showed that the c-axis resistivity and penetration depth of Bi2212

change by a factor of  $3 \sim 6$  in the studied doping range[132, 133, 131].

# Chapter 4

## Electronic Structure of Bi2223

In this chapter, the low-energy electronic structure of the trilayer cuprate superconductor  $\text{Bi}_2\text{Sr}_2\text{Ca}_2\text{Cu}_3\text{O}_{10+\delta}$  near optimal doping is investigated by angle-resolved photoemission spectroscopy. The normal state quasiparticle dispersion and Fermi surface, and the superconducting  $d$ -wave gap and coherence peak are observed and compared with those of single and bilayer systems. We find that both the superconducting gap magnitude and the relative coherence-peak intensity scale linearly with  $T_c$  for various optimally doped materials. This suggests that the higher  $T_c$  of the trilayer system should be attributed to parameters that simultaneously enhance phase stiffness and pairing strength.<sup>1</sup>

### 4.1 Introduction

The high- $T_c$  cuprate superconductors (HTSCs), based on the number of  $\text{CuO}_2$  planes in the characteristic multilayer blocks, can be classified into single-layer materials [e.g.,  $\text{Bi}_2\text{Sr}_2\text{CuO}_{6+\delta}$  (Bi2201),  $\text{HgBa}_2\text{CuO}_{4+\delta}$  (Hg1201), and  $\text{La}_{2-x}\text{Sr}_x\text{CuO}_4$  (LSCO)], bilayer materials [e.g.,  $\text{Bi}_2\text{Sr}_2\text{CaCu}_2\text{O}_{8+\delta}$  (Bi2212),  $\text{HgBa}_2\text{CaCu}_2\text{O}_{6+\delta}$  (Hg1212) and  $\text{YBa}_2\text{Cu}_3\text{O}_{7-\delta}$  (Y123)], trilayer materials [e.g.,  $\text{Bi}_2\text{Sr}_2\text{Ca}_2\text{Cu}_3\text{O}_{10+\delta}$  (Bi2223), and  $\text{HgBa}_2\text{Ca}_2\text{Cu}_3\text{O}_{8+\delta}$  (Hg1223)], and so on. This structural characteristic has a direct correlation with the superconducting properties: within each family of cuprates, the

---

<sup>1</sup>The major content of this chapter has been submitted to Phys. Rev. Lett. (2001).

superconducting phase transition temperature ( $T_c$ ) increases with the layer number ( $n$ ) for  $n \leq 3$ , and then starts to decrease [134, 135]. Taking the Bi-family of HTSCs as an example, the maximum  $T_c$  is approximately 34, 90, and 110 K for optimally doped Bi2201 ( $n = 1$ ), Bi2212 ( $n = 2$ ), and Bi2223 ( $n = 3$ ), respectively. Despite various experimental and theoretical efforts, a conclusive microscopic understanding of this evolution has not yet been reached, partly because of the lack of detailed knowledge about the electronic structure of the trilayer systems. In particular, angle-resolved photoemission spectroscopy (ARPES), one of the most direct probe of the electronic structure of HTSCs [102], has so far been limited to single and bilayer compounds. To gain further insight into the role of multiple  $\text{CuO}_2$  planes in determining the macroscopic physical properties of the cuprates, like the value of the  $T_c$ , it is crucial to extend the investigation of the electronic structure to trilayer HTSCs, and to compare the results with those from the single and bilayer materials. Given that the Bi-based cuprates represent the HTSC family best characterized by ARPES, the trilayer system Bi2223 is the ideal candidate for such a comparative study.

In this chapter, we present the first ARPES study, to the best of our knowledge, of the electronic structure of the trilayer HTSC Bi2223, for which high quality single crystals with dimensions suitable for ARPES measurements has been recently synthesized. As in the single- and bi-layer materials, at nearly optimally doped Bi2223, we observed a large hole-like Fermi surface, a flat quasiparticle band near  $(\pi, 0)$ ,  $d$ -wave pseudo and superconducting gaps, and a large superconducting peak (the so-called coherence peak in the case of Bi2212). The superconducting gap magnitude and the relative weight of the superconducting peak both increase linearly with  $T_c$  for the optimally doped Bi-based HTSCs. This indicates that the higher  $T_c$  of Bi2223 is caused by the enhancement of both pairing strength and phase stiffness, consistent with the idea that optimal doping corresponds to the intersection between phase-coherence and pairing-strength temperature scales. Moreover, the Fermi surface, quasiparticle dispersion, and lineshape analysis indicate a possibly weak intra-trilayer coupling (as compared to the bilayer case of Bi2212 [35, 119]), which suggests that the intra-multi-layer coupling is not the dominant factors for the enhancement of  $T_c$ .

## 4.2 Experimental

Bi2223 single crystals were grown by floating-zone technique. Nearly optimally doped samples [ $T_c = 108$  K,  $\Delta T_c(10\% - 90\%) = 2$  K] were obtained by subsequently annealing the slightly underdoped as-grown Bi2223 crystals ( $T_c = 105$  K) for three days at  $400^\circ\text{C}$  and  $P_{O_2} = 2.1$  atm, and then rapidly quenching them to room temperature. Magnetic susceptibility measurements did not detect the presence of second phases, and X-ray diffraction showed well ordered bulk structures, with the typical superstructure seen in Bi2201 and Bi2212. Optimally doped Bi2212 ( $T_c = 90$  K) and Bi2201 ( $T_c = 34$  K) with  $\Delta T_c(10\% - 90\%) = 1$  K were also studied for comparison. ARPES experiments were performed at the Stanford Synchrotron Radiation Laboratory (SSRL) on a beamline equipped with a Scienta SES200 electron analyzer. Multiple ARPES spectra were acquired simultaneously in a narrow window of  $0.5^\circ \times 14^\circ$  with, unless otherwise specified, an angular resolution of  $0.3^\circ$  (along the cut direction) and an energy resolution of 10 meV. The samples were aligned by Laue diffraction, and cleaved *in-situ* under a pressure better than  $5 \times 10^{-11}$  torr. Bi2223 samples #1, #3 (#2, #4) were cleaved at  $T = 10$  K ( $T = 125$  K). The flatness of the cleaved surfaces was confirmed by the small laser reflection from the samples. Data were collected within 12 hours after cleaving and aging effects were negligible.

## 4.3 Band dispersion, and Fermi surface

Fig. 4.1 presents the normal state ARPES spectra measured on Bi2223 along the high symmetry directions of the first Brillouin zone (BZ). Similar to what has been observed on optimally doped Bi2201 and Bi2212[102], the quasiparticle band is rather flat near  $(\pi, 0)$  while it is quite dispersive and defines a clear Fermi crossing along the  $(0,0)$ - $(\pi, \pi)$  direction. The *umklapp* bands, one of the characteristics of the Bi-family of cuprates, are also detected. The Fermi surface (FS) can be identified by the local maxima of the intensity map obtained by integrating the ARPES spectra within a narrow energy window at the Fermi energy ( $E_F$ ), after the spectra were normalized with respect to the high energy spectral weight. As in the case of Bi2201

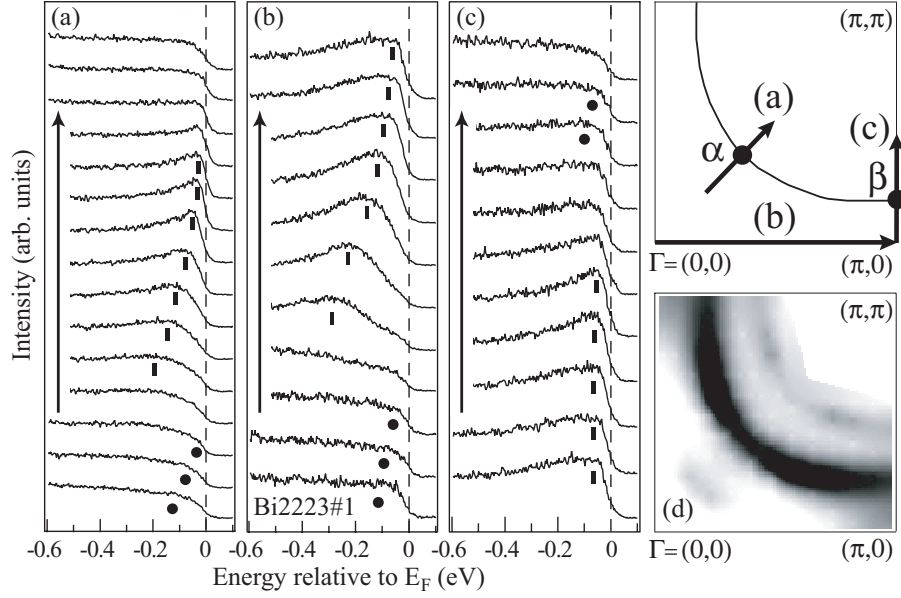


Figure 4.1: (a-c) Normal state Bi2223 ARPES spectra along the high-symmetry lines, as indicated in the BZ sketch (data taken at 125 K with 21.2 eV photons and angular resolution of  $0.24^\circ$ ,  $0.6^\circ$ , and  $0.3^\circ$ , respectively). Main (*umklapp*) bands are marked with bars (circles). (d) Integrated  $E_F$ -intensity map ( $\pm 10$  meV) symmetrized with respect to  $(0,0)$ - $(\pi,\pi)$ .

and Bi2212[102], one main and two weak *umklapp* FSs, shifted by  $\pm(0.21, 0.21)$  with respect to the main FS, are clearly observed (Fig. 4.1d).

## 4.4 Pseudogap and superconducting gap

By tracking the energy position of the leading-edge midpoint (LEM) as a function of temperature and momentum, one can identify an anisotropic pseudogap and a superconducting gap ( $\Delta$ ) consistent with a  $d$ -wave symmetry. Figs. 4.2a and 4.2b show that at  $\pi/2$ , where the FS crossing along the nodal region is found (see the BZ sketch in Fig. 4.1), the LEMs of both normal and superconducting state spectra are located at  $E_F$ , indicating the absence of any gap. On the other hand, in the antinodal region (i.e., at  $\pi$ ) the LEM is always shifted below  $E_F$ , corresponding to an 11 meV pseudogap above  $T_c$  and a 33 meV superconducting gap below  $T_c$ . The momentum

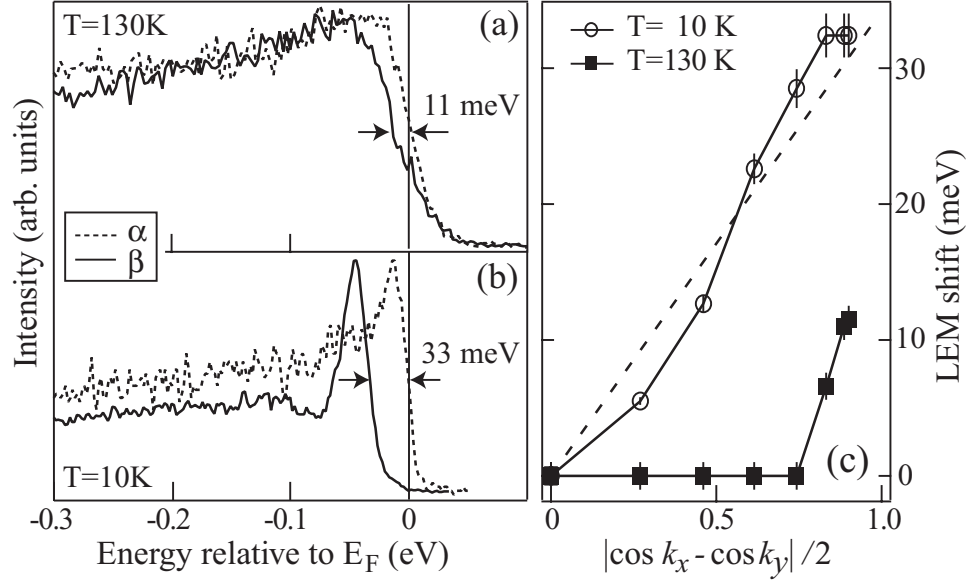


Figure 4.2: (a) Normal and (b) superconducting state Bi2223 spectra measured with 21.2 eV photons at  $\Gamma$  and  $\Sigma$  (see BZ sketch in Fig. 4.1). (c) Position of the leading-edge midpoint (LEM) above and below  $T_c$  along the normal state FS. The dashed line is a fit to the d-wave gap functional form.

dependence of both normal and superconducting state gaps along the normal state FS is summarized in Fig. 4.2c. The superconducting gap can be fitted to the d-wave functional form  $\Delta = \Delta_0 |\cos k_x - \cos k_y|/2$  (where  $\Delta_0$  is the superconducting gap amplitude), while the pseudogap vanishes in wide momentum-space regions resulting in a partially gapped FS (or, equivalently, four disconnected FS arcs in the BZ) at 130 K. Similar phenomena have also been observed in Bi2212 [136]. Furthermore, for the Bi2223 samples #2-4 the pseudogap at  $\Sigma$  was found to vary from 6 to 9 meV at 125 K (which is possibly caused by some small variations in carrier dopings), and the sample with larger pseudogap also has a larger superconducting gap.

Again in analogy with the case of Bi2212[137], in Fig. 4.2 one also notices that the normal state spectrum at  $\Sigma$  sharpens up upon entering the superconducting state, but the most dramatic change in the lineshape takes place at  $\Gamma$ , where the spectrum evolves into a *peak-dip-hump* structure below  $T_c$ . This so-called superconducting peak, which dominates the spectral function in the  $(\Gamma, 0)$  region, has been argued to be an

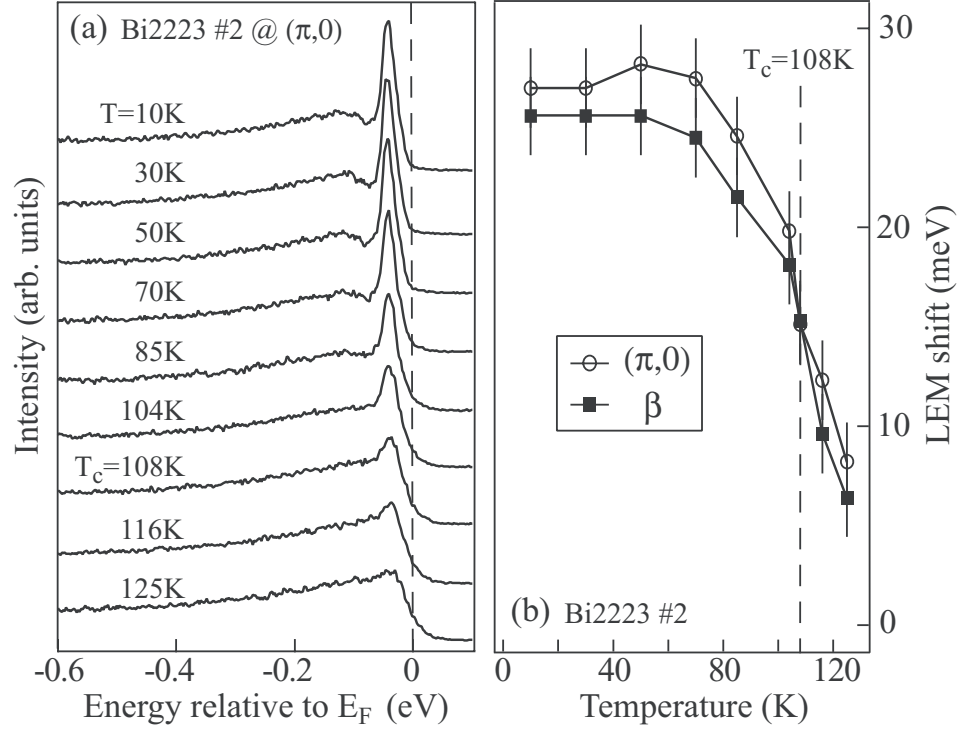


Figure 4.3: (a) Temperature dependence of the Bi2223  $(\pi, 0)$  spectra and (b) of the LEM energy shift at  $(\pi, 0)$  and  $\beta$ .

important characteristics of the HTSCs[138]. It has so far been detected by ARPES only on Bi2212[61] and Y123[99], and the present results substantiate its existence in the spectral function of an  $n=3$  system. In order to gain more information, detailed temperature dependence measurements were performed at  $(\pi, 0)$ , and the results are presented in Fig. 4.3a. The superconducting peak emerges slightly above  $T_c$  (i.e., at 116 K). Upon further cooling the sample below  $T_c$ , its intensity increases rapidly before it eventually saturates at low temperatures, while the total spectral weight is conserved (within 1-2%). At the same time, the LEM shifts to high binding energies reflecting the opening of the superconducting gap (Fig. 4.3b). Note also that, due to the weak quasiparticle dispersion in the flat band region, the spectra at  $(\pi, 0)$  and  $\beta$  exhibit a very similar behavior, as emphasized by Fig. 4.3b.



## 4.5 Compare the normal state lineshape with Bi2201 and Bi2212

Having studied the basic normal and superconducting state spectral properties, we now compare the normal state spectral properties of the trilayer material with those of single and bilayer materials.

The normal state  $(\pi, 0)$  spectra taken with 22.7 eV photons on optimally doped Bi2201, Bi2212 and Bi2223 are presented in Fig. 4.4. One can see interesting non-monotonic behavior with  $n$ : the lineshape for Bi2223 is sharper than that of Bi2201, and broader than that of Bi2212. In Chapter 3, we showed that the large linewidth of spectra near  $(\pi, 0)$  in the optimally doped Bi2212 is due to the bilayer splitting[129], which is caused by the coupling between the neighboring  $\text{CuO}_2$  layers[139]. Because of the broad linewidth for both bonding and antibonding bands, one can only observe a

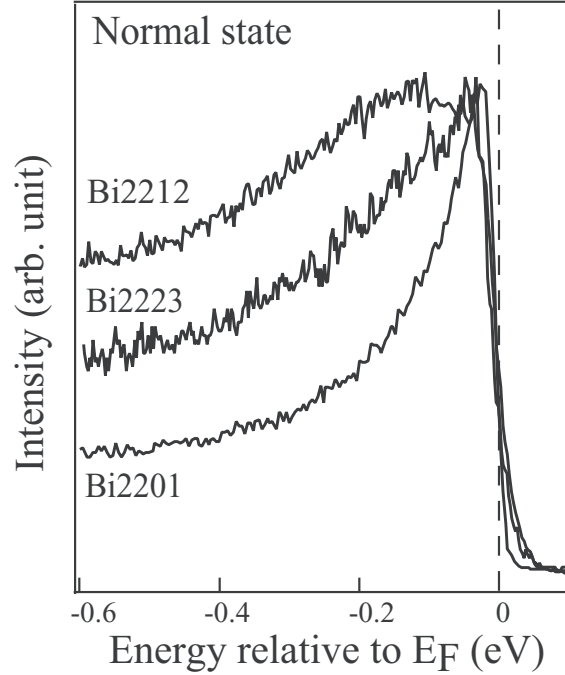


Figure 4.4: Comparison of the normal state  $(\pi, 0)$  spectra of optimally doped Bi2201, Bi2212 and Bi2223. Data were taken with 22.7 eV photons at 10–15 K above  $T_c$  for the normal state spectra.

broad envelope instead of two separated features as have been observed in overdoped Bi2212, where linewidth of both bands are sharp enough to be resolved[35, 119, 120]. Similarly, one would also expect that trilayer splitting due to the intra-trilayer coupling would give rise to *unresolvable* bonding, non-bonding, and antibonding bands. This is consistent with the fact that only one main feature was detected in the normal state spectra and the Fermi surface as shown in Fig. 4.1. However, the nonmonotonic behavior of the linewidth can be naturally explained by assuming that the coupling between neighboring layers is weaker in near optimally doped Bi2223 than that of optimal doped Bi2212. In Fig. 4.5a-c) the normal state  $(\pi, 0)$  spectra from optimally doped Bi2201, Bi2212 and Bi2223 are presented. The photon energy dependence of Bi2201 and Bi2212 have been discussed in last chapter. The large photon energy dependence of the lineshape in Bi2212 was attributed the bilayer splitting. On Bi2223, even though multi-layer splitting is expected, the quasiparticle peak does not show as significant changes with photon energy as on Bi2212. This is also consistent with the weak trilayer splitting idea. We note that this message is not conclusive yet, further investigation, such as the study of heavily overdoped Bi2223, is still needed to resolve this issue.

This postulation of the weak intra-trilayer coupling in Bi2223 could be understood by considering the differences in chemical environment among the three  $\text{CuO}_2$  planes. The two outer  $\text{CuO}_2$  layers have apical oxygens similar to the  $\text{CuO}_2$  layers in Bi2212, while the inner  $\text{CuO}_2$  layer of Bi2223 has no apical oxygen, similar to the electron doped cuprate superconductor  $\text{Nd}_{2-x}\text{Ce}_x\text{CuO}_4$ . It was shown both empirically[140] and theoretically[141] that it is energetically unfavorable to hole-dope a  $\text{CuO}_2$  plane without apical oxygen. Ionic-model calculations show that the inner layer is underdoped[142] or even depleted of holes[134]. Nuclear magnetic resonance experiments show that the Bi2223 inner layer has 15% to 25% less holes than the outer layers [143]. Because the inner layer is underdoped, electronic correlations are strong and will reduce the *effective* hopping between the outer and inner layers [35, 106], and thus weaken the trilayer bandsplitting. This could explain the experimental finding that the normal state  $(\pi, 0)$  spectrum in Bi2223 is sharper than in Bi2212 but broader than in Bi2201 (Fig. 4.4).

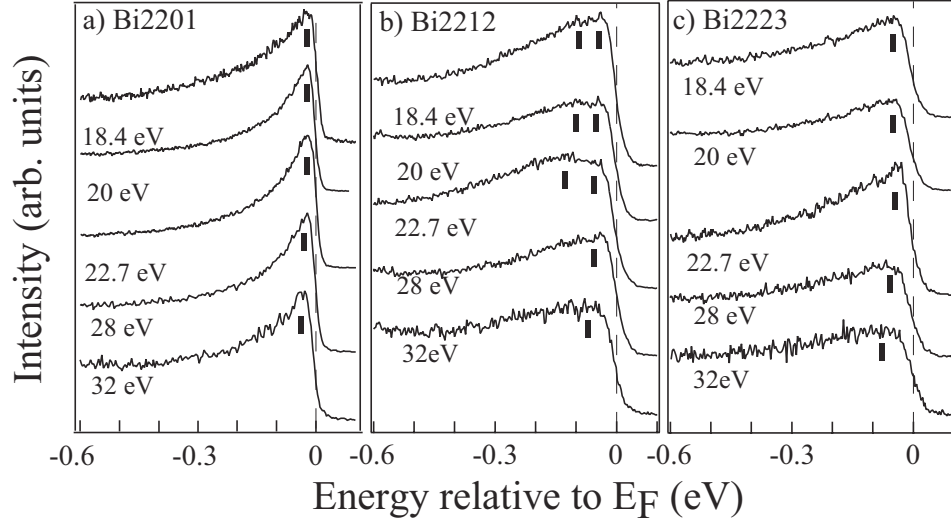


Figure 4.5: Photon energy dependence of the normal state  $(0,0)$  ARPES spectra for optimally doped: (a) Bi2201 at 40 K ( $T_c = 33$  K); (b) Bi2212 at 110 K ( $T_c = 90$  K); (c) Bi2223 at 125 K ( $T_c = 108$  K).

## 4.6 Compare the superconducting state properties for optimally doped cuprates

In Secs. 4.3 and 4.4, we have shown that various properties of Bi2223 qualitatively resemble those of Bi2212 and/or Bi2201. In Sec. 4.5, we have also shown that the intra-multi-layer coupling is not stronger and possibly weaker in Bi2223 than in Bi2212. The natural question is: what part of the electronic structure of Bi2223 can account for the highest  $T_c$  among the Bi-family of cuprates? To further investigate this issue, we compare in Fig. 4.6a the superconducting state  $(0,0)$  spectra from optimally doped Bi2201 and Bi2212, and nearly optimally doped Bi2223 taken under the same experimental conditions (except for the higher energy resolution, i.e. 6 meV, used for the Bi2201 data). The superconducting gap magnitude  $\Delta_0$  can be estimated by either the position of the superconducting peak or the LEM shift below  $E_F$  in the  $(0,0)$  spectra. We found that the average LEM (peak position) gap values are 10 (21), 24 (40), 30 (45) meV for the  $n=1,2,3$  systems, respectively. As shown in Fig. 4.6b, the gap value of the three different systems scales linearly with the corresponding  $T_c$ .

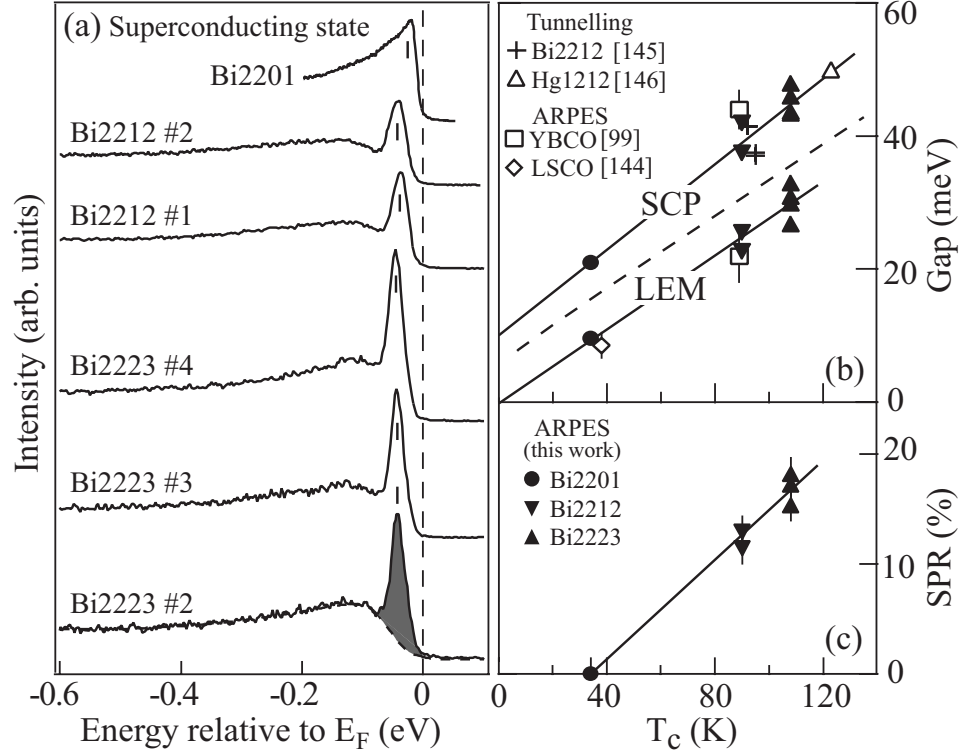


Figure 4.6: (a) Superconducting state ( $\pi, 0$ ) spectra measured at 10 K with 22.7 eV photons on optimally doped Bi2201 and Bi2212, and nearly optimally doped Bi2223. (b) Superconducting gap magnitude as estimated from the position of the superconducting peak (SCP) and the LEM shift (separated by the dashed line), for various optimally doped materials, and (c) superconducting peak ratio (SPR) extracted from the data in (a), plotted versus  $T_c$ .

In particular, the LEM gap can be well fitted by a line across the origin corresponding to an  $n$ -independent ratio  $2\Delta_0/k_B T_c \simeq 5.5$ . Furthermore, from ARPES and tunnelling spectroscopy results reported for other families of cuprates it is found that the values of  $\Delta_0$  for optimally doped LSCO[144], Bi2212[145], YBCO[99]<sup>2</sup>, and Hg1212[146] follow the same gap versus  $T_c$  linear relation (see Fig. 4.6b).

<sup>2</sup>For YBCO, because of the additional gap anisotropy due to the presence of the CuO chains[99], the maximum gap amplitude (i.e., at the Y point) is plotted in Fig. 4.6b). Surface state peak is fitted out before extracting the LEM gap.

From the data presented in Fig. 4.6a, one can also extract the so-called superconducting peak ratio (SPR), which is defined as the ratio between the integrated spectral weight of the superconducting peak and that of the whole spectrum (i.e., from  $-0.5$  to  $+0.1$  eV). As shown in Fig. 4.6a, for the Bi2223 sample #2, the peak intensity is obtained by fitting the smooth “background” with a phenomenological function and then subtracting its contribution to the total integrated weight, as discussed in detail in Chapter 2[34]. For Bi2201, the superconducting peak is not resolved in the ARPES data and therefore its SPR is estimated to be close to zero. In recent scanning tunneling spectroscopy (STS) experiments, a superconducting peak in the density of state was observed for Bi2201. This, however, was detected only at certain locations on the cleaved sample surface and was not resolved in the spatially averaged STS spectra[100], consistent with what is observed by ARPES. For Bi2212 and Bi2223, the spectra in Fig. 4.6a (normalized at high binding energy to allow a direct comparison) indicate that the superconducting peak amplitude for Bi2223 is much larger than that of Bi2212. Overall, the SPRs of these systems scale linearly with  $T_c$  (Fig. 4.6c)<sup>3</sup>. For Bi2212, it has been argued that the SPR is related to the phase stiffness of the condensate or superfluid density ( $\rho_s$ )[34, 113] (see Chapter 2 for details). The weak superconducting peak in the (spatially averaged) ARPES spectra from Bi2201 may then reflect a low superfluid density, and in fact the peak amplitude is negligible also in Bi2212 samples with  $T_c < 50$  K[34]. The  $n$ -dependence of the SPR is qualitatively consistent with the muon spin resonance ( $\mu$ SR) results, which show that  $\rho_s$  for the optimally doped cuprates increases with  $n$  (for  $n \leq 3$ ), and scales with  $T_c$  in approximately a linear fashion as in the celebrated “Uemura plot” [147]. Therefore, the ARPES results together with those from tunneling and  $\mu$ SR indicate that both  $\Delta_0$  and  $\rho_s$  increase with  $T_c$  for the different optimally doped cuprates.

---

<sup>3</sup>We note that Bi2223 and Bi2212 have different structures and thus possibly different photoemission matrix elements. However, the large enhancement of the superconducting peak in Bi2223 and the qualitative aspect of Fig. 4.6c) are not likely just matrix element artifacts.

## 4.7 Discussion

Within current understanding,  $\Delta_0$  and  $\kappa_s$  are the two most important quantities in characterizing the superconducting state, as they reflect the strength of the two basic ingredients of superconductivity: pairing and phase coherence.  $T_\Delta$ , the temperature at which the Cooper pairs start to form, is determined by pairing strength (or  $\Delta_0$ );  $T_\Sigma$ , the temperature at which the Cooper pairs, if any, become phase coherent, is determined by the phase stiffness (or  $\kappa_s$ ). The superconducting phase transition temperature is given by  $T_c = \min(T_\Delta, T_\Sigma)$  [148]. For conventional superconductors,  $T_\Sigma \gg T_\Delta$ ; therefore,  $T_c = T_\Delta$  and phase fluctuations are not important in determining  $T_c$ . The situation is different for the HTSCs: in order to have high  $T_c$ , it is necessary to have both large  $\Delta_0$  and  $\kappa_s$ , as we have seen for nearly optimally doped Bi2223. The reason for this is that HTSCs are doped Mott insulators with low carrier density, for which  $T_\Sigma$  and  $T_\Delta$  are comparable and proposed to have the doping dependence sketched in Fig. 4.7 [148, 149]. The crossing of  $T_\Delta(x)$  ( $x$  being doping) and  $T_\Sigma(x)$  gives  $T_\Delta(x_{opt}) = T_\Sigma(x_{opt}) = T_{c,opt}$  (with the subscript *opt* referring to optimal doping, which is found to be approximately fixed at  $x_{opt} \simeq 0.16$  for many HTSCs [150]). The approximate linear relations  $\Delta_{0,opt} \propto T_{c,opt}$  and  $\kappa_{s,opt} \propto T_{c,opt}$  observed for various optimally doped systems lead to  $T_\Sigma(x_{opt}) \propto \kappa_{s,opt}$  and  $T_\Delta(x_{opt}) \propto \Delta_{0,opt}$ , as theoretically proposed [148].

We have shown that many aspects of the electronic structure of Bi2223, such as the Fermi surface topology and flat band dispersion, resemble those of Bi2212 and Bi2201. The above lineshape analysis suggests that the interlayer coupling between  $\text{CuO}_2$  planes within a multilayer block is not stronger, but possibly even weaker in Bi2223 than in Bi2212. This and the fact that  $T_{c,opt}$  in Hg1201 is comparable to that of Bi2212 indicate that the interlayer coupling within a multilayer block is not the dominant factor for the enhancement of  $T_c$ . Moreover,  $T_{c,opt}$  does not scale with  $n$  in a linear way within a specific HTSC family; and for a given  $n$ , e.g.  $n = 1$ ,  $T_{c,opt}$  varies from 30 K to 100 K for different families of cuprates. Instead, we have shown that  $T_{c,opt}$  scales approximately linearly with both  $\kappa_{s,opt}$  and  $\Delta_{0,opt}$ . One could speculate that the resolution of the  $T_c$  vs.  $n$  problem might be incorporated into a broader task, namely

the search for the parameters that enhance both superconducting gap and superfluid density, and in turn the optimal  $T_c$ . These parameters could be affected by  $n$  and other conspiring factors, for which various candidates have already been proposed, including superconductivity enhancement in the non-CuO<sub>2</sub> layers[151], or as a consequence of impurities and distortion/strain introduced into the system[152, 153]. To highlight these unknown parameters, we add a third axis to the phase diagram of the hole-doped HTSCs (Fig. 4.7), along which both pairing strength and phase stiffness (and thus  $T_{c,opt}$ ) increase with the same monotonic trend, contrary to their opposite trends along the doping axis. In this way, the Bi-based cuprates and possibly different families of HTSCs can be integrated into one comprehensive phase diagram.

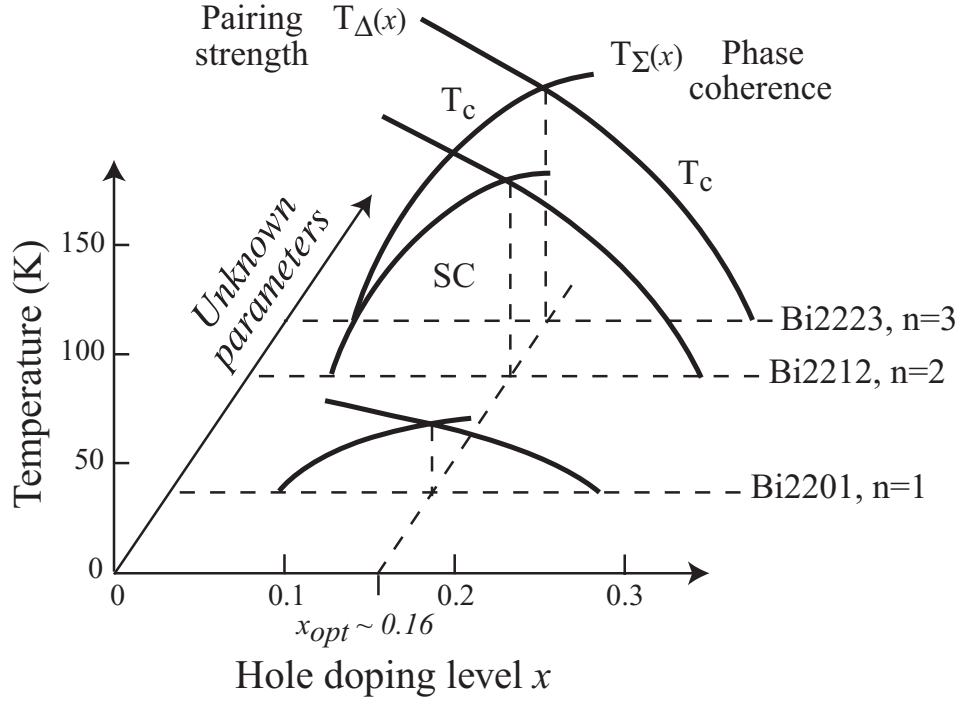


Figure 4.7: Qualitative phase-diagram for the Bi-based HTSCs.

## 4.8 Summary

In summary, we presents the first ARPES investigation of a trilayer cuprate HTSC. We showed that in the normal state, near optimally doped Bi2223 has a large hole-like Fermi surface, and anisotropic pseudogap, in the superconducting state, it has a 45 meV  $d$ -wave superconducting gap and a large superconducting peak. Our results indicate the universality of these features among cuprates. Moreover, our work together with others show that both superconducting gap and phase coherence strength scale with the optimal  $T_c$  for various systems, while the intra-multi-layer coupling does not. To understand the enhancement of  $T_c$  in the trilayer system, one might then need to search for other factors that can enhance both pairing strength and phase coherence in the system.



# Chapter 5

## Conclusion

In this thesis we have presented angle resolved photoemission spectroscopy work on the Bi-family of high temperature superconductors. These systems provide the ideal experimental testing ground for various concepts and fundamental ideas in the field of the strongly correlated system.

We show that the superconducting peak intensity is a signature of the phase coherence in a single particle excitation spectrum, which places a strong constraint on many theories. This, together with the universal appearance of the superconducting peak, suggest that the origin of the superconducting peak may provide the key to understanding its mechanism.

Moreover, we found the long-sought bilayer band splitting in Bi2212, which has very different behavior for normal and superconducting state. We found the scattering rate in the  $(\pi, 0)$  region is much smaller than previously estimated based on the photoemission results. The observed strong photon energy dependence of the lineshape also places a strong constraint on ARPES lineshape analysis of Bi2212 spectra.

For the tri-layer system, we present the first photoemission study. We showed the ubiquitous presence of various properties, including a large hole-like Fermi surface, a d-wave pseudogap and a superconducting gap, flat band region, etc., The intra-tri-layer coupling is found to be fairly weak, suggesting that a stronger interlayer coupling is not related to a higher  $T_c$ . On the other hand, we find that both the superconducting gap magnitude and the relative coherence-peak intensity scale linearly

with  $T_c$  for various optimally doped materials. This suggests that the higher  $T_c$  of the trilayer system should be attributed to parameters that simultaneously enhance phase stiffness and pairing strength.

Various issues remain to be explored, such as the doping dependence behavior of the Bi2223 electronic structure, the origin of the superconducting peak, possible quantum critical behavior in the system, and the different energy scales of the normal and superconducting state bilayer splitting, etc. We leave this for future study.

Our work, together with other theoretical and experimental works, shows that with improvements of experimental techniques and sample quality, the general picture in the field of High temperature superconductors is converging and becoming more clear. A more comprehensive and accurate understanding of the mechanism is on the horizon.

# Bibliography

- [1] F. Bloch, Z. Phys. **57**, 545 (1929).
- [2] A. H. Wilson, Proc. Roy. Soc. A **133**, 458 (1931).
- [3] H. J. De Boer and E. J. W. Verwey, Proc. Phys. Soc. A **49**, 59 (1937).
- [4] Peierls, Comment of Ref. 3
- [5] N. F. Mott, Proc. Phys. Soc. A **62**, 416 (1949).
- [6] J. Hubbard, Proc. Roy. Soc. A, **277**, 237 (1964).
- [7] P. W. Anderson, Phys. Rev. **115**, 2 (1959); Solid State Physics **14**, 99 (1963).
- [8] J. Kondo, Prog. Theoret. Phys. **28**, 846 (1962); **32** 37 (1964); **34** 204 (1965).
- [9] M. B. Brodsky in “Valence Instabilities and Related Narrow Band Phenomena”, edited by R. D. Parks (Plenum, New York, 1977), p. 351.
- [10] P. W. Anderson, Phys. Rev. **124**, 41 (1961).
- [11] J. R. Shrieffer and P. A. Wolff, Phys. Rev. **149**, 491 (1966).
- [12] E. Lieb and F. Y. Wu, Phys. Rev. Lett. **20**, 1455 (1968).
- [13] For a review, “Electron Correlation and Magnetism”, Patrik Fazekas (World Scientific 1999).
- [14] P. Hohenberg and W. Kohn, Phys. Rev. B **136** 864 (1964); W. Kohn and L. J. Sham, Phys. Rev. A **140** 1133 (1964).

- [15] "Theory of the Inhomogeneous Electron Gas" edited by S. Lundqvist and N. H. March (Plenum, 1983); G. D. Mahan and K. R. Subbaswamy, "Local Density Theory of Polarizability", (Plenum, 1990).
- [16] C.M. Varma, *et al.*, Phys. Rev. Lett. **63**, 1996 (1989); **64**, 497 (1990).
- [17] D. Pines, in "High Temperature Superconductivity" edited by K. S. Bedell *et al.*, p. 392, Addison Wesley, New York (1990).
- [18] For example, X.G. Wen and P.A. Lee, Phys. Rev. Lett. **76**, 503 (1996).
- [19] P. W. Anderson, Science **235**, 1196 (1987).
- [20] For a review, J. Orenstein and A. J. Millis, Science **288**, 468 (2000).
- [21] J. G. Bednorz and K. A. Müller, *Z. Phys. B* **64**, 189 (1986).
- [22] J. Zannen, G. A. Sawatzky and J. W. Allen, Phys. Rev. Lett. **55**, 418 (1985).
- [23] F. C. Zhang and T. M. Rice, Phys. Rev. B **37**, 3759 (1988).
- [24] T. Valla *et al.*, Science **285**, 2110 (1999).
- [25] Z. X. Shen *et al.*, Phys. Rev. Lett. **70**, 1553 (1993).
- [26] For a review, T. Timusk and B. Statt, Rep. Prog. Phys. **62**, 61, (1999).
- [27] J. Tranquada *et al.*, Nature **375**, 561 (1995); T. E. Mason, G. Aeppli, H. A. Mook, Phys. Rev. Lett. **68**, 1414 (1992); K. Yamada *et al.*, Phys. Rev. B **57**, 6165 (1998).
- [28] S. H. Pan *et al.*, Nature **403**, 746 (2000); M. Kugler *et al.*, Phys. Rev. Lett. **86**, 4911 (2001).
- [29] D. S. Dessau, *et al.*, Phys. Rev. Lett. **66**, 2160 (1991); D. H. Lu, *et al.* Phys. Rev. Lett. **86**, 4370 (2001); M. Kugler *et al.*, Phys. Rev. Lett. **86**, 4911 (2001).
- [30] T. Senthil and Matthew P.A. Fisher, cond-mat/9912380 (1999).

- [31] S.-C. Zhang, *Science* **275**, 1089 (1997).
- [32] V. J. Emery, S. A. Kivelson, J. M. Tranquada, *Proc. Natl. Acad. Sci. U.S.A.* **96**, 8814 (1999), and references therein.
- [33] Z.-X. Shen and G.A. Sawatzky, *Phys. Stat. Sol.* **215**, 523 (1999).
- [34] D. L. Feng, *et al.*, *Science*, Vol. **289**, 277 (Jul. 2000).
- [35] D. L. Feng *et al.*, *Phys. Rev. Lett.* **86**, 5550, (2001).
- [36] H. Hertz, *Ann. Phys.* **17**, 983 (1887).
- [37] J. J. Thomson, *Phil. Mag.* **48**, 547 (1899).
- [38] P. Lenard, *Wien. Ber.* **108**, 649 (1899); *Ann. Phys.* **2**, 359 (1900); *Ann. Phys.* **8**, 149 (1902).
- [39] A. Einstein, *Ann. Phys.* **31**, 132 (1905).
- [40] G. F. Derbenwick, D. T. Pierce, and W. E. Spicer, in *Methods of experimental Physics*, edited by R. V. Coleman, (Academic Press, 1974), Vol. **11**, p. 67. *Phys. Rev.* **68**, 43 (1945).
- [41] H. Y. Fan, *Phys. Rev.* **68**, 43 (1945).
- [42] H. Mayer and H. Thomas, *Z. Phys.* **147**, 419 (1957).
- [43] H. Puff, *Phys. Stat. Sol.* **1**, 636 (1961).
- [44] C. N. Berglund and W. E. Spicer, *Phys. Rev.* **136**, A1030 (1964).
- [45] C. Caroli , D. Lederer-Rosenblatt, B. Roulett, and D. Saint James, *Phys. Rev.* **8**, 4552 (1973).
- [46] P. J. Feibelman and D. E. Eastman, *Phys. Rev.* **10**, 4932 (1974).
- [47] G. Jezequel and I. Pollini, *Phys. Rev. B* **41**, 1327 (1990).

- [48] G. D. Mahan, *Phys. Rev.* **2**, 4334 (1970).
- [49] M. Cardona and L. Ley, in *Photoemission in Solids I*, edited by M. Cardona and L. Ley, (Springer Verlag, Berlin, 1978) Vol. **26**, and references therein.
- [50] D. D. Vvedensky, in *Unoccupied Electronic States*, edited by J. C. Fuggle and J. E. Inglesfield, (Springer Verlag, Berlin, 1992), p. 139.
- [51] J. W. Gadzuk, M. Šunjić, *Phys. Rev. B* **12**, 524 (1975).
- [52] M. Randeria *et al.*, *Phys. Rev. Lett.* **74**, 4951 (1995).
- [53] M. R. Norman *et al.*, *Phys. Rev. B* **60**, 7585 (1999).
- [54] L. D. Landau, *Sov. Phys. JETP* **3**, 920 (1956); **5**, 101 (1957). **8**, 70 (1959).
- [55] P. Nozières, *Theory of Interacting Fermi Systems*, Benjamin, New York (1964).
- [56] D. Pines and P. Nozières, *The Theory of Quantum Fluids*, vol. 1, Addison-Wesley, New York (1966).
- [57] Th. Straub *et al.*, *Phys. Rev. B* **55**, 13 473 (1997).
- [58] L. Kipp *et al.*, *Phys. Rev. Lett.* **83**, 5551 (1999).
- [59] N. V. Smith, P. Thiry, and Y. Petroff, *Phys. Rev. B* **47**, 15476 (1993).
- [60] *Electron Correlations in Molecules and Solids*, edited by P. Fulde, (Springer Verlag, Berlin, 1995), Vol. **100**, and references therein.
- [61] D. S. Dessau, *et al.*, *Phys. Rev. Lett.* **66**, 2160 (1991).
- [62] J. M. Harris, *et al.*, *Phys. Rev. Lett.* **79**, 143 (1997).
- [63] M. R. Norman, *et al.*, *Phys. Rev. Lett.* **79**, 3506 (1997).
- [64] A. G. Loeser, *et al.*, *Phys. Rev. B* **56**, 14185 (1997).
- [65] A. V. Fedorov, *et al.*, *Phys. Rev. Lett.* **82**, 2179 (1999).

- [66] J. C. Campuzano, et al., Phys. Rev. Lett. 83, 3709 (1999).
- [67] Z.-X. Shen and J. R. Schrieffer, Phys. Rev. Lett. 78, 1771 (1997).
- [68] A. Abanov and A. V. Chubukov, Phys. Rev. Lett. 83, 1652 (1999).
- [69] A. J. Millis, Nature 398, 193 (1999).
- [70] M. R. Presland, J. L. Tallon, R. G. Buckley, R. S. Liu, N. E. Flower, Physica C 176, 95 (1991).
- [71] E. W. Hudson, S. H. Pan, A. K. Gupta, K.-W. Ng, J. C. Davis, Science 285, 88 (1999).
- [72] D. S. Marshall, et al., Phys. Rev. Lett. 76, 4841 (1996).
- [73] P. J. White, et al., Phys. Rev. B 54, R15669 (1996) .
- [74] J. L. Tallon, et al., Physica Status Solidi B 215, 531 (1999) and references therein.
- [75] Y. J. Uemura, et al., Phys. Rev. Lett. 66, 2665 (1991).
- [76] J. L. Tallon and J. W. Loram, Physica C **349 (1-2)**, 53 (2001).
- [77] J. Corson, R. Mallozzi, J. N. Eckstein, I. Bozovic, J. Orenstein, Nature 398, 221 (1999).
- [78] S. Chakravarty, and H.-Y. Kee Phys. Rev. B **61**, 14821 (2000).
- [79] M. Franz and A. J. Millis, Phys. Rev. B 58, 14572 (1998).
- [80] J. Zaanen, Science 286, 251 (1999), and references therein.
- [81] M. I. Salkola, V. J. Emery, S. A. Kivelson, Phys. Rev. Lett. 77, 155 (1996).
- [82] R. S. Markiewicz, Phys. Rev. B **62**, 1252 (2000), and references therein.
- [83] M. G. Zacher, R. Eder, E. Arrigoni, W. Hanke, Phys. Rev. Lett. **85**, 2585 (2000)
- [84] X. J. Zhou, et al., Science 286, 268 (1999).

- [85] E. W. Carlson, D. Orgad, S. A. Kivelson, V. J. Emery, Phys. Rev. B **62**, 3422 (2000).
- [86] S. A. Kivelson, D. S. Rokhsar, J. P. Sethna, Phys. Rev. B 35, 8865 (1987).
- [87] G. Kotliar and J. Liu, Phys. Rev. B 38, 5142 (1988).
- [88] L. B. Ioffe and A. I. Larkin, Phys. Rev. B 39, 8988 (1989).
- [89] T. Tanamoto, K. Kohno, H. Fukuyama, J. Phys. Soc. Jpn. 61, 1886 (1992).
- [90] X.-G. Wen and P. A. Lee, Phys. Rev. Lett. 76, 503 (1996).
- [91] D.-H. Lee, Phys. Rev. Lett. 84, 2694 (2000).
- [92] S. Sachdev, Science 288, 475 (2000) and references therein.
- [93] S. Chakravarty, R. B. Laughlin, D. K. Morr, C. Nayak, Phys. Rev. B **63**, 094503 (2001).
- [94] H. He et al., Phys. Rev. Lett. **86**, 1610 (2001).
- [95] Y. J. Uemura, High-  $T_c$  Superconductivity and C60 Family (proceedings of the 1994 CCAST Symposium, Beijing), S. Feng and H. C. Ren, Eds. (Gordon & Breach, Amsterdam, 1995), pp. 113-142.
- [96] T. Jacobs, S. Sridhar, Q. Li, G. D. Gu, N. Koshizuka, Phys. Rev. Lett. 75, 4516 (1995).
- [97] D. A. Bonn, et al., Phys. Rev. B 50, 4051 (1994).
- [98] J. E. Sonier, et al., Phys. Rev. Lett. 83, 4156 (1999).
- [99] D. H. Lu, et al. Phys. Rev. Lett. **86**, 4370 (2001).
- [100] M. Kugler et al., Phys. Rev Lett. **86**, 4911 (2001).
- [101] S. H. Pan et al., Nature (accepted).



- [102] D. W. Lynch and C. G. Olson, “Photoemission Studies of High-Temperature Superconductors”, Cambridge University Press (1999); Z.-X. Shen and D. S. Dessau, Physics Reports, **253**, 2 (1995). A. Damascelli, D.H. Lu, and Z.-X. Shen, J. Electron Spectr. Relat. Phenom. **117-118**, 165 (2001), and references therein.
- [103] S. Massidda *et al.*, Physica C **152** 251 (1988); W. E. Pickett, Rev. Mod. Phys. **61** (2), 251 (1989).
- [104] S. Chakravaty *et al.*, Science **261**, 337 (1993).
- [105] O. K. Anderson *et al.*, J. Phys. Chem Solids **12**, 1573 (1995).
- [106] R. Eder *et al.*, Phys. Rev. B **51**, 3265 (1995).
- [107] A. I. Liechtenstein *et al.*, Phys. Rev. B **54**, 12505 (1996).
- [108] H. Ding *et al.*, Phys. Rev. Lett. **76**, 1533 (1996).
- [109] S. Rast *et al.* Europhys. Lett. **51** (1), 103 (2000). An abrupt change in the measured ARPES spectra at a new temperature scale  $T^+ \approx 85\text{K}$  is also reported. However, it is not observed in our experiments.
- [110] Z. Yusof and B. O. Wells, private communication.
- [111] P. Aebi *et al.*, Phys. Rev. Lett. **72**, 2757 (1994).
- [112] D. L. Feng *et al.*, unpublished.
- [113] H. Ding *et al.*, cond-mat/0006143.
- [114] T. Valla *et al.*, Phys. Rev. Lett. **85**, 828 (2000).
- [115] R. Hlubina and T. M. Rice, Phys. Rev. B **51**, 9253 (1995); B. P. Stojković and D. Pines, Phys. Rev. Lett. **76**, 811 (1996).
- [116] C. Kim *et al.*, Phys. Rev. Lett. **80**, 4245 (1998).

- [117] M. Eschrig, and M. R. Norman, *ibid.* **85**, 3261 (2000).
- [118] J. Mesot *et al.*, cond-mat/0102339 (2001).
- [119] Y.-D. Chung *et al.*, cond-matt/0102386.
- [120] P. Bogdanov *et al.*, cond-mat/0005394.
- [121] Z. Yusof *et al.* cond-matt/0104367.
- [122] M.R. Presland, *et al.*, Physica C **176**, 95 (1991).  $T_c = T_{c,max}[1 - 82.6(x - 0.16)^2]$ ,  
 $T_{c,max} = 33K$  , and  $91K$  for Bi2201 and Bi2212 respectively.
- [123] J. M. Harris *et al.*, Phys. Rev. Lett. **79**, 143 (1997).
- [124] T. Sato, *et al.*, Phys. Rev. B **63**, 132502 (2001).
- [125] A. Bansil *et al.*, Phys. Rev. Lett. **83**, 5154 (1999).
- [126] P. V. Bogdanov *et al.*, Phys. Rev. Lett. **85**, 2581 (2000).
- [127] For example, M. R. Norman and H. Ding, Phys. Rev. B **57**, R11089 (1998); M.  
R. Norman *et al.*, Phys. Rev. B **63**, 140508 (2001).
- [128] L. B. Ioffe, and A. J. Millis, Phys. Rev. B **58**, 11631 (1998).
- [129] D. L. Feng *et al.*, submitted to Phys. Rev. Lett. (2001).
- [130] T. Valla *et al.*, Science **285**, 2110 (1999).
- [131] T. Motohashi *et al.*, Phys. Rev. B **61**, R9269 (2000).
- [132] H. Shibata and A. Matsuda, Phys. Rev. B **59**, R11672 (1999).
- [133] T. Motohashi *et al.*, Phys. Rev. B **59**, 14080 (1999).
- [134] M. Di Stasio, K.A. Muller, and L. Pietronero, Phys. Rev. Lett. **64**, 2827 (1990),  
and references therein.
- [135] J.M. Tarascon *et al.*, Phys. Rev. B **38**, 8885 (1992).

- [136] D. S. Marshall *et al.*, Phys. Rev. Lett. **76** 4841 (1996); M. Norman *et al.*, Nature, **392**, 157 (1998).
- [137] A. Kaminski *et al.*, Phys. Rev. Lett. **84**, 1788 (2000).
- [138] For example, D.-H. Lee, Phys. Rev. Lett. **84**, 2694 (2000); T. Senthil and M. P. A. Fisher cond-mat/9910224. E. W. Carlson, D. Orgad, S. A. Kivelson, V. J. Emery, Phys. Rev. B **62**, 3422 (2000).
- [139] O.K. Andersen *et al.*, J. Phys. Chem. Solids **12**, 1573 (1995); A.I. Lichtenstein *et al.*, Phys. Rev. B **54**, 12 505 (1996).
- [140] Y. Tokura *et al.*, Phys. Rev. B **39**, 9704 (1989); Nature **337**, 345 (1989).
- [141] J. Kondo, J. Phys. Jpn. **58**, 2884 (1989); Y. Ohta, T. Tohyama and S. Maekawa, Phys. Rev. B **43**, 2968 (1991).
- [142] R.P. Gupta and M. Gupta, Phys. Rev. B **49**, 13154 (1994).
- [143] A. Trokiner *et al.*, Phys. Rev. B **44**, 2426 (1991).
- [144] X.J. Zhou *et al.*, unpublished.
- [145] Ch. Renner *et al.*, Phys. Rev. Lett. **80**, 149 (1998); Y. De Wilde *et al.*, *ibid.* 153 (1998); N. Miyakawa *et al.*, *ibid.* 157 (1998).
- [146] J.Y.T. Wei *et al.*, Phys. Rev. B **57**, 3650 (1998). Due to large variations of the reported gap values of Hg-based cuprates by different tunnelling experiments, only result on single crystal Hg1212 is plotted in Fig. 4.6b).
- [147] Y.J. Uemura *et al.*, Nature **364**, 605 (1993), and references therein.
- [148] V.J. Emery and S. Kivelson, Nature **374**, 434 (1995).
- [149] Y.J. Uemura, Physica C **282-287**, 194 (1997), which also shows that  $\Delta_s$  (and thus  $T_\Delta$ ) eventually decreases in the overdoped regime. It is omitted here for simplicity, and will not affect the qualitative conclusions drawn here.

- [150] M.R. Presland *et al.*, Physica C **176**, 95 (1991); J. Tallon *et al.*, Phys. Rev. B **51**, 12911 (1995); S. Ono *et al.*, Phys. Rev. Lett. **85**, 638 (2000).
- [151] T.H. Geballe and B.Y. Mozysh, Physica C **341-348**, 1821 (2000).
- [152] H. Eisaki *et al.*, private communication.
- [153] A. Bianconi *et al.*, Int. J. Mod. Phys. B **14**, 3342 (2000).

# Appendix A

## Intriguing data, possible new physics

In this appendix, I present a collection of intriguing ARPES data on the the Bi-family of cuprates as well as some from other cuprates. They are “figures in the drawer”, *i.e.*, the meaning of many of these data are still to be explored, and hopefully new physics would be discovered with further experiments and analyses.

### A.1 Electronic structure of heavily overdoped Bi2201

The following data were taken on heavily overdoped  $\text{Bi}_{1.7}\text{Pb}_{0.3}\text{Sr}_2\text{CuO}_{6+\delta}$ , ( $T_c=5\text{K}$ ) at  $T=12\text{K}$  with He-I light.

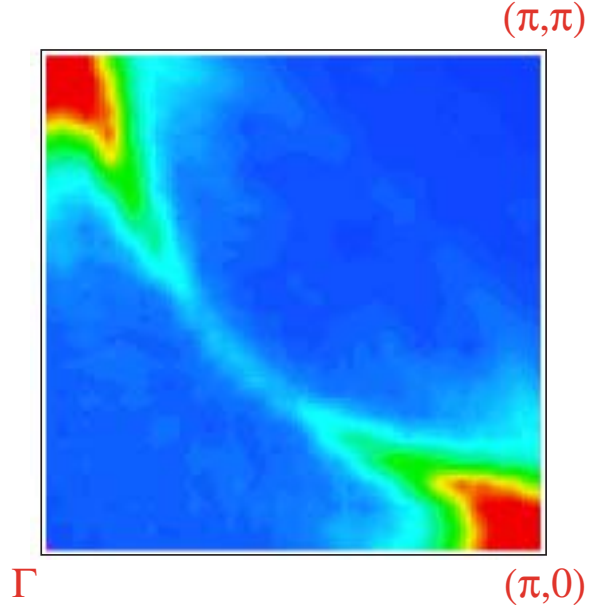


Figure A.1: (color) Fermi surface mapping by spectral weight integrated over  $[-20\text{meV}, 10\text{meV}]$ , data were symmetrized along  $(0,0) - (\pi, \pi)$ .

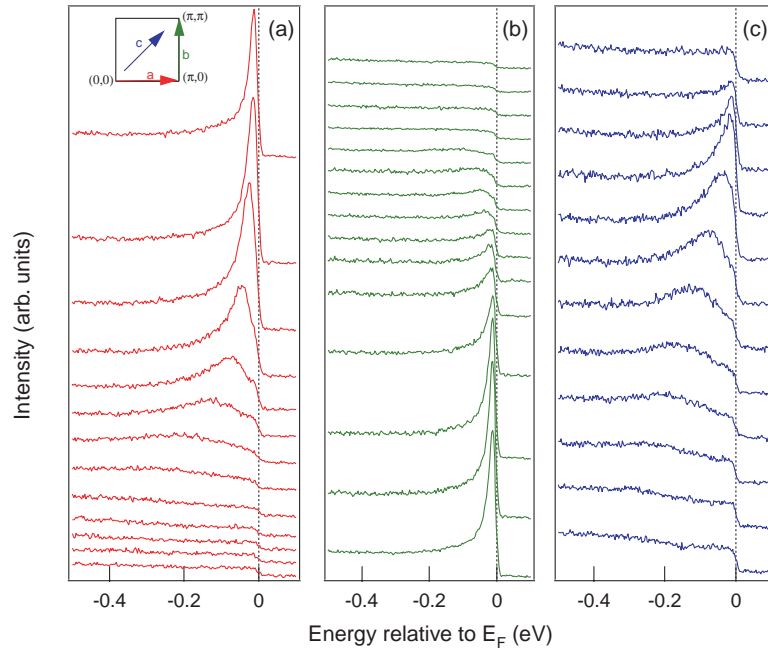


Figure A.2: (color) Spectra along high symmetry lines for heavily overdoped Bi2201.

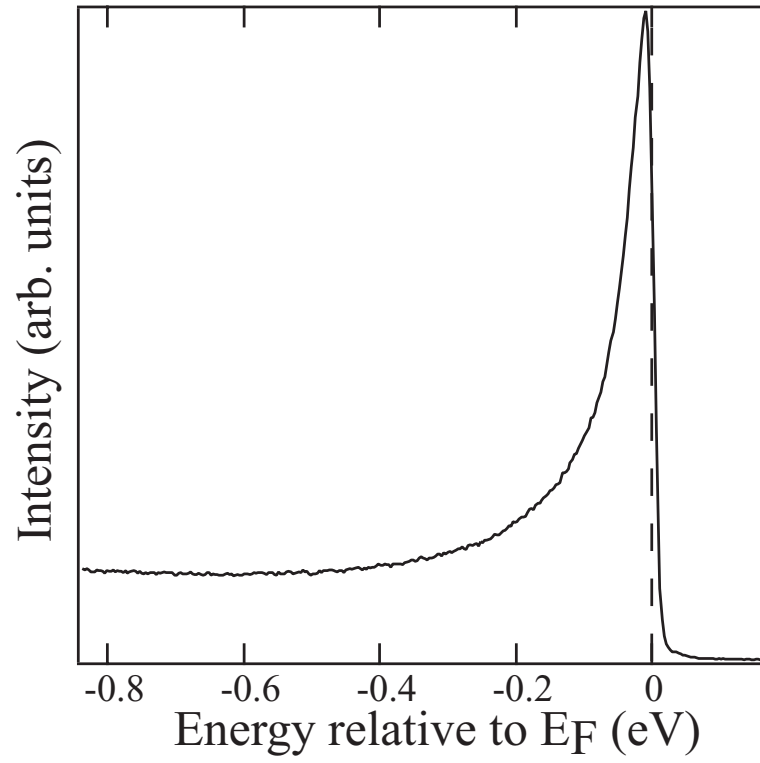


Figure A.3:  $(\pi, 0)$  spectrum taken at  $T=11\text{K}$  in the normal state for OD5 Bi2201, which indicates the correlation is weak and quasiparticle concept is more suitable for this heavily overdoped system than the underdoped systems.

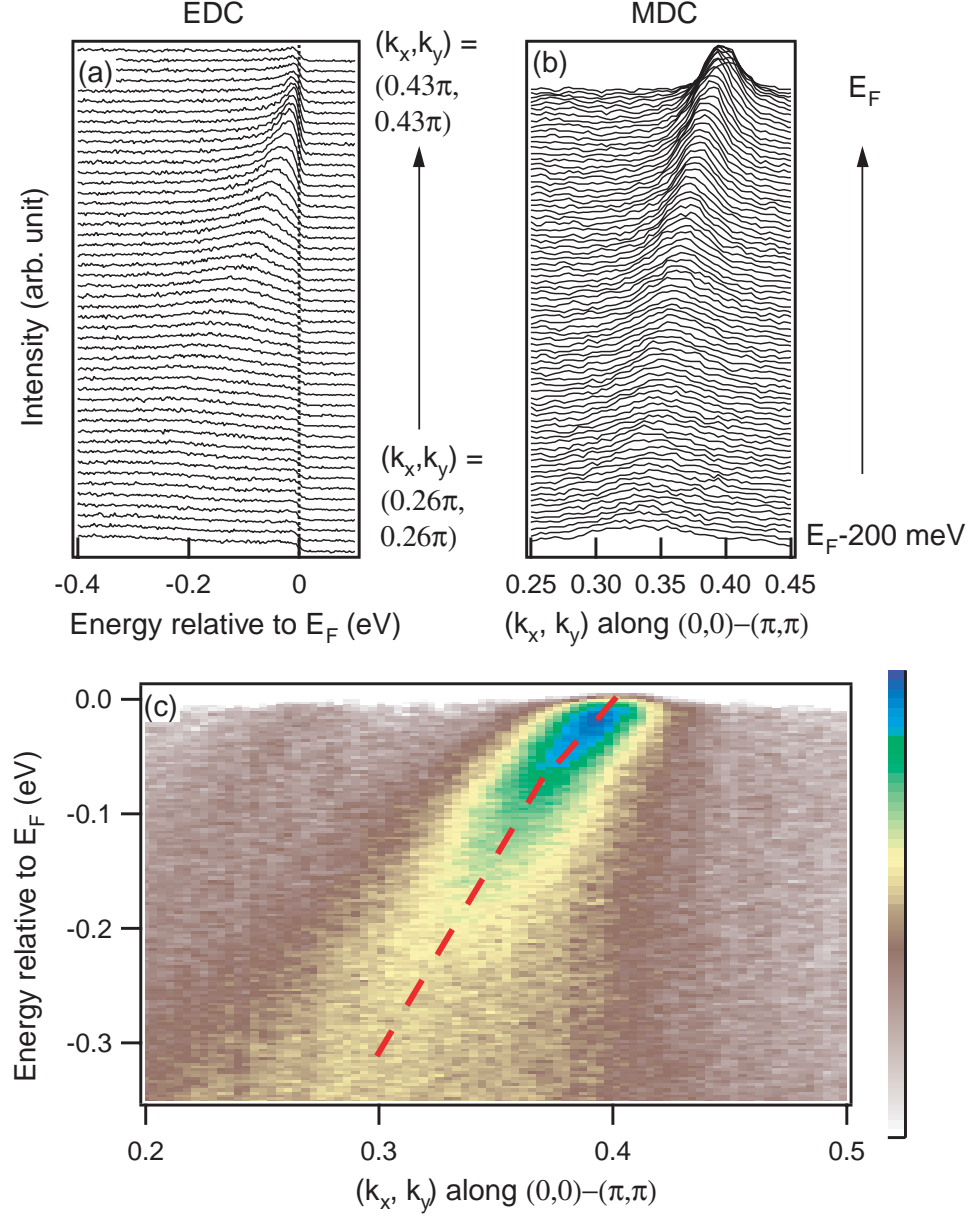


Figure A.4: (color) (a) EDC, (b) MDC, and (c) photoemission intensity map for the  $(0,0) - (\pi, \pi)$  nodal cut. The observed kink in dispersion indicates that it is not related to gap or Neutron  $(\pi, \pi)$  resonance, and it clearly exist in the normal state.



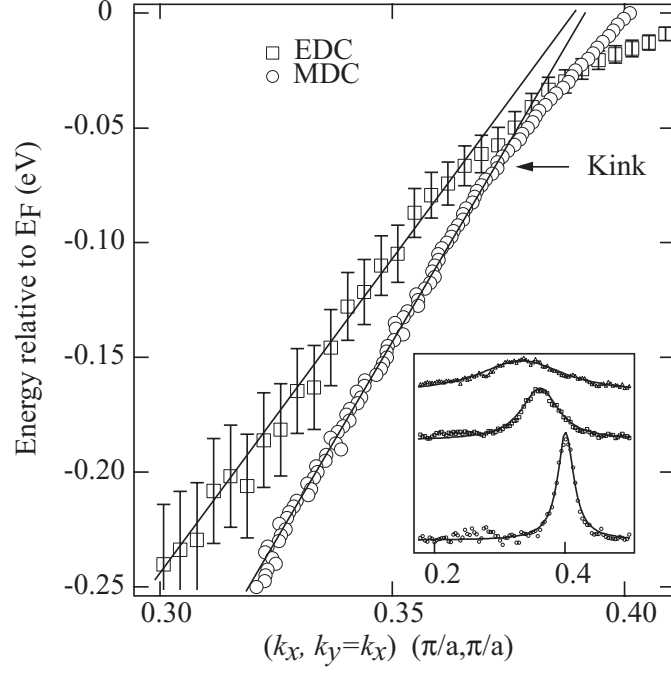


Figure A.5: Kink in the dispersion obtained through EDC and MDC analyses. The inset shows that the MDC's could be fitted by Lorentzians very well.

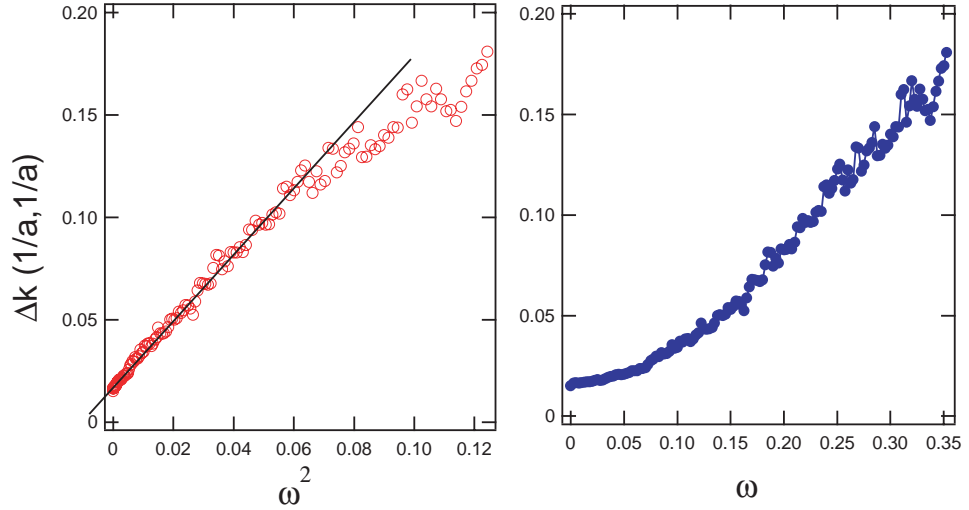


Figure A.6: Scattering rate obtained through the MDC analysis plotted as a function of energy, which can be fitted to the Fermi liquid formula  $\Gamma \propto \omega^2$ .

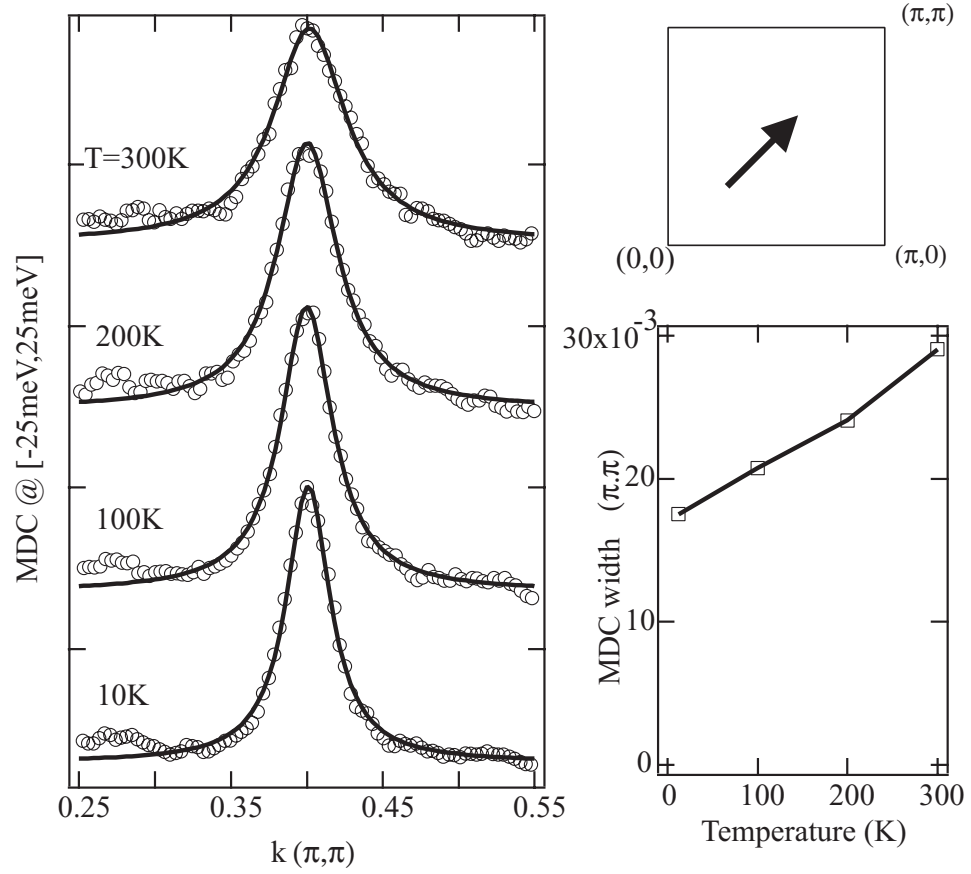


Figure A.7: Scattering rate near  $E_F$  obtained through the MDC as a function of temperature for heavily overdoped Bi2201.

## A.2 Photon energy dependence of the superconducting peak

The following figures show that the superconducting peak and the hump have different photoemission matrix elements. Its physical meaning is still to be explored.

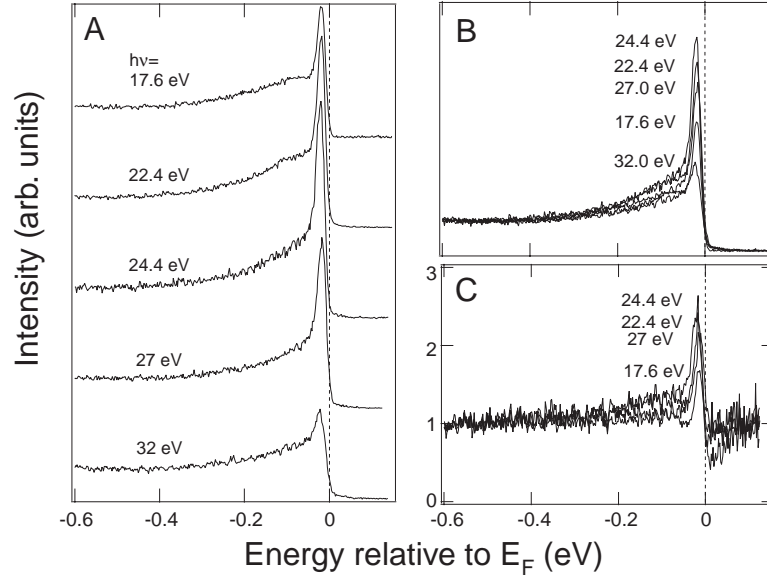


Figure A.8: (A) ARPES spectra at  $(\pi, 0)$  for Pb-Bi2212 OD82.5 (superstructure free), taken at  $T=12\text{K}$  with different photon energies. (B) same as (A) but spectra are stacked on each other. (C) spectra taken at 24.4 eV, 22.4 eV, 27 eV, 17.6 eV were divided by spectrum taken at 32 eV. Labels in B and C were in the order of peak height.

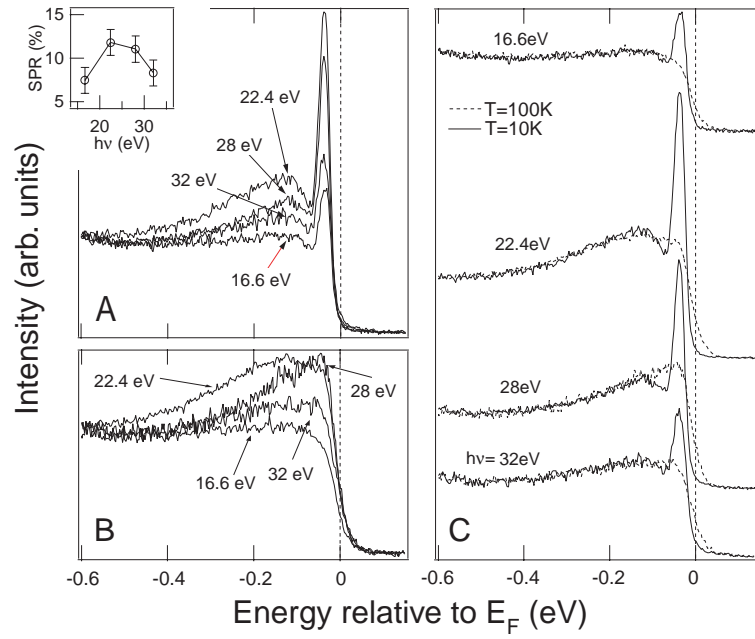


Figure A.9: ARPES spectra at  $(\pi, 0)$  for pure Bi2212 OP90 taken with different photon energies (A) at  $T=10K$ ; (B) at  $T=100K$ . (C) Spectra in A and B are stacked together. Inset in A shows superconducting peak ratio (SPR) as a function of photon energy.

### A.3 Dispersion of the superconducting peak

The dispersion of the superconducting peak is still not understood.

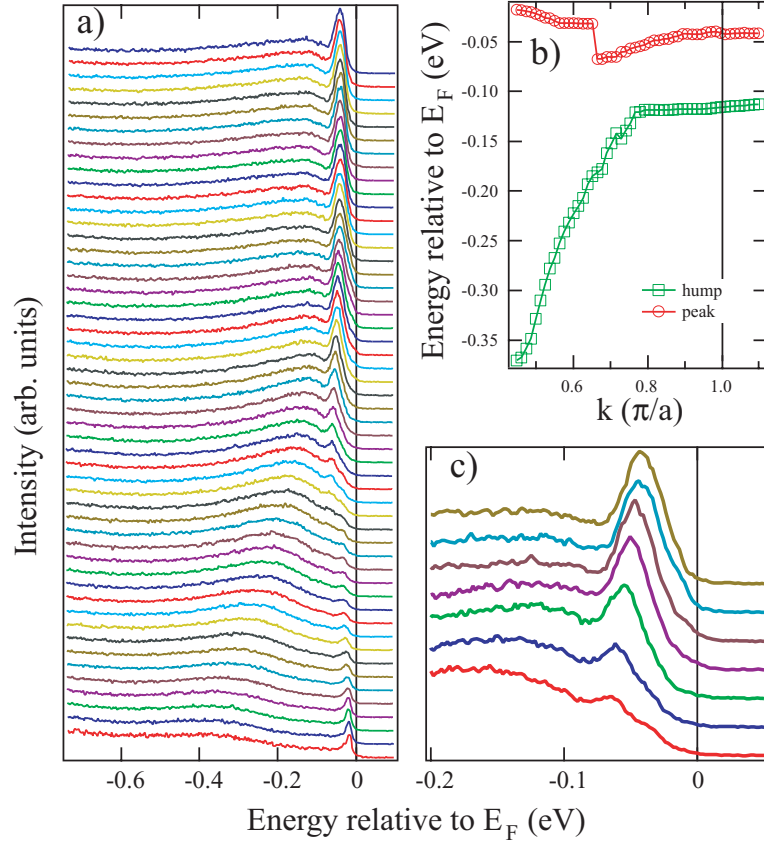


Figure A.10: (color) (a) ARPES spectra along the  $(0,0) - (\pi,0)$  direction for optimally doped OP90 Bi2212 in the superconducting state. (b) The dispersion of the peak and hump extracted from (a), where the break in the superconducting peak dispersion is due to its superstructure image. (c) Selected spectra from (a) to highlight the superconducting peak dispersion.

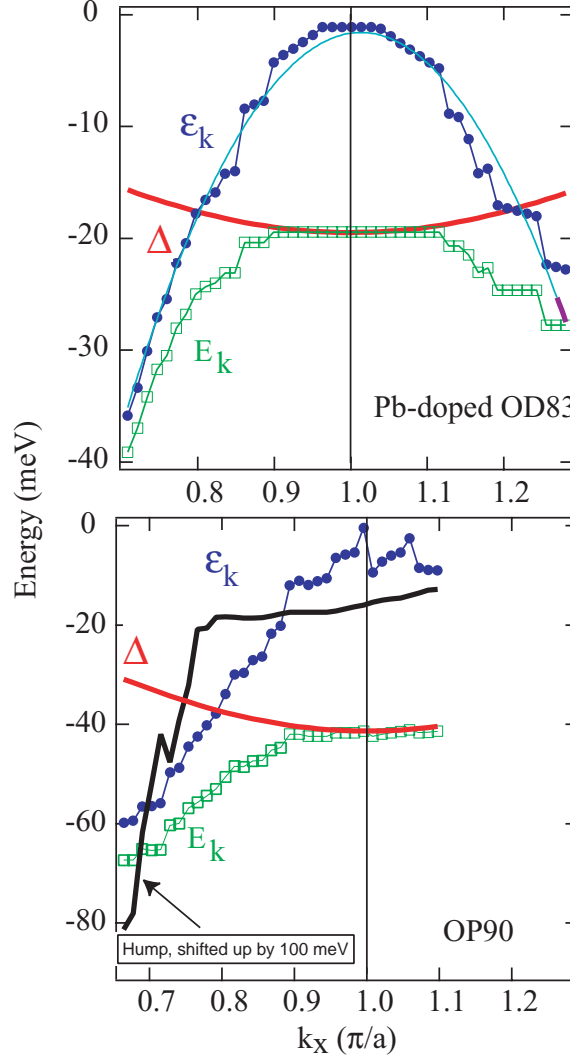


Figure A.11: (color) An intriguing (based on two assumptions) way to look at the superconducting peak dispersion. The superconducting peak position  $E_k$  is assumed to be  $\sqrt{\frac{2}{k} + \Delta(k)^2}$ , where  $\frac{2}{k}$  is the normal state dispersion of an underlying band (assuming it exist), and  $\Delta$  is the superconducting gap, which has the  $d$ -wave form. By assuming the underlying band is at  $E_F$  at  $(\pi, 0)$ ,  $\epsilon_k$  is obtained. The resulting  $\epsilon_k$ 's for (a) Pb-OD83 and (b) OP90 are obtained, which can be fitted by a parabolic function and resemble the dispersion of a free boson.

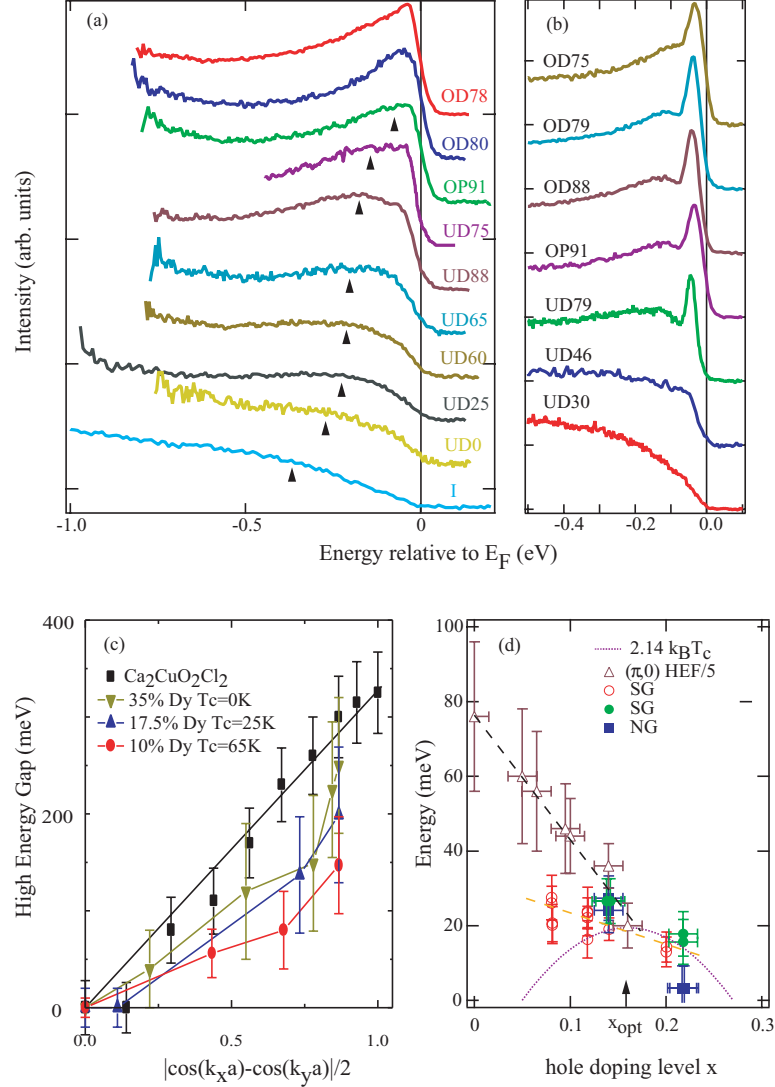


Figure A.12: (color) (a) The normal state  $(\pi, 0)$  spectra as a function of doping give the so-called high energy feature (HEF) or high energy pseudogap, while (b) the superconducting state  $(\pi, 0)$  spectra as a function of doping give the superconducting gap (SG). (c) HEF has  $d$ -wave form, which smoothly evolves to the HEF of antiferromagnetic parent compound  $\text{Ca}_2\text{CuO}_2\text{Cl}_2$ . The amplitudes of low energy pseudogap (NG), SG, and HEF is summarized in (d) as a function of doping. The relation between these energy scales is an important issue that needs to be further studied.

## A.4 Fermi surface, and spectral weight distribution of Bi2212

The topology of the Fermi surface of Bi2212 was hotly debated over the last several years. It is still not clear whether the two Fermi surfaces observed in Bi2212 are due to the bilayer band splitting effects or just matrix element effects or maybe both.

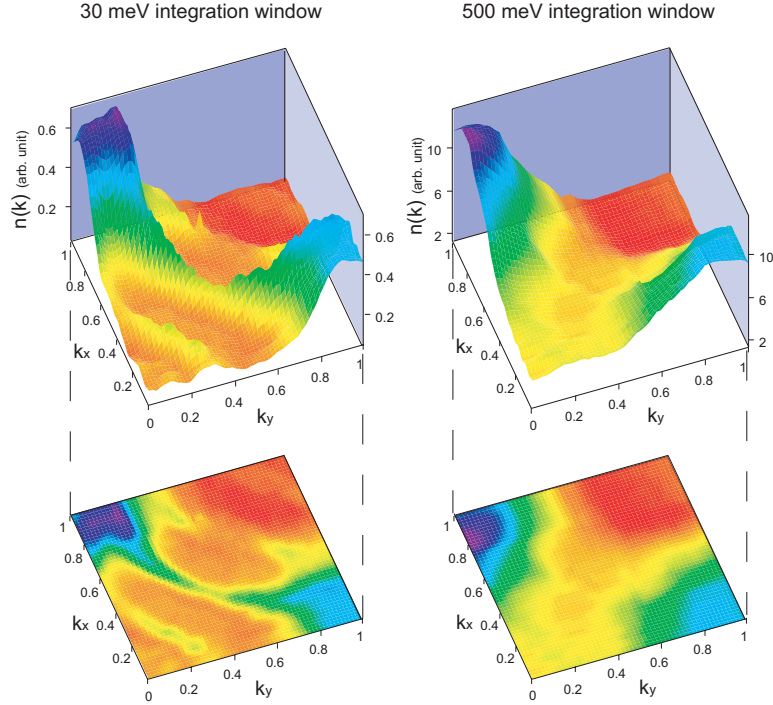


Figure A.13: (color) ARPES spectral weight distribution in the momentum space can be used to determine the Fermi surface, by identifying the local maximum of the low energy spectral weight (left column), or the steepest decent of the total spectral weight (right column). Here data taken from optimally doped OP90 Bi2212 are used as an example.



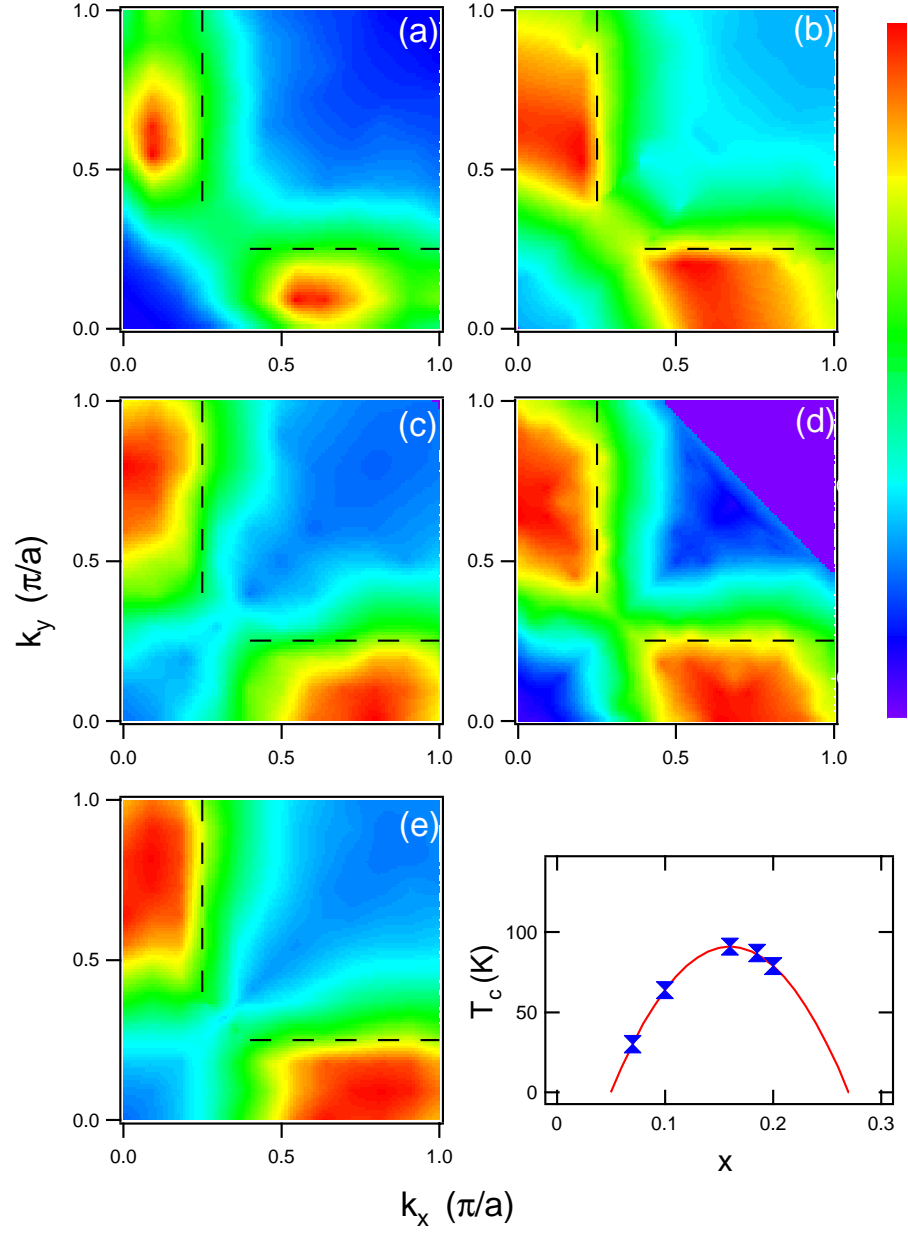


Figure A.14: (color) Two fold symmetrized spectral weight integrated over  $[E_F - 0.5 \text{ eV}, E_F + 0.1 \text{ eV}]$  for Bi2212 samples: (a) UD30, (b) UD60, (c) OP91, (d) OD87, and (e) OD78. The inset shows their position on the  $T_c - x$  diagram. Dashed lines show the spectral weight is mainly confined within  $\pm \pi/4$  region. Data were taken in the  $k$ -space octant  $\Gamma(0,0) - \bar{M}(\pi,0) - Y(\pi,\pi) - \Gamma(0,0)$  at a temperature of 10~20 K above  $T_c$ . Data were taken at SSRL Beamline V-3.

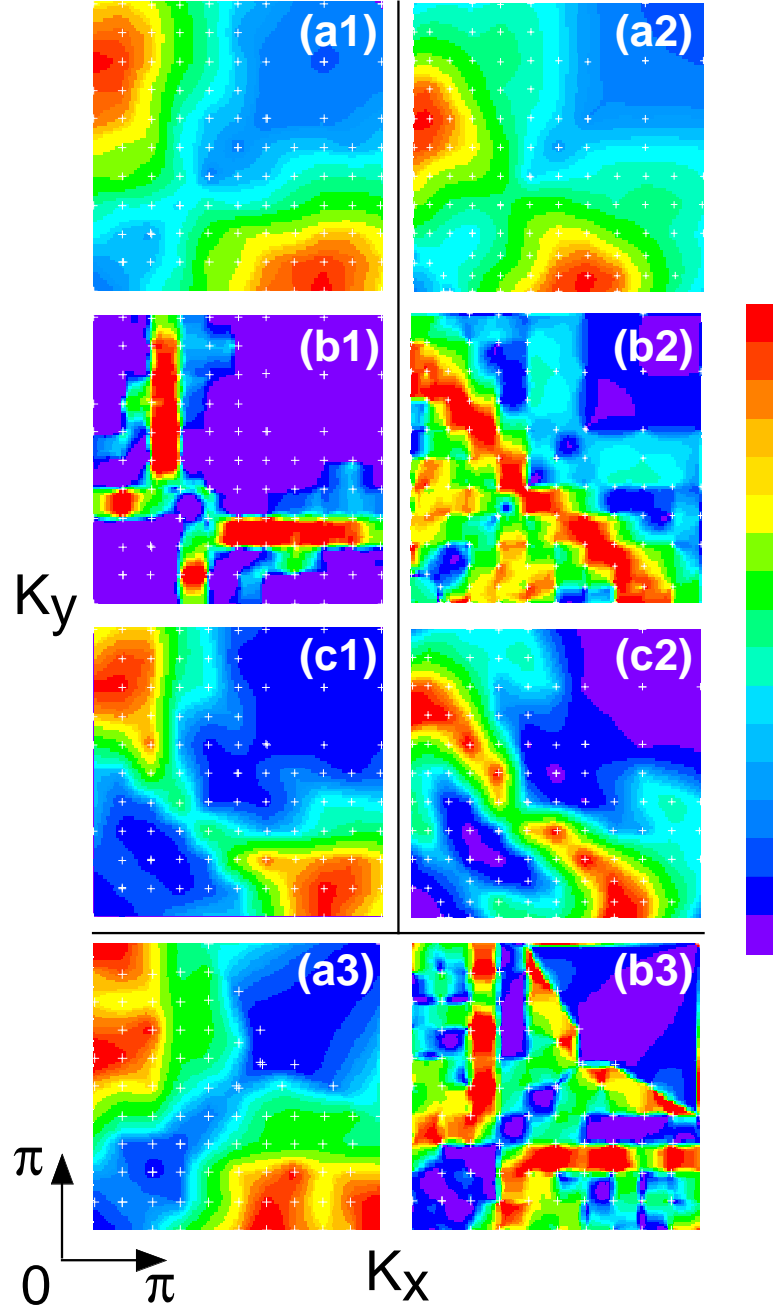


Figure A.15: (color) Two-fold symmetrized scale plots of the optimally doped sample ( $T_C \sim 90$  K) with the white crosses representing the sampled  $k$  points. (a1), (b1), and (c1) show  $n(k)$ ,  $|\nabla_{\vec{k}} n_{\vec{k}}|$ , and  $A(k, E_F)$  respectively for data taken at 22.4 eV photon energy. (a2), (b2), and (c2) show  $n(k)$ ,  $|\nabla_{\vec{k}} n_{\vec{k}}|$ , and  $A(k, E_F)$  respectively for data taken at 32.3 eV photon energy. (a3) and (b3) show  $n(k)$  and  $|\nabla_{\vec{k}} n_{\vec{k}}|$  respectively for data taken at 55 eV photon energy. The ranges of  $k_x$  and  $k_y$  are both from 0 to  $\pi$  for all eight panels. Data were taken at SSRL Beamline V-3.

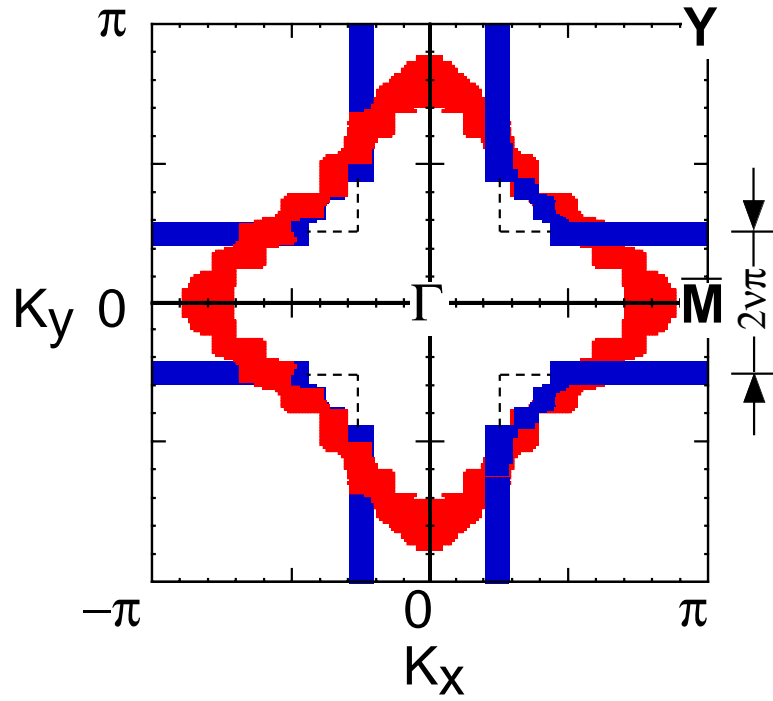


Figure A.16: (color) Eight-fold symmetrized experimental Fermi surface as derived from the local  $|\nabla_{\vec{k}} n_{\vec{k}}|$  maxima locus in previous figure for OP90 Bi2212. The distance between the nesting pieces is denoted as  $2\delta$ .

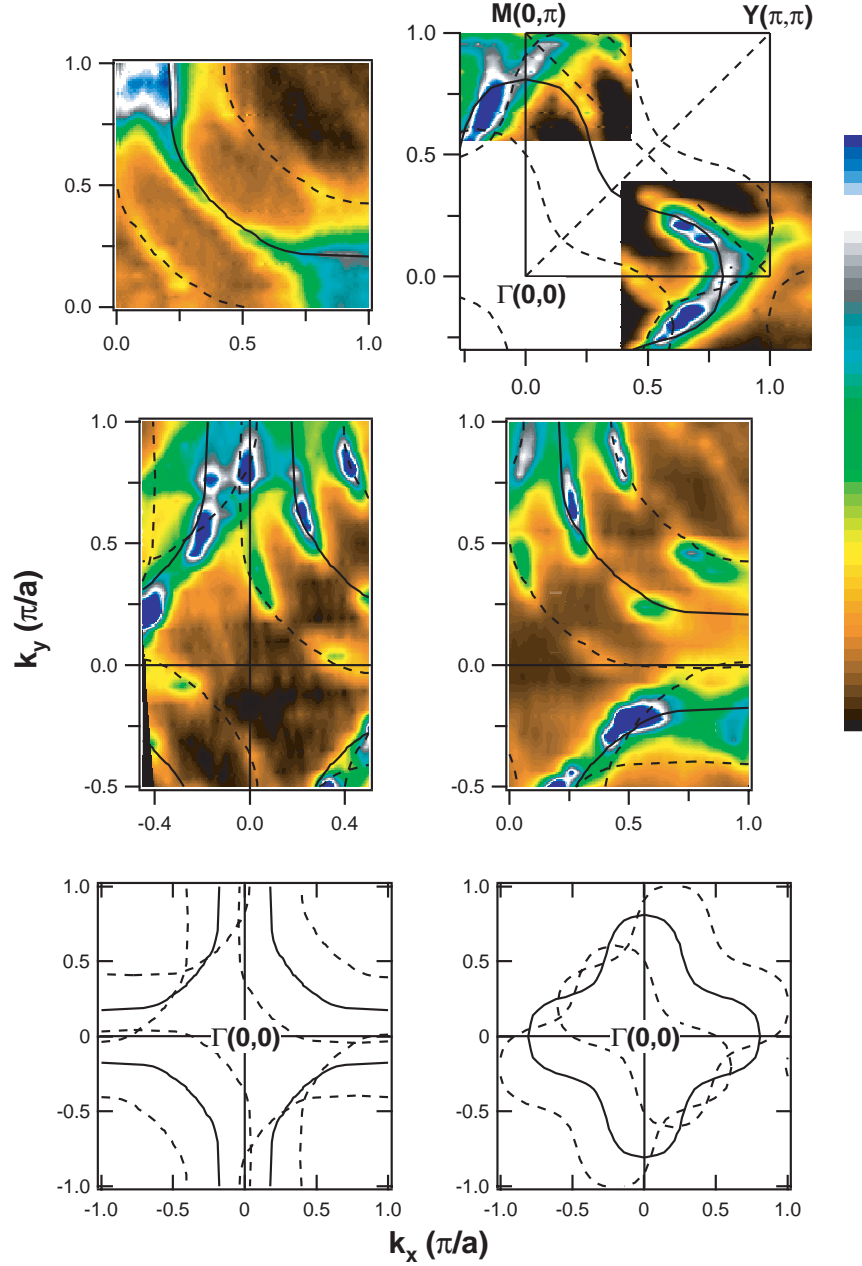


Figure A.17: (color) Normal state spectral weight distributions of the OP91 Bi2212 system integrated over 30 meV window near  $E_F$ . Data are taken with 21.2 He-I photon at SSRL (upper left panel), 33 eV polarized synchrotron light at ALS (upper right panel), and 55 eV polarized synchrotron light at ALS (middle two panels). Curves laid on top are cartoons for the different Fermi surfaces which are considered to be the best fit of the data at certain photon energy. Dashed curves represents the superstructure induced Fermi surface. Lower panels show the two different Fermi surface topologies under debate. One can see that photoemission matrix element does play an important role here.

## **A.5 Fermi surface, and spectral weight distribution of Bi2201**

The study of the Fermi surface of Bi2201 will benefit our understanding of that of Bi2212. However, it is still an open question whether the two Fermi surfaces observed in Bi2201 are real (certainly not caused by bilayer splitting) or another matrix element induced artefact.

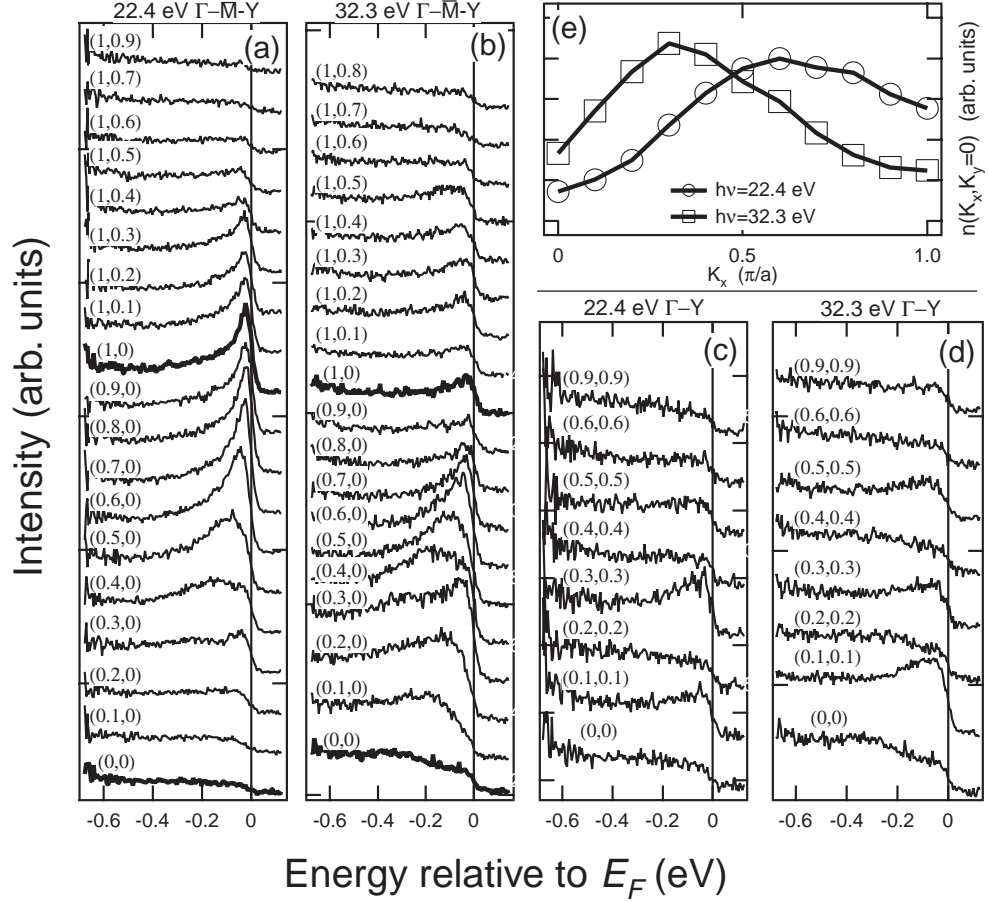


Figure A.18: ARPES spectra of overdoped  $\text{B}_{1.1}\text{Sr}_{1.9}\text{CuO}_{6+y}$ , ( $T_c = 8\text{K}$ ) at (a) 22.4 eV along the  $\Gamma-\bar{\text{M}}-\text{Y}$  cut; (b) 32.3 eV along the  $\Gamma-\bar{\text{M}}-\text{Y}$  cut; (c) 22.4 eV along the  $\Gamma-\text{Y}$  cut; (d) 32.3 eV along the  $\Gamma-\text{Y}$  cut, and (e) the spectral weight  $n(\mathbf{k})$  along  $\Gamma-\bar{\text{M}}$  at 22.4 eV (circles) and 32.3 eV (squares)

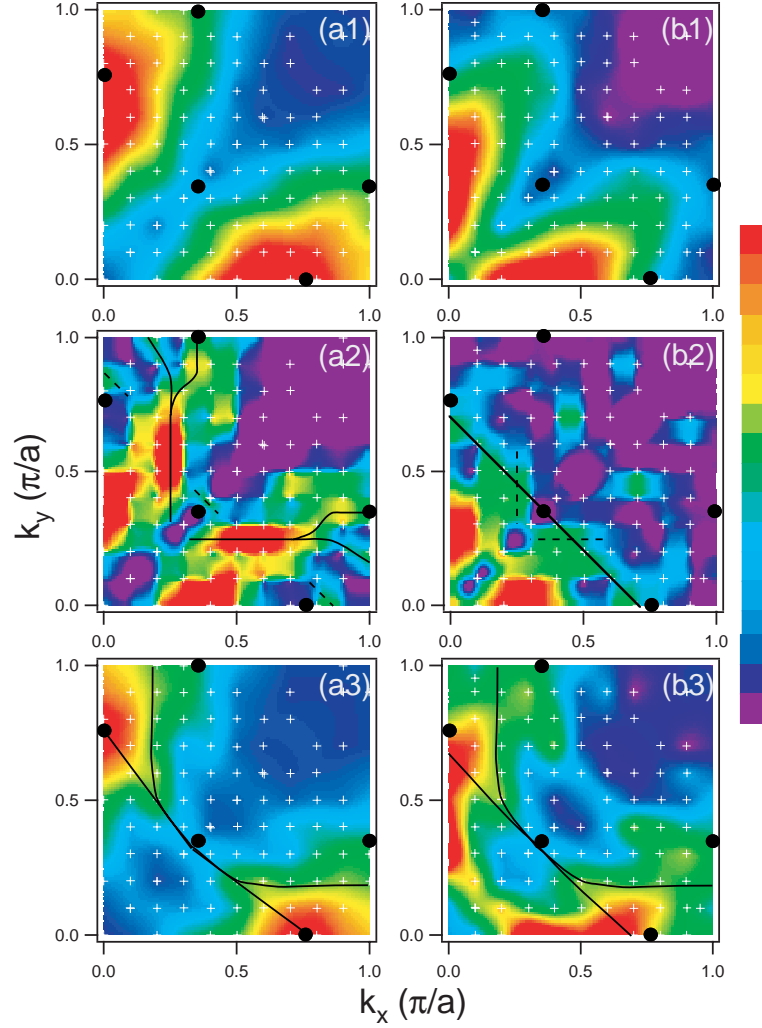


Figure A.19: (color) Two-fold symmetrized scale plots for the overdoped  $\text{Bi}_{2.1}\text{Sr}_{1.9}\text{CuO}_{6+y}$ , ( $T_c = 8\text{K}$ ) with the white crosses representing the sampled  $\mathbf{k}$  points. (a1), (a2), and (a3) show  $n(\mathbf{k})$ ,  $|\nabla_{\vec{k}} n_{\vec{k}}|$ , and  $A(\mathbf{k}, E_F)$  respectively for data taken at 22.4 eV photon energy in arbitrary units. (b1), (b2), and (b3) show  $n(\mathbf{k})$ ,  $|\nabla_{\vec{k}} n_{\vec{k}}|$ , and  $A(\mathbf{k}, E_F)$  respectively for data taken at 32.3 eV photon energy. The color bar on the right indicates the linear color scales of the shown quantities. The Fermi vectors determined by the dispersion method are shown as the black solid circles; the FS determined by the  $\nabla n$  method (in a2 and b2) are shown as solid lines (more emphasized piece) and dashed lines (less emphasized piece); and the FS determined by the  $\max-A(\mathbf{k}, E_F)$  (in a3 and b3) method are shown as solid lines. These determined FS have the error of  $\pm 0.045$  in (a2) and (a3) and  $\pm 0.06$  in (b2) and (b3), the error bars are not shown to avoid blocking the data.

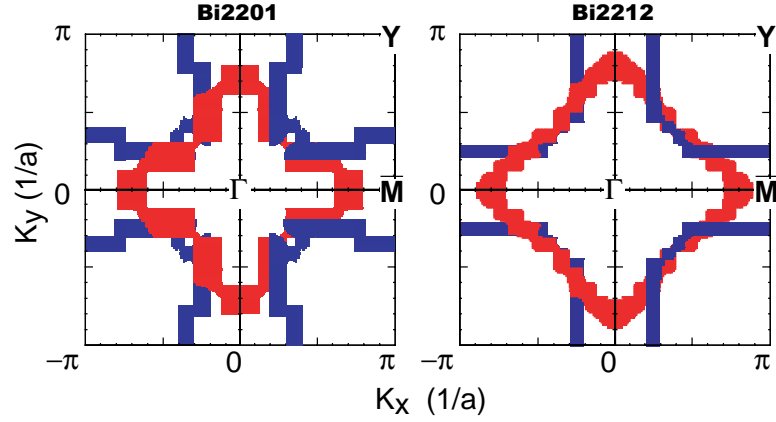


Figure A.20: (color) (a) Four-fold symmetrized experimental FS of the overdoped  $\text{Bi}_{1.1}\text{Sr}_{1.9}\text{CuO}_{6+y}$  ( $T_c = 8\text{K}$ ) derived from the local  $|\nabla_{\vec{k}} n_{\vec{k}}|$  maxima in the previous figure; (b) Four-fold symmetrized experimental Bi2212 FS reproduced from Fig. A.16.

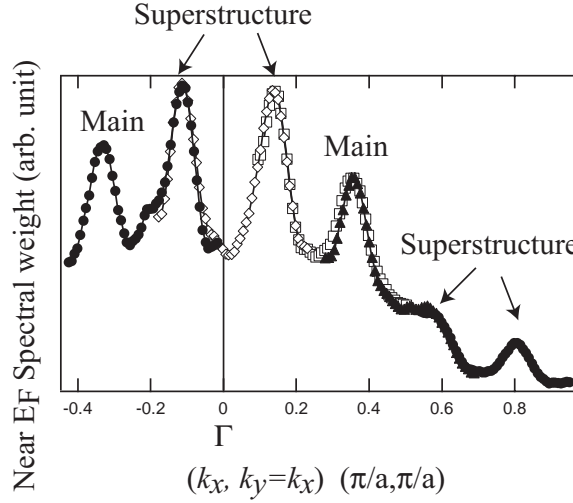


Figure A.21: Near  $E_F$  spectral weight for near optimally doped Bi2201 ( $T_c \sim 29\text{K}$ ) along the  $(-\pi/a, -\pi/a) - (\pi/a, \pi/a)$  direction, which consists of several experimental cuts. Data were taken with He-I light. It shows that the superstructure weight near  $(0,0)$  is even stronger than the main feature, particularly considering the matrix element usually vanishes near  $(0,0)$ . This usually happens when the superstructure in Bi2201 is strong, which indicates that the photoemission process and the superstructure effects are very complicated in Bi2201.



## A.6 Random interesting figures

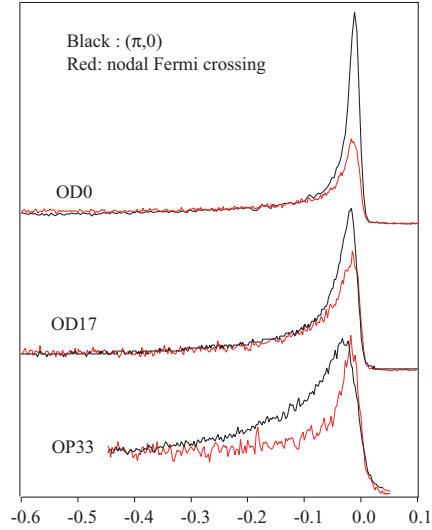


Figure A.22: (color) Comparison between the normal state spectra at  $(\pi,0)$  and the nodal Fermi crossing for three Bi2201 samples: OP33, OD17, OD0. It shows that the  $(\pi,0)$  scattering is reduced with increased doping. The  $(\pi,0)$  spectrum is even sharper than the nodal spectrum for OD0 sample.

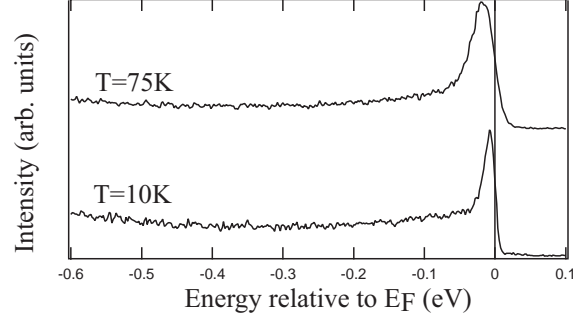


Figure A.23: ARPES spectra at the nodal Fermi crossing of heavily overdoped OD65 Bi2212. A kink is clearly visible in the superconducting state spectrum.

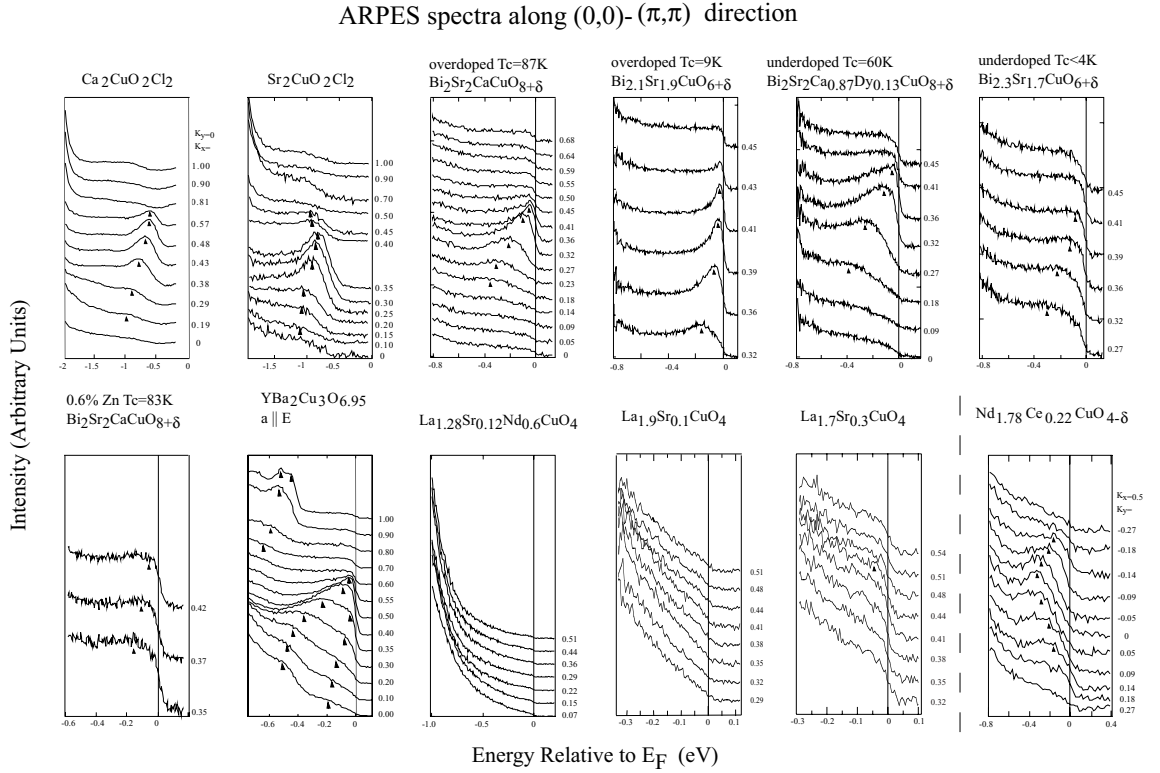


Figure A.24: A comparison of ARPES spectra along  $(0,0) - (\pi, \pi)$  directions for various cuprates.

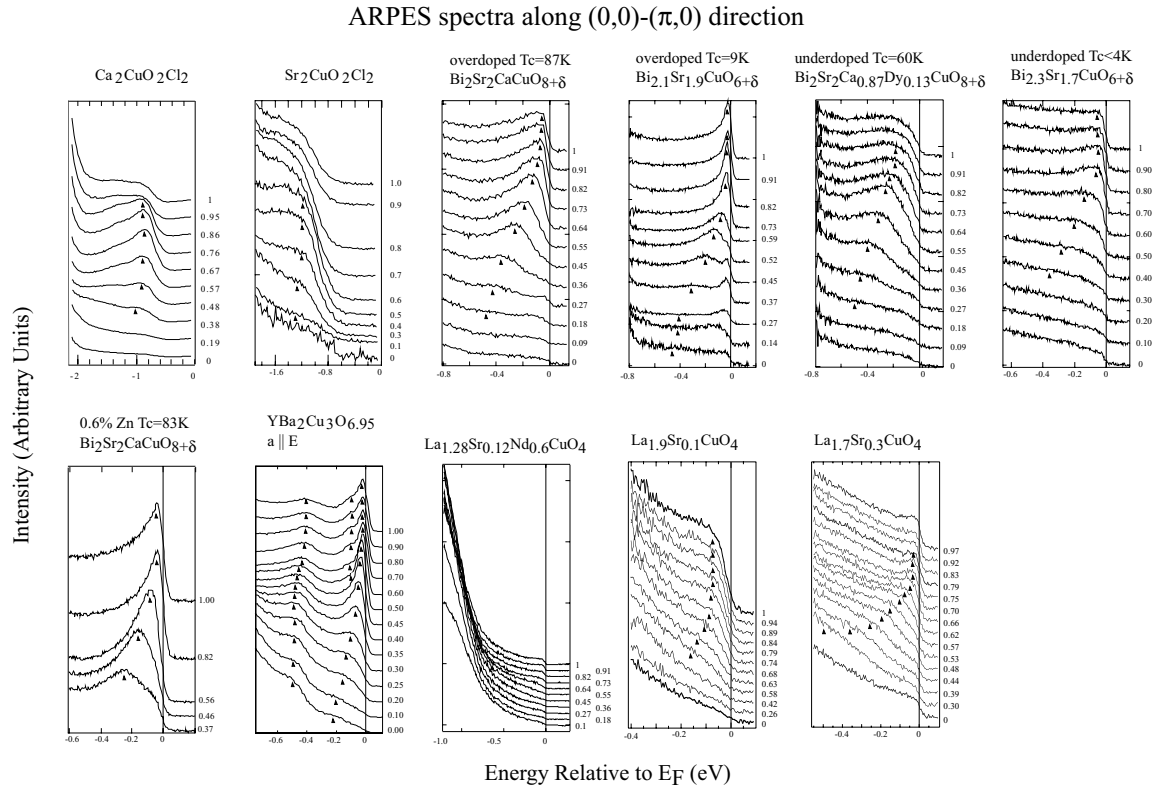


Figure A.25: A comparison of ARPES spectra along  $(0,0) - (\pi,0)$  directions for various cuprates.

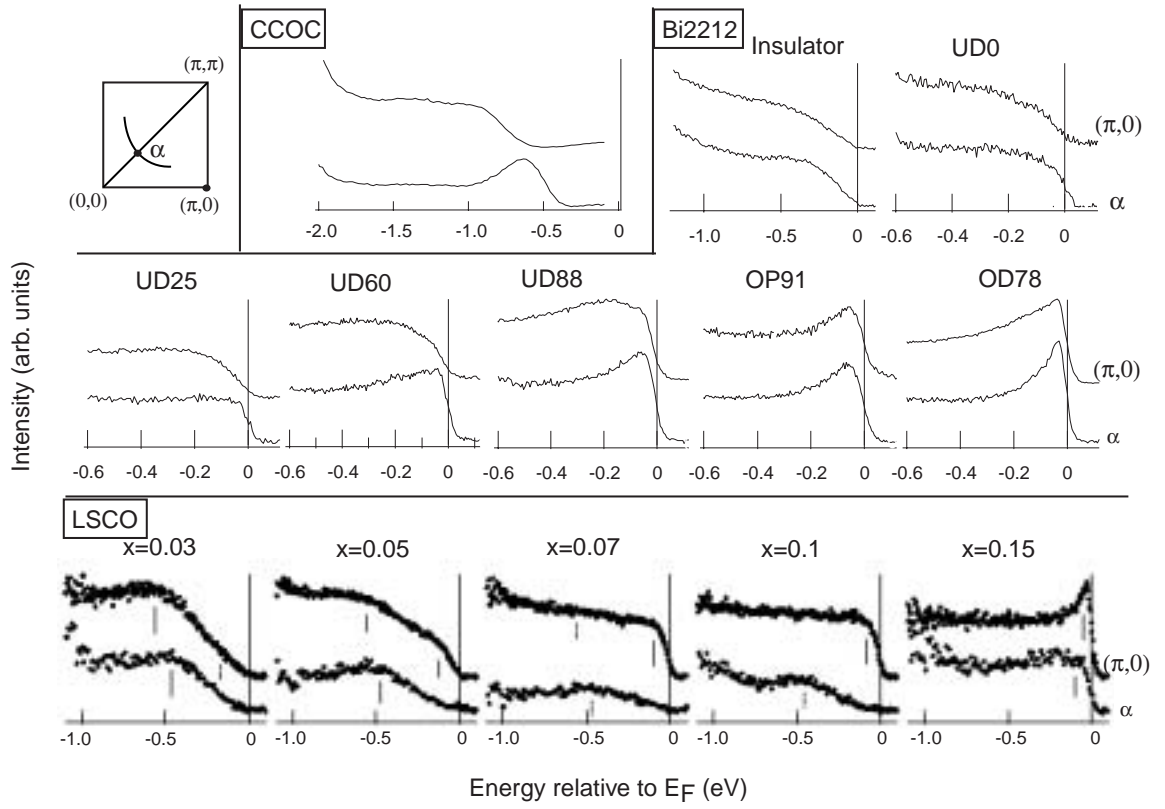


Figure A.26: ARPES spectral lineshape comparison at nodal  $(\pi,\pi)$  and antinodal  $(\pi,0)$  regions for CCOC, Bi2212, and LSCO systems. CCOC data is reproduced by the courtesy of F. Ronning, LSCO data is reproduced by the courtesy of I. Akihiro.

# Appendix B

## Donglai Feng's Publication

As Primary Author

1. **D. L. Feng**, C. Kim, H. Eisaki, D.H. Lu, K. M. Shen, F. Ronning, N. P. Armitage, A. Damascelli, N. Kaneko, M. Greven, J.-i. Shimoyama, K. Kishio, R. Yoshizaki, G. D. Gu and Z.-X. Shen, “*Nature of the Electronic Excitations near the Brillouin Zone Boundary of  $\text{Bi}_2\text{Sr}_2\text{CaCu}_2\text{O}_{8+\delta}$* ”, Physical Review Letters (in review).
2. **D. L. Feng** , A. Damascelli, K.M. Shen, H. Eisaki, C. Kim, D.H. Lu, F. Ronning, N.P. Armitage, Z.-X. Shen, K. Shimizu, J.-i. Shimoyama, K. Kishio, N. Motoyama, N. Kaneko, M. Greven and G.D. Gu “*ARPES study of the trilayer cuprate superconductor  $\text{Bi}_2\text{Sr}_2\text{Ca}_2\text{Cu}_3\text{O}_{10+\delta}$* ”, Physical Review Letters (in review).
3. **D. L. Feng**, N. P. Armitage, D.H. Lu, C. Kim, A. Damascelli, , F. Ronning, K. M. Shen, J.-i. Shimoyama, K. Kishio, and Z.-X. Shen, “*Bilayer splitting in the electronic structure of heavily overdoped  $\text{Bi}_2\text{Sr}_2\text{CaCu}_2\text{O}_{8+\delta}$* ”, Physical Review Letters **86**, 5550 (2001).
4. **D. L. Feng**, D. H. Lu, K. M. Shen, C. Kim, H. Eisaki, A. Damascelli, R. Yoshizaki, J.-i. Shimoyama, K. Kishio, G. D. Gu, S. Oh, A. Andrus, J. O'Donnell,

- J. N. Eckstein, Z.-X. Shen, “Signature of Superfluid Density in the Single-Particle Excitation Spectrum of  $\text{Bi}_2\text{Sr}_2\text{CaCu}_2\text{O}_{8+\delta}$ ”, Science, **289**, p. 277-281, (Jul. 2000).
5. **D. L. Feng**, D. H. Lu, K. M. Shen, S. Oh, A. Andrus, J. O'Donnell, J. N. Eckstein, Jun-ichi Shimoyama, Kohji Kishio, and Z. X. Shen, “On the Similarity of the Spectral Weight Pattern of  $\text{Bi}_2\text{Sr}_2\text{CaCu}_2\text{O}_{8+\delta}$  and  $\text{La}_{1.48}\text{Nd}_{0.4}\text{Sr}_{0.12}\text{CuO}_4$ ”, Physica C, **341** no. 4 p. 2097-2098 (Nov. 2000).
  6. **D. L. Feng**, C.-X. Yu, J. L. Xie, W. X. Ding, “On-off intermittencies in gas discharge plasma”, Physical Review E, **58**, no.3, p.3678-85, (Sept. 1998).
  7. **D. L. Feng**, “On-off intermittencies in gas-discharge plasma”, M.S. thesis, University of Science and Technology of China, Hefei, P. R. China (1996).
  8. **D. L. Feng**, J. Zheng, W. Huang, C.-X. Yu, W. X. Ding, “Type-I-like intermittent chaos in multicomponent plasmas with negative ions”, Physical Review E, **54**, no.3, p. 2839-43, (Sept. 1996).

### As Secondary Author

9. C. Kim A. Mehta, **D. L. Feng**, K.M. Shen, N.P. Armitage, K. Char, Y.Y. Xie and J. Wu, “X-ray diffraction measurements of the c-axis Debye-Waller factors of  $\text{YBa}_2\text{Cu}_3\text{O}_7$  and  $\text{HgBa}_2\text{CaCu}_2\text{O}_6$ ”, Physical Review B (in review).
10. K.M. Shen, A. Damascelli, D.H. Lu, N.P. Armitage, F. Ronning, **D. L. Feng**, C. Kim, Z.-X. Shen, D.J. Singh, I.I. Mazin, S. Nakatsuji, Z.Q. Mao, Y. Maeno, T. Kimura, Y. Tokura. “Surface Electronic Structure of  $\text{Sr}_2\text{RuO}_4$ ”. Phys. Rev. B (Rapid Comm.), (in press) (2001).
11. N.P. Armitage, D.H. Lu, C. Kim, A. Damascelli, K.M. Shen, F. Ronning, **D. L. Feng**, Z.X. Shen, Y. Onose, Y. Taguchi, Y. Tokura, “Particle-hole asymmetry in the electronic structure of the cuprate superconductors”, Physical Review Letters (accepted) .

12. P.J. White, Z.-X. Shen, **D. L. Feng**, C. Kim, M.-Z.Hasan, J.M. Harris, A.G. Loeser, H.Ikeda, R. Yoshizaki, G.D.Gu, N.Koshizuka, “*Photoemission Studies on  $\text{Bi}_2\text{Sr}_2\text{Ca}(\text{Cu}_{1-x}\text{Zn}_x)_2\text{O}_{8+\delta}$ : Electronic Structure Evolution and Temperature Dependence*”, Physical Review B (in review).
13. P. V. Bogdanov, A. Lanzara, X. J. Zhou, S. A. Kellar, **D. L. Feng**, E. D. Lu, J. -I. Shimoyama, K. Kishio, Z. Hussain, Z. X. Shen, “*ARPES study of Pb doped  $\text{Bi}_2\text{Sr}_2\text{CaCu}_2\text{O}_{8+\delta}$  - an unambiguous case for an electron-like Fermi surface*”, Physical Review Letters (in review).
14. A. Lanzara, P. V. Bogdanov, X. J. Zhou, S. A. Kellar, **D. L. Feng**, E. D. Lu, T. Yoshida, H. Eisak, A. Fujimori, K. Kishio, J. -I. Shimoyama, T. Noda, S.Uchida, Z. Hussain and Z.-X. Shen, “*Evidence for ubiquitous strong electron-phonon coupling in high-temperature superconductors*”, Nature **412**, p. 510-514 (2001).
15. C. Kim,, F. Ronning, A. Damascelli, **D. L. Feng**, Z.-X. Shen, B.O. Wells, Y.J. Kim, R.J. Birgeneau, M.A. Kastner, L.L. Miller, H. Eisaki, and S. Uchida, “*Anomalous Temperature Dependence in Photoemission Spectral Function of Cuprates*”, Physical Review B (in press).
16. D. H. Lu, **D. L. Feng**, N. P. Armitage, K. M. Shen, A. Damascelli, C. Kim, F. Ronning, D. A. Bonn, R. Liang, W. N. Hardy, A. I. Rykov, S. Tajima, and Z.-X. Shen, “*Superconducting Gap and Strong In-Plane Anisotropy in Untwinned  $\text{YBa}_2\text{Cu}_3\text{O}_{7-y}$  Single Crystals*”, Physical Review Letter, **86**, 4370 (2001).
17. N.P. Armitage, D.H. Lu, **D. L. Feng**, C. Kim, A. Damascelli, K.M. Shen, F. Ronning, Y. Onose, Y. Taguchi, Y. Tokura, Z.X. Shen, “*Anisotropy of the Superconducting Gap in  $\text{Nd}_{1.85}\text{Ce}_{0.15}\text{CuO}_4$ : Results from Photoemission*”, Physical Review Letter, **86** no. 6 p. 1126-1129 (Feb. 2001).
18. A. Damascelli, K.M. Shen, D.H. Lu, N.P. Armitage, F. Ronning, **D. L. Feng**, C. Kim, Z.-X. Shen, T. Kimura, Y. Tokura, Z.Q. Mao, Y. Maeno, “*Fermi Surface*

- of  $\text{Sr}_2\text{RuO}_4$  from Angle Resolved Photoemission.”, J. Electron Spectr. Relat. Phenom., **114-116**, p. 641-646 (2001).
19. A. Damascelli, D.H. Lu, K.M. Shen, N.P. Armitage, F. Ronning, **D. L. Feng**, C. Kim, Z.-X. Shen, T. Kimura, Y. Tokura, Z.Q. Mao, Y. Maeno, “*Fermi surface, surface states, and surface reconstruction in  $\text{Sr}_2\text{RuO}_4$* ”, Physical Review Letter, **85** no. 24 p. 5194-5197 (Dec. 2000).
  20. Z. X. Shen, **D. L. Feng**, “*Superconducting Gap and Pseudogap by Angle Resolved Photoemission measurement*”, Chapter 8 in the book “Fundamental Research in High Tc Superconductivity” in “Frontiers in Science Series” edited by W. Z. Zhou and W. Y. Liang, Shanghai Sci. Tech. Publishing Co. , Shanghai China (1999).
  21. F. Ronning, C. Kim, **D. L. Feng**, D. S. Marshall, A. G. Loeser, L. L. Miller, J. N. Eckstein, I. Bozovic, and Z.-X. Shen, “*Photoemission Evidence for a Remnant Fermi Surface and a d- Wave-Like Dispersion in Insulating  $\text{Ca}_2\text{CuO}_2\text{Cl}_2$* ”, Science, **282**, p.2067-2072, (Dec. 1998).
  22. Z.-X. Shen, P. J. White; **D. L. Feng**, C. Kim, G. D. Gu, H. Ikeda, R. Yoshizaki, N. Koshizuka “*Temperature-induced momentum-dependent spectral weight transfer in  $\text{Bi}_2\text{Sr}_2\text{CaCu}_2\text{O}_{8+\delta}$* ”, Science, **280**, p. 259-62, (April 1998).
  23. W. Huang, W.X. Ding, **D. L. Feng**, C. X. Yu, “*Estimation of a Lyapunov-exponent spectrum of plasma chaos*”, Physical Review E, **50**, no.2, p.1062-9, (Aug. 1994).